Microstructure and crystal order during freezing of supercooled water drops

Armin Kalita,[1] Maximillian Mrozek-McCourt,[1,5] Thomas F. Kaldawi,[1,6] Philip R.Willmott,[2,3]
N. Duane Loh,[4,7,8] Sebastian Marte,[1] Raymond G. Sierra,[4,9] Hartawan Laksmono,[4,10] Jason E. Koglin,[2,11]
Matt J. Hayes,[2] Robert H. Paul,[2] Serge A. H. Guillet,[2] Andrew L. Aquila,[2] Mengning Liang,[2]
Sébastien Boutet[2] and Claudiu A. Stan[1,4,*]

[1]*Department of Physics, Rutgers University-Newark, Newark, NJ, USA*
[2]*Linac Coherent Light Source, SLAC National Accelerator Laboratory, Menlo Park, CA 94025, USA*
[3]*Paul Scherrer Institute, Villigen, Switzerland*
[4]*Stanford PULSE Institute, SLAC National Accelerator Laboratory, Menlo Park, CA 94025, USA*

[5]*Present address: Department of Physics, Lehigh University, Bethlehem, PA, USA*
[6]*Present address: Department of Physics, University of Rochester, Rochester, NY, USA*
[7]*Present address: Department of Biological Sciences, National University of Singapore, Singapore, Singapore*
[8]*Present address: Department of Physics, National University of Singapore, Singapore, Singapore*
[9]*Present address: Linac Coherent Light Source, SLAC National Accelerator Laboratory, Menlo Park, CA, USA*
[10]*Present address: KLA-Tencor, Three Technology Drive, Milpitas, CA, USA*
[11]*Present address: Los Alamos National Laboratory, Los Alamos, NM, USA*

[*]*email: claudiu.stan@rutgers.edu*

Supercooled water droplets are widely used to study supercooled water[1,2], ice nucleation[3-5], and droplet freezing[6-11]. Their freezing in the atmosphere impacts the dynamics and the climate feedback of clouds[12,13], and can accelerate cloud freezing via secondary ice production[14-17]. Droplet freezing occurs at multiple time and length scales[14,18], and is sufficiently stochastic to make it unlikely that two frozen drops are identical. Here we use optical microscopy and X-ray laser diffraction to investigate the freezing of tens of thousands of water microdrops in vacuum after homogeneous ice nucleation around 234–235 K. Based on drop images, we developed a seven-stage model of freezing and used it to time the diffraction data. Diffraction from ice crystals showed that long-range crystalline order formed in less than 1 ms after freezing, while diffraction from the remaining liquid became similar to the one from quasiliquid layers on premelted ice[19,20]. The ice had a strained hexagonal crystal structure just after freezing, which is an early metastable state that likely precedes the formation of ice with stacking defects[8,9,18]. The techniques reported here could help determine the dynamics of freezing in other conditions, such as drop freezing in clouds, or help understand rapid solidification in other materials.

We investigated the freezing of individual 40-μm diameter supercooled water drops using the setup illustrated in Fig. 1. The droplets were injected into a vacuum chamber, where they cooled rapidly through evaporation, nucleated ice homogeneously, and froze. Femtosecond X-ray pulses and nanosecond light pulses arrived simultaneously at the freezing droplets, producing X-ray diffraction patterns and images of single droplets at multiple times of flight from 6.4 to 7.8 ms after injection. The droplets were probed only once.

The freezing of the droplets started with ice nucleation around 234–235 K, followed by dendritic crystal growth leading to partial solidification and heating to the melting temperature, then by inward freezing of the remaining liquid, during which the drops grew spicules and sometimes shattered (Extended Data Fig. 1(a)). These stages of freezing were also observed in studies with varied droplet environments, sizes and cooling rates[14], see for example the supplementary videos in refs.[4,6]. The commonality of freezing stages is largely due to the dynamics of dendritic freezing in supercooled water. Dendritic freezing is an extreme thermal process that generates large heat fluxes and thermal gradients of the order of 10 K/μm at the freezing front[10]. It depends primarily on temperature and is relatively insensitive to the drop's environment[10] for drops larger than 0.1–1 μm, for which the dynamics of dendritic freezing remains approximately the same over a wide range of cooling rates. Dendritic freezing also produces a common initial state for the later stages of freezing: an ice-liquid mixture at the melting temperature. This mixture fully solidifies by inward freezing if the drop remains in the environment that supercooled it. The duration of inward freezing depends on the environment. For the present experiment, we estimated that it is ~1 ms using a finite-element solidification model (Methods, Supplementary Information (SI)).

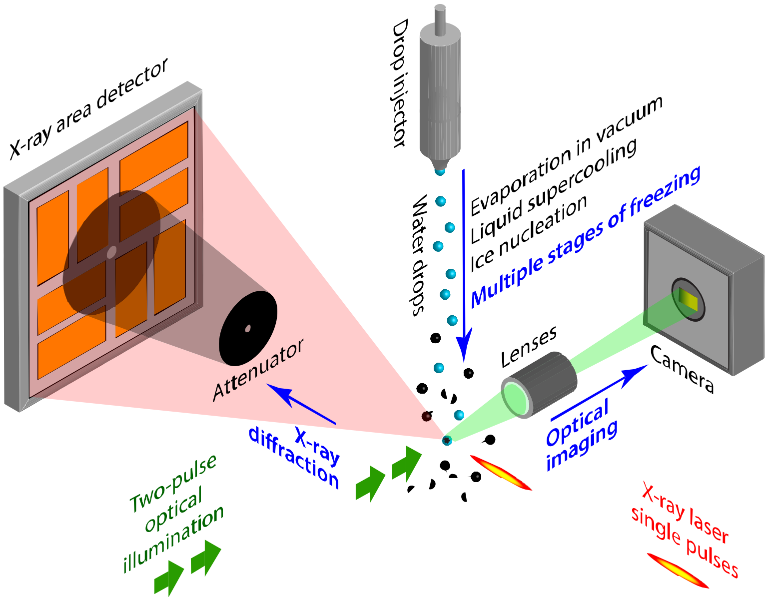

Figure 1. Capturing the earliest stages of freezing in supercooled water drops. 40-µm diameter water drops were injected in a vacuum chamber, where they cooled rapidly and froze after homogeneous ice nucleation. The freezing drops were probed simultaneously using X-ray laser diffraction and two-pulse optical imaging.

Since both the duration of freezing and the spread of nucleation times were approximately 1 ms, the drops probed at one time of flight had a broad distribution of freezing stages, and we investigated of the order of 1000 drops at each time of flight to determine the stage probabilities and their temporal evolution. To capture the statistics of droplet splitting, we recorded additional data using 12 light exposures per image to record multiple images of each droplet (Extended Data Fig 1(b)). Compared to larger droplets[6,7] we observed smaller deformations, a larger number of spicules with smaller relative sizes, and higher fragment velocities (Extended Data Fig. 1(c-f)).

The stochastic nature of nucleation limits the time resolution to the spread of nucleation times, both in experiments using one-shot measurements of single drops[11,21] and in experiments probing multiple drops simultaneously, such as emulsion systems[8,9]. We addressed this problem by developing a detailed model for the freezing of a supercooled droplet. The model, illustrated in Fig. 2(a), has seven optically identifiable stages of freezing: (1) Liquid supercooled water in which ice will nucleate homogenously.

(2) Dendritic growth of ice, which freezes approximately half of the liquid[22] and deforms the droplet slightly. (3) An initial stage of inward freezing, in which a smooth solid shell of ice forms around a core filled with a mixture of ice dendrites and liquid. (4) The appearance and growth of small spicules on the surface of the drop. The spicules are formed by liquid driven from the core through cracks in the solid shell, due to the pressure build-up caused by the expansion of water upon freezing. (5) Drops with large spicules. (6) Drops that cracked due to the pressure build-up but did not split. (7) Drops split into fragments. During freezing, the drops first evolve from stage 1 to stage 5, then freezing ends with one of the stages 5, 6, or 7.

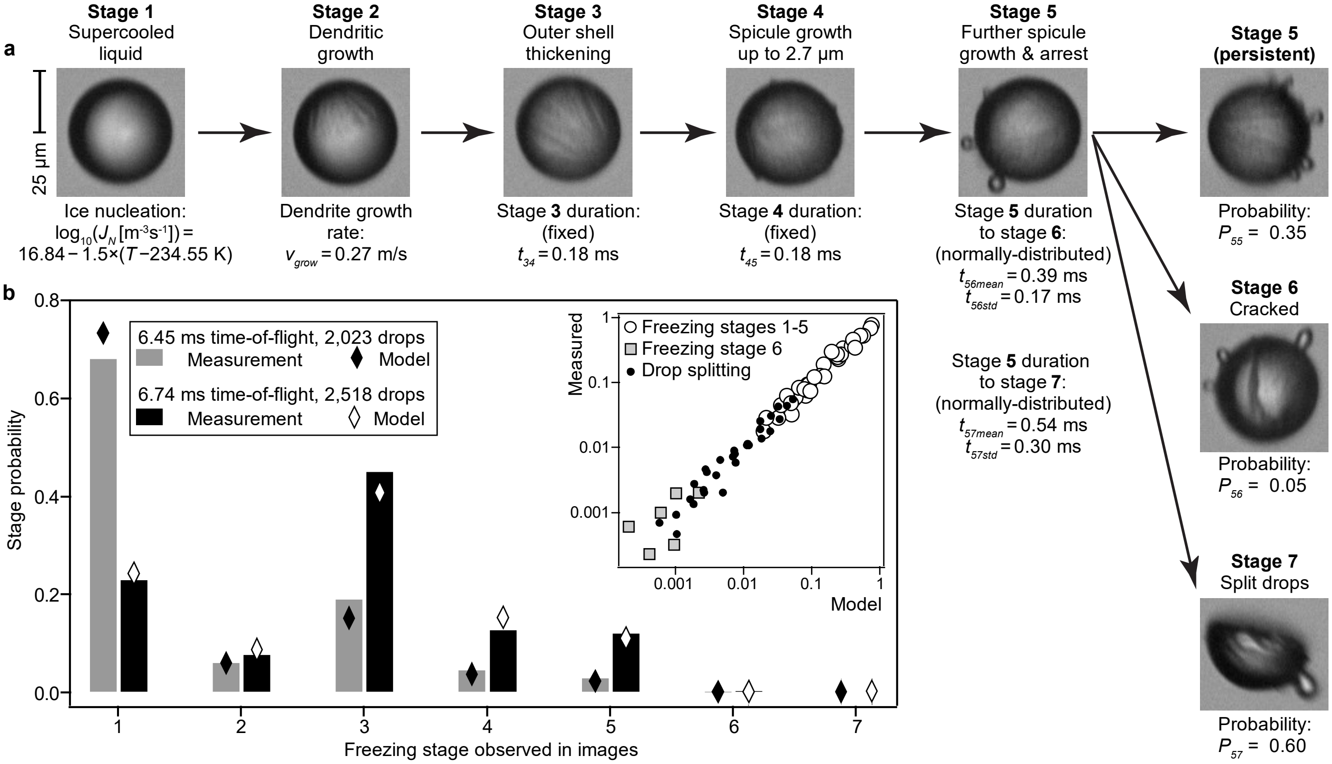

Figure 2. A detailed model of freezing in 40-µm supercooled water drops in vacuum, after homogeneous nucleation. (a) The freezing process was modelled using seven stages of freezing that are identifiable in optical images. The dynamics of each stage is characterized by the physical parameters listed in the figure, which were obtained by fitting the model against measurements from thousands of drops. (b) Comparison of experimental and modelled probabilities of observing drops in specific freezing stages. The graph shows the freezing stage probabilities for two of the data sets, and the inset displays the freezing stage or the splitting probability for all the data sets used.

The freezing model is stochastic and was used to simulate freezing in large ensembles of drops. The ensemble simulations provided the probabilities of observing each freezing stage at a given time of flight, the probability of drops splitting over a range of times of flight, and ensemble-averaged properties such as the time elapsed from nucleation.

The freezing model parameters were determined using a complex fitting procedure (Methods, Supplementary Information). They are shown in Extended Data Table 1 and represent the best match between the model and our experiment, which is illustrated in Fig. 2(b) by comparing measured and modelled probabilities. Since the freezing parameters are implicitly dependent on the model, they are not a unique solution to the problem of quantifying all freezing stages, but the ice nucleation rate and the dendrite growth velocity are consistent with previous dedicated measurements (Methods, Extended Data Fig. 5), while the other parameters quantify additional freezing processes.

The parameters of the freezing stages after the completion of dendritic growth are specific to our drop size, temperature, and cooling rate. We modelled the durations of pressure build-up before the generation of spicules and the initial growth of spicules with fixed times, because the fit of the model was not improved when using normally-distributed values. The fixed duration of stages 3 and 4 is consistent with both being approximately deterministic. In contrast, the fit of the model was better when using normally-distributed values for the times spent before the fracture and splitting of drops, indicating that fracture and splitting are stochastic events.

In clouds, the splitting of frozen drops is a secondary ice production process, and its probability depends sensitively on the drop's properties and environment[7,23]. The probability of splitting in our model, $P_{57} = 0.6$, is larger than the ones observed in experiments at atmospheric conditions[7], where the duration of solidification is substantially longer (Methods, Extended Data Fig. 2(i-j)). While P_{57} cannot be applied to cloud modelling, it is consistent with an observed increase of the splitting probability with the cooling rate[23], which could make it useful for parametrizing the splitting probability of cloud droplets. P_{57} is inconsistent with a model based on studying millimetre-sized drops freezing near 266 K, which predicted that drops with diameters below 50 μm will not split[6]. This discrepancy can be explained by two factors that were different in our experiment: (i) the initial dendrites filled approximately half of the droplet volume and reinforced it against splitting, and (ii) according to our solidification model the surface of drops cooled 14 degrees below the melting temperature at complete solidification (see Extended Data Fig. 2(f)), which would increase the fracture strength of ice. The increased fracture strength allows the buildup of more elastic energy before fragmentation, and may restrict the pressure-releasing process of spicule growth.

The freezing model also enabled the calculation of the mean and standard deviation of the times elapsed from ice nucleation for all stages. For the earliest freezing stages, these standard deviations were approximately ±0.02 ms, shorter than the ~0.3 ms standard deviation of the nucleation times. Therefore, data sorted by the freezing stage had up to one order of magnitude better temporal resolution than unsorted data.

We analysed the evolution of X-ray scattering during freezing by grouping data from single drops by their freezing stage, and by separating the crystal diffraction from liquid scattering (Extended Data Fig. 6, Methods). Figure 3 and Extended Data Fig. 7 show representative scattering profiles from drops in different freezing stages.

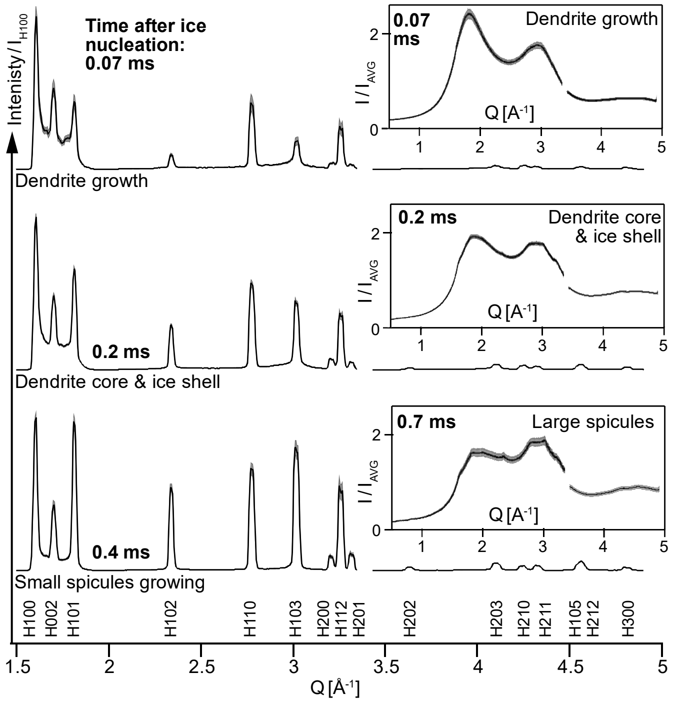

Figure 3. The evolution of X-ray scattering from the crystal and liquid phases during freezing. The crystal diffraction peaks (left), labelled according to the Miller indices of hexagonal ice, are characteristic of hexagonal ice. The intensity of high-index reflections increases with the time elapsed after ice nucleation, indicating the formation of long-range crystalline order. The diffuse scattering patterns from the liquid (right) show a relative increase in the second diffuse peak. During freezing, the liquid scattering patterns become similar to the ones observed on premelted ice. The crystal data is normalized to the height of the first peak, and the liquid data is normalized to the average intensity. The gap at 3.4 Å^{-1} is a region with unreliable data near the edge of the attenuator shadow, which hides a hexagonal (004) peak. The standard deviations, evaluated via bootstrapping over bands with ΔQ = 0.0025 Å^{-1}, are shown as upper and lower confidence bands at one standard deviation (Methods).

The dominant changes in the X-ray scattering patterns during freezing were the increase of most crystal diffraction peaks relative to the first one, and the relative increase of the second liquid scattering peak. Most of the evolution of crystal diffraction patterns occurred before the drops reached stage 5 of freezing at approximately 0.5 ms after nucleation, indicating that long-range crystalline order formed on a timescale of less than a millisecond.

The scattering patterns from supercooled water drops had the same shape as observed previously, with the second liquid peak being higher than at the melting temperature[2]. During freezing, which heated the dendrite-liquid mixture close to the melting temperature, the second peak continued to increase, instead of becoming lower as expected for a heated bulk liquid. Since similar X-ray scattering patterns were observed from the quasiliquid layer (QLL) on the surface of premelted ice[19], it is likely that the interstitial liquid between the dendrites has a structure similar to the QLL on premelted ice, and is related to the QLL between ice grains[20,24].

The crystal diffraction patterns displayed all the main peaks characteristic of hexagonal ice. The relative heights of the peaks from drops in the last stages of freezing (Fig. 3, Extended Data Fig. 7) were different from the ones observed in drops with annealed hexagonal ice[9]. Since the drops we investigated contain small crystals, peak heights different from bulk annealed ice are to be expected (Extended Data Fig. 7(a)). The raised background between the first three peaks is caused by diffraction spots from highly strained crystals (Extended Data Fig. 9). These spots are different from the features generated by stacking defects in X-ray laser diffraction[25]. The radial diffraction patterns did not show a significant signal near the cubic ice (400) peak at 3.93 $Å^{-1}$, which is unique to cubic ice and well separated from the nearest peaks of hexagonal ice. We therefore conclude that from 0.03 to 1 ms after freezing, the ice had a predominantly hexagonal structure.

This freshly formed ice is different from the stable hexagonal ice. Figure 4(a) shows an image of the X-ray detector data accumulated from stage 5 drops. As the diffraction angle increases, the diffraction peaks have increasingly elongated shapes in the radial direction, indicating a substantial inhomogeneous strain. Some of the peaks are also split, suggesting the existence of two preferred strain levels. A Williamson-Hall plot[26] is shown in Fig. 4(b) for drops in stages 4 to 7 probed at low intensity to prevent saturation. Additional evaluations of the inhomogeneous strain for the crystal data shown in Fig. 3, which was affected by detector saturation (Methods), did not reveal a significant evolution of the strain with the freezing stage; the strain remained large up to 1 ms after freezing and was not relaxed by the splitting of drops.

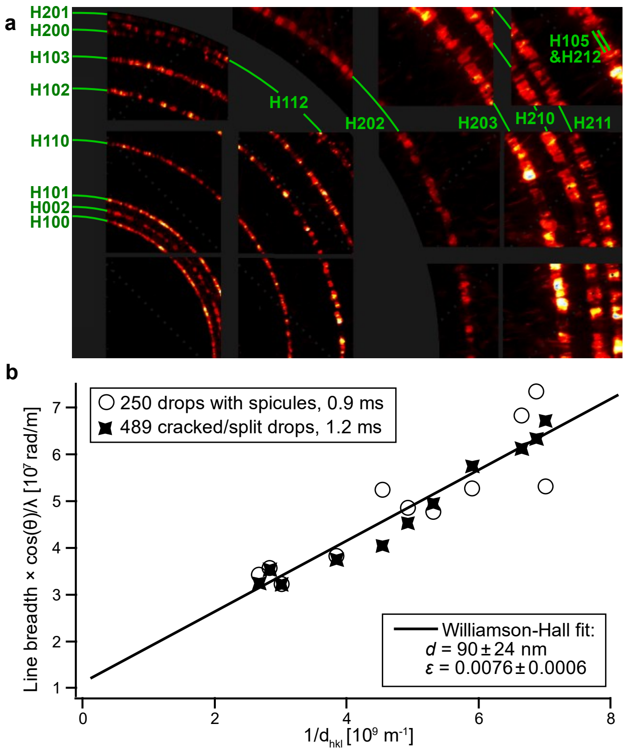

Figure 4. Inhomogeneous strain in rapidly solidified ice. (a) Composite X-ray detector image showing the crystal diffraction accumulated from 784 drops in the stage 5 of freezing, 0.7 ms on average after nucleation. The Bragg peaks are elongated in the radial direction and the elongation increases with the diffraction angle. (b) The dependence of the broadening of crystal peaks on the reciprocal of the lattice planes spacing. The linear fit is a Williamson-Hall analysis providing the ice crystal grain size *d* and the inhomogeneous strain *ε*, with uncertainties calculated from the standard deviation of the fit coefficients.

The evolution of the diffraction patterns during freezing indicates how the long-range crystalline order develops. At the shortest time delay investigated (27 μs average; see Extended Data Fig. 7(a)), the diffraction was dominated by the (100), (110) and (002) peaks, which are the markers of short-range order in the (001) basal plane sheets and in the stacking distance of these sheets; the (101) peak, which is a marker of proper registration between sheets, had a low intensity. During freezing, both the peaks reflecting long-range order in the hexagonal sheets ((hk0), h > 1 or k > 1) and the peaks reflecting the registration of sheets ((h0l), (hkl)) increased, with similar timescales. These observations indicate that the formation of crystalline order starts with short-range order in the basal plane sheets and in their stacking separation, and then continues with a concurrent enhancement of the order within the sheets and in the registration of the sheets.

We investigated higher nucleation temperatures using drops that nucleated ice heterogeneously, doped with either Arizona Test Dust (ATD, nucleation at 240–249 K) or silver iodide (AgI, nucleation at 260–265 K). The same freezing stages were observed, and their properties depended on temperature (see SI and Extended Data Fig. 8(c)). The X-ray diffraction evolved with the freezing stage, and Extended Data Figs. 8 and 9 compare the diffraction from pure and doped drops, for stages 2 and 5. In all cases, the diffraction profiles were consistent with the strained hexagonal ice structure, and the similar widths of the peaks indicated a similar degree of strain.

The diffraction patterns after heterogeneous nucleation had higher peak heights during dendritic freezing, which can be explained by longer time delays after nucleation but also suggests that the crystalline order develops faster and better in less supercooled drops. In particular, the drops with AgI displayed the very weak hexagonal (104) peak, and the raised background between the first three peaks was negligible. The diffraction images for drops with AgI (Extended Data Fig. 9) displayed a combination of diffuse spots with bright spots with a smaller radial elongation, indicating that some crystals had a narrower strain distribution than the crystals grown in colder drops.

The strained hexagonal ice is the structure with long-range order that forms first in water microdrops supercooled by ~10 K to ~40 K. The existence of strained hexagonal ice at multiple nucleation temperatures indicates that this ice is likely to be a metastable state that precedes the formation of ice with stacking defects and high cubicity.

A transition from strained hexagonal ice to ice with stacking defects seems feasible energetically (Methods). Such an evolution of ice was discussed theoretically[27], but was not observed in simulations[28,29]. Experiments that observed ice with stacking defects in microdrops used concentrated emulsions[8,9,18,30]. Based on the applied cooling rates[30], the emulsions were probed minutes after freezing and spent seconds within a few degrees of the freezing temperatures. These time delays are much longer than in our experiment and may enable a transformation from strained hexagonal ice to ice with stacking defects. Here we did not observe an evolution towards the diffraction patterns of ice with stacking defects. Understanding how the strained hexagonal ice is related to ice with stacking defects will require further experiments that control the temperature of ice during and after freezing.

The freezing of supercooled water droplets is a complex sequence of processes. At the droplet scale, the complexity of freezing can be disentangled using large numbers of observations in combination with detailed physical modelling. This detailed quantification of freezing stages enables improved hydrodynamic models of drop freezing[6], which may become accurate enough to predict splitting probabilities and other properties relevant to secondary ice production in the atmosphere. At the molecular scale, the ice formed from supercooled water microdrops between 234–265 K evolves through possibly more than one class of metastable states before becoming a perfect crystal. A similarly rich freezing dynamics may occur in other substances, offering opportunities to understand nonequilibrium solidification and to discover metastable materials.

References

1 Angell, C. A., Oguni, M. & Sichina, W. J. Heat Capacity of Water at Extremes of Supercooling and Superheating. *J. Phys. Chem.* **86**, 998-1002 (1982).

2 Sellberg, J. A. *et al.* Ultrafast X-ray probing of water structure below the homogeneous ice nucleation temperature. *Nature* **510**, 381-384 (2014).

3 Stöckel, P., Weidinger, I. M., Baumgartel, H. & Leisner, T. Rates of Homogeneous Ice Nucleation in Levitated H_2O and D_2O Droplets. *J. Phys. Chem. A* **109**, 2540-2546 (2005).

4 Stan, C. A. *et al.* A microfluidic apparatus for the study of ice nucleation in supercooled water drops. *Lab Chip* **9**, 2293-2305 (2009).

5 Hagen, D. E., Anderson, R. J. & Kassner, J. L. Homogeneous Condensation–Freezing Nucleation Rate Measurements for Small Water Droplets in an Expansion Cloud Chamber. *J. Atmos. Sci.* **38**, 1236-1243 (1981).

6 Wildeman, S., Sterl, S., Sun, C. & Lohse, D. Fast Dynamics of Water Droplets Freezing from the Outside In. *Phys. Rev. Lett.* **118**, 084101 (2017).

7 Lauber, A., Kiselev, A., Pander, T., Handmann, P. & Leisner, T. Secondary Ice Formation during Freezing of Levitated Droplets. *J. Atmos. Sci.* **75**, 2815-2826 (2018).

8 Murray, B. J., Knopf, D. A. & Bertram, A. K. The formation of cubic ice under conditions relevant to Earth's atmosphere. *Nature* **434**, 202-205 (2005).

9 Malkin, T. L., Murray, B. J., Brukhno, A. V., Anwar, J. & Salzmann, C. G. Structure of ice crystallized from supercooled water. *Proc. Natl. Acad. Sci. USA* **109**, 1041-1045 (2012).

10 Buttersack, T. & Bauerecker, S. Critical Radius of Supercooled Water Droplets: On the Transition toward Dendritic Freezing. *J. Phys. Chem. B* **120**, 504-512 (2016).

11 Esmaeildoost, N. *et al.* Heterogeneous Ice Growth in Micron-Sized Water Droplets Due to Spontaneous Freezing. *Crystals* **12**, 65 (2022).

12 Pruppacher, H. R. & Klett, J. D. *Microphysics of Clouds and Precipitation*. (Springer Dordrecht, 2010).

13 Murray, B. J., Carslaw, K. S. & Field, P. R. Opinion: Cloud-phase climate feedback and the importance of ice-nucleating particles. *Atmos. Chem. Phys.* **21**, 665-679 (2021).

14 Korolev, A. & Leisner, T. Review of experimental studies of secondary ice production. *Atmos. Chem. Phys.* **20**, 11767-11797 (2020).

15 Field, P. *et al.* Secondary ice production: Current state of the science and recommendations for the future. *Meteor. Mon.* **58**, 7.1-7.20 (2017).

16 Kleinheins, J., Kiselev, A., Keinert, A., Kind, M. & Leisner, T. Thermal Imaging of Freezing Drizzle Droplets: Pressure Release Events as a Source of Secondary Ice Particles. *J. Atmos. Sci.* **78**, 1703-1713 (2021).

17 Korolev, A. *et al.* Observation of secondary ice production in clouds at low temperatures. *Atmos. Chem. Phys.* **22**, 13103-13113 (2022).

18 Malkin, T. L. *et al.* Stacking disorder in ice I. *Phys. Chem. Chem. Phys.* **17**, 60-76 (2015).

19 Maruyama, M. *et al.* X-Ray Analysis of the Structure of Premelted Layers at Ice Interfaces. *Jpn. J. Appl. Phys.* **39**, 6696-6699 (2000).

20 Dash, J. G., Rempel, A. W. & Wettlaufer, J. S. The physics of premelted ice and its geophysical consequences. *Rev. Mod. Phys.* **78**, 695-741 (2006).

21 Laksmono, H. *et al.* Anomalous Behavior of the Homogeneous Ice Nucleation Rate in "No-Man's Land". *J. Phys. Chem. Lett.* **6**, 2826-2832 (2015).

22 Buttersack, T., Weiss, V. C. & Bauerecker, S. Hypercooling Temperature of Water is about 100 K Higher than Calculated before. *J. Phys. Chem. Lett.* **9**, 471-475 (2018).

23 Keinert, A., Spannagel, D., Leisner, T. & Kiselev, A. Secondary Ice Production upon Freezing of Freely Falling Drizzle Droplets. *J. Atmos. Sci.* **77**, 2959-2967 (2020).

24 Thomson, E. S., Hansen-Goos, H., Wettlaufer, J. S. & Wilen, L. A. Grain boundary melting in ice. *J. Chem. Phys.* **138** (2013).

25 Niozu, A. *et al.* Crystallization kinetics of atomic crystals revealed by a single-shot and single-particle X-ray diffraction experiment. *Proc. Natl. Acad. Sci. USA* **118** (2021).

26 Williamson, G. K. & Hall, W. H. X-ray line broadening from filed aluminium and wolfram. *Acta Metall.* **1**, 22-31 (1953).

27 Hondoh, T. Dislocation mechanism for transformation between cubic ice I_c and hexagonal ice I_h. *Philos. Mag.* **95**, 3590-3620 (2015).

28 Haji-Akbari, A. & Debenedetti, P. G. Direct calculation of ice homogeneous nucleation rate for a molecular model of water. *Proc. Natl. Acad. Sci. USA* **112**, 10582-10588 (2015).

29 Lupi, L. *et al.* Role of stacking disorder in ice nucleation. *Nature* **551**, 218-222 (2017).

30 Murray, B. J. & Bertram, A. K. Formation and stability of cubic ice in water droplets. *Phys. Chem. Chem. Phys.* **8**, 186-192 (2006).

Methods

The experiments were conducted at the Coherent X-ray Imaging (CXI) instrument[31] of the Linac Coherent Light Source (LCLS) X-ray free-electron laser (XFEL) facility[32]. The experimental setup was installed in the SC1 sample environment setup, which provided a vacuum environment with a pressure below 0.1 Pa. SC1 included X-ray optics that focused the XFEL pulses to a nominal diameter of 1 μm and a Cornell-SLAC Pixel Array Detector (CSPAD) X-ray camera[33] to record scattering and diffraction from single XFEL pulses interacting with the droplets.

Droplet generation. Droplets of ultrapure water (Milli-Q Integral, MilliporeSigma, Burlington, MA, USA) and of water with ice-nucleating particles were generated using a 20-μm diameter glass nozzle equipped with a piezoelectric actuator (MJ-AT series, MicroFab Technologies, Plano, TX, USA). To maximize the data collection rate, the droplet generation parameters were adjusted during experiments. The drop diameter and velocities used in the data analysis were measured for each data group having the same generation parameters. The nozzle had a pressure differential of 1.6–1.9 bar and a flow rate of 11.3–12 mL/hour, and the piezoelectric actuator was driven by a 69 kHz sinusoidal voltage with 16–20 V peak-to-peak amplitude. The droplets had an initial temperature of 292 K, diameters ranging from 40.0 to 44.7 μm when probed, and velocities ranging from 16.0 to 18.1 m/s.

Samples for heterogeneous nucleation. For ATD-doped drops, 4.91 g of Arizona Test Dust (grade A1 Ultrafine, Reade Advanced Materials, RI, USA) were mixed in a glass vial with 44.2 mL of ultrapure water, sonicated, and left to settle for 6 hours. 11 mL of clear suspension were collected from the top of the vial, diluted ten times with ultrapure water, and then used to generate the drops. For AgI-doped drops, a colloidal solution with 1 mM concentration of AgI was prepared as described previously[4]. The colloidal solution was then diluted 50 times with ultrapure water and used to generate the drops. The particle sizes, determined with a nanoparticle tracking analyser (NanoSight, Malvern Panalytical) were 0.3±0.1 μm for ATD and 0.15±0.05 μm for AgI, and their concentration was of the order of 100 particles/drop for both samples.

Optical imaging. The optical imaging system was similar to the one described in ref.[34] except for (i) using only the right-angle imaging path and setting it perpendicular to the XFEL beam, and (ii) using a different illumination source that used multiple light pulses to characterize the kinematics of drops and split fragments[35]. A pulsed LED illuminator (IL-106B, HARDsoft Microprocessor Systems, Krakow, Poland) generated 200-ns blue light pulses (460 nm) at 200 kHz repetition rate. The illuminator had a much higher repetition rate than the XFEL (120 Hz) and produced trains of light pulses that were synchronized with each of the XFEL pulses.

Two different microscope objectives (long working distance apochromats, Mitutoyo) were used. A 20× objective was used for the primary two-exposure data producing images with a magnification of 497 nm/pixel and a resolution better than 780 nm. A 2× objective was used for the secondary 12-exposure data, producing images with a magnification of 5.1 μm/pixel and a resolution of 7.8 μm.

X-ray scattering and diffraction. The XFEL was operated in a self-amplified spontaneous emission mode and produced pulses with 40 fs duration, 9.5 keV photon energy, and 3 mJ average pulse energy at the XFEL source. The estimated beamline transmission was 0.4, and the XFEL pulses were further attenuated by factors from 0.009 to 0.331 to prevent detector damage, with more attenuation needed at longer times of flight. This resulted in average pulse energies at the drops from 0.01 to 0.42 mJ.

An aluminium disk was used to attenuate the crystal diffraction at low angles, enabling the collection of weak X-ray scattering at high angles. The post-sample attenuator was a polycrystalline aluminium disk with a diameter of 74.9 mm and a thickness of 0.5 mm. For experiments with pure water, the X-ray detector and the post-sample attenuator were located approximately 70 mm and 43 mm, respectively, from the droplets. For heterogeneous nucleation experiments, these distances were 66 mm and 41 mm.

Processing of optical images. The intensity of images was rescaled linearly to correct the loss of contrast due to multiple exposures[36]. From approximately one million two-exposure images recorded, a subset of ~50000 images likely to contain droplets was selected based on the image intensities. This subset was investigated frame by frame, and 20580 images containing drops with identified freezing stages were found. The 12-exposure image data contained 10855 images with approximately 34 drops per image; these images were investigated frame by frame to detect splitting events. Freezing stage probabilities, splitting probabilities, and additional freezing statistics shown in Extended Data Fig. 1 were determined via manual measurements. The images used for analysis and the code for linear rescaling have been deposited at the CXIDB data repository[37].

Processing of X-ray scattering data. A detailed description of the X-ray data analysis is available in the Supplementary Information, and the corresponding codes[38] are available at Zenodo. Only individual detector images that had a corresponding doubly-exposed optical image of the droplet were used. The geometry of the X-ray detector was refined[39] using accumulated X-ray diffraction images from ice crystals. The raw detector data for pure water drops was corrected for background noise, common mode noise, and polarization, and the raw data for drops with AgI or ATD was corrected for background noise and polarization. This corrected detector data was separated at the pixel level into crystal diffraction from ice crystals and diffuse scattering from the liquid. The separated data was corrected for the post-sample attenuation and then grouped by the freezing stage of the drops and by the pulse energy at the sample, averaged across the data groups, and integrated angularly to obtain the scattering intensities as a function of the photon momentum transfer. The absolute scattering cross-sections could not be determined because the scattered X-ray intensity depended on the X-ray pulse energy, the overlap of the droplet with the beam, and the volumetric fraction of ice. Total, crystal, and liquid scattering images were also assembled from the data groups by summation (see Fig. 4(a), Extended Data Figs. 6(a-c), 9).

The statistical uncertainties of the intensity values in the diffraction profiles were evaluated via bootstrapping. Single-shot diffraction profiles were sampled with replacement from the set of experimental profiles for a given freezing stage, then averaged into a test profile. The number of samples was equal to the number of experimental single-shot profiles, and 10000 test profiles were calculated. The mean and standard deviation of intensity at each Q point were calculated from the test profiles. Due to the large number of test profiles, the bootstrapped mean is very close to the simple mean of single-shot data and is indistinguishable from it in the figures. The bootstrapped standard deviation did not change substantially when the Q bin size was increased several fold, because the bin size is a few times smaller than the size of the elongated diffraction spots. For ice in stages 2–5, the stage-to-stage peak height differences of the (101), (102), (110), (103), and (112) peaks, whose changes during freezing were most prominent, are larger than their standard deviations. Between hidden ice in stage 1 and ice in stage 2, (112) changed by more than the standard deviation, while the other four peaks changed by approximately the same as their standard deviation in stage 1.

We note that the diffraction measurements represent a compromise between the linearity of the detector data and the ability to record scattering intensities that have a wide dynamic range due to the large difference in the diffracted intensities from the liquid and crystal phases. In some data sets, the first peak height may be underestimated due to detector saturation, the ones from 2.7–3.4 Å may be affected by detector noise, or the (200), (201) and (300) peaks may be under-sampled due to the detector geometry.

Extended Data Fig. 7(a) compares an experimental diffraction pattern from drops in stages 4–7 with a simulated diffraction pattern from a cylinder of hexagonal ice with 100 nm diameter, 100 nm height, and faces parallel to the basal plane. The simulation was performed using DIFFaX[40] v1.813, using the ice crystal model given by Malkin *et al.*[9] with the unit cell dimensions at 0 °C, no stacking defects, no strain, and scattering from oxygen atoms only. For an infinite crystal, this simulation reproduces the pattern given by Malkin *et al.*[9] for bulk ice. The peak heights simulated for the 100-nm ice cylinder are different, and illustrate the impact of crystal size and shape. The simulated pattern in Extended Data Fig. 7(a) also includes the instrumental broadening, which was calculated from the raw pattern generated by DIFFaX, using the wavelength distribution of the XFEL pulses (gaussian with 0.1% standard deviation).

Metastability of the strained hexagonal ice. Despite having the same basic crystal structure as the stable form of ice, the strained hexagonal ice has a higher energy that may allow transitions to other metastable forms of ice. The maximum elastic energy associated with the inhomogeneous strain, $K\varepsilon^2/2$ = ~5 J/mol, where K = 8.5 GPa is the bulk modulus of ice and $\varepsilon = 0.0076$ is the inhomogeneous strain from Fig. 4(b), is of the same order of magnitude as the 8 J/mol energy needed to induce a high density of stacking defects[41]. Also, the stacking defect energy is smaller than the energies that can be released through the annealing of crystal defects and interfaces[41]. Dendritic growth may be necessary for the formation of strained hexagonal ice, because water nanodrops, which are too small to form dendrites, freeze to ice with stacking defects and high cubicity within 100 µs of nucleation at ~50 K supercooling[42].

Models for evaporative cooling of liquid drops and spherically symmetric solidification of freezing drops. A detailed description of these models is available in the Supplementary Information, and the corresponding codes[43] are available at Zenodo. The drops were assumed to be spherical during evaporation and solidification, and their volume was divided into concentric spherical subshells. The evaporative cooling model (Extended Data Fig. 2(a)) computed the subshell temperatures by solving numerically heat equations that included the evaporative cooling at the surface and the thermal conduction inside the drop[44]. The solidification model (Extended Data Fig. 2(b)) tracked the inward growth of the solid ice shell. It advanced the freezing boundary by one subshell per time step, and calculated the duration of the time steps to determine the shell growth towards the centre of the drop. The temperatures of fully frozen subshells were calculated by solving numerically heat equations that included cooling at the droplet surface, heat conduction in the fully frozen shell, and heating at the freezing front due to the release of latent heat. The duration of the time steps was obtained by equating, at the freezing front, the heat fluxes due to thermal conduction in ice and due to latent heat release.

The models used a Crank-Nicolson scheme[45] (see Extended Data Fig. 2(c)) to solve the heat equations efficiently. The numerical convergence of the models is illustrated in Extended Data Fig. 2(d-f). The accuracy of the models was tested against experimental data[2,16,44,46,47] and analytical models[6] (see Extended Data Fig. 2(g,h))

Three versions of the solidification model were developed to evaluate the time in which isolated drops with 1–100 μm radii solidify when instantaneously exposed to vacuum, to air at atmospherically relevant conditions[48] (temperature, pressure and humidity), and to an oil matrix. The solidification times are displayed in Extended Data Fig. 2(i-k).

Seven-stage droplet freezing model. A detailed description of the freezing model is given in the Supplementary Information, and the corresponding codes[43] are available at Zenodo. The model was developed to be as simple as possible while providing a good match with the experimental data. For example, the model distinguishes between small and large spicules because the distributions of spicule heights at different times of flight (Extended Data Fig. 1(d)) indicated that the spicule growth occurred in spurts.

The freezing model tracks the droplet until the droplet reaches the probing region; it assigns the time and location of nucleation, calculates the duration of each subsequent stage, and assigns one of the terminal freezing stages (5, 6, or 7). The duration of stage 2 is determined by the dendritic growth velocity. The duration of stages 3 and 4 is given by fixed times. The duration of stage 5 depends on the end stage: it is implicitly infinite if freezing ends in stage 5 and is given by normally-distributed times if freezing ends in stages 6 and 7. The model was implemented numerically using subroutines for each of the stages. The subroutines calculate the end times of the freezing stages, which are stochastic values, and compare them with the time of flight. The simulation advances to the next stage if the end time is smaller than the time of flight, or ends the calculation otherwise. The main outputs of the simulation are the freezing stage at a given time of flight and the time elapsed between nucleation and the time of flight. Both the actual stage of freezing and one that would be observed in an image are calculated, because they can be different (Extended Data Fig. 3(c,d)).

The statistical behaviour of the freezing simulation was verified by calculating the distribution of freezing stages, and the standard deviation of drops in all freezing stages, using simulations of droplet ensembles. The distribution and their standard deviation of the number of drops in a stage are expected to have a binomial distribution. The droplet ensemble simulations were consistent with a binomial distribution, as shown in Extended Data Fig. 4(a-b).

Ice nucleation and dendritic growth rates from the freezing model. The modelled ice nucleation rate is shown in Extended Data Fig. 5(a) and applies to homogenous nucleation between 233.7 and 235.6 K. It is consistent with high-accuracy measurements at higher temperatures (235.4–237.9 K) on levitated[3] and microfluidic[4] drops, and with measurements at lower temperatures (226–232.5 K) on nanodrops[5,49]. The nucleation rate is also consistent with nucleation rate parametrizations that use a Vogel-Fulcher-Tammann dependence of the self-diffusion coefficient of water[50-52]. The modelled nucleation rate is inconsistent with a smaller ice nucleation rate measured between 229 and 232 K in another X-ray laser experiment on evaporatively cooled droplets, where the droplet sizes and the times of flight were not measured in situ[21]. Since in that experiment the drops were not imaged optically during data collection, it was not possible to quantify phenomena that can affect the measurement of nucleation rates, such as the spread of the droplet stream[36] and variations of the droplet diameter and velocities.

The growth rate of dendritic ice, 0.27 m/s between 233.7 and 235.6 K, is nearly the same as the extrapolation of Pruppacher's data[53] for dendritic ice growth in drops below 264 K, but is inconsistent with a reported maximum in the ice growth rate[10] near 255 K (Extended Data. Fig 5(b)).

Determination of the parameters of the freezing model. A detailed description of this procedure is given in the Supplementary Information. The model has 11 primary freezing parameters and 5 auxiliary parameters (Extended Data Table 1). The freezing parameters were determined by fitting the freezing model against the experimental data. The fitting consisted in minimizing the difference between the measured and simulated probabilities of observed freezing stages in the two-exposure image data, and between the measured and simulated splitting probabilities in the 12-exposure image data. This difference was quantified by an error function equal to the base-10 logarithm of the product of binomial probabilities of observing the measured numbers of droplets at the simulated probability. Codes for the calculation of the error function[43] are available at Zenodo. To reduce the statistical noise, the numerical freezing simulations were conducted at ten times the number of experimentally measured drops, and the determination of all freezing parameters required approximately one billion single-droplet simulations.

The error function depends on the parameters of the freezing model through the simulated probabilities. The error function has a stochastic output and was minimized in two steps. First, of the order of one thousand error function values were sampled near its minimum using a pattern search algorithm[54]. The sampled values were then fitted with a multidimensional parabolic function to improve the precision of the freezing parameters at the minimum of the error function. For part of the parameters the minimum was refined further using single-parameter scans of the error function followed by fitting with parabolic functions. The minimization procedure was applied sequentially using either the two-exposure and the 12-exposure data to determine the freezing parameters that were most sensitive to that part of the experimental data.

The overall validity of the parameter optimization procedure was tested by comparing the experimental and simulated numbers of split fragments observed in the two-exposure data, which were not used for the optimization procedure. The model predicts fragment numbers consistent with the experiment within the statistical fluctuations (see Extended Data Fig. 4(f)).

The statistical uncertainty of the freezing parameters (see Extended Data Table 1) was calculated as the change in the value of the parameter that led to a one standard deviation increase in the error function, along the parabolic fit function that was used to determine the minimum. The standard deviation of the error function was estimated as the standard deviation of the error function when the simulation was run with the same number of drops as in the experiment.

All numerical models and the determination of the freezing parameters were implemented as codes in MATLAB R2022a. The numerical calculations were performed on a Lenovo P620 workstation with a 64-core AMD ThreadRipper PRO 3995WX processor and 128 Gb of RAM.

Data availability

All optical image and X-ray scattering data used in this study have been deposited[37] at the CXIDB repository. Source data is provided in the online version for all figures including extended data.

Code availability

Codes for modelling cooling, solidification, and staged freezing[43] are available at Zenodo. Codes for processing the X-ray data[38] are available at Zenodo. Codes for extracting the optical images and X-ray scattering data have been deposited[37] at CXIDB along with the data.

Methods references

31 Liang, M. N. *et al.* The Coherent X-ray Imaging instrument at the Linac Coherent Light Source. *J. Synchrotron Radiat.* **22**, 514-519 (2015).

32 Emma, P. *et al.* First lasing and operation of an ångstrom-wavelength free-electron laser. *Nat. Photonics* **4**, 641-647 (2010).

33 Hart, P. *et al.* The CSPAD megapixel x-ray camera at LCLS. *Proc. SPIE* **8504**, 85040C (2012).

34 Stan, C. A. *et al.* Liquid explosions induced by X-ray laser pulses. *Nat. Phys.* **12**, 966-971 (2016).

35 Brownscombe, J. & Thorndike, N. Freezing and shattering of water droplets in free fall. *Nature* **220**, 687-689 (1968).

36 Stan, C. A. *et al.* Rocket drops: The self-propulsion of supercooled freezing drops. *Phys. Rev. Fluids* **8**, L021601 (2023).

37 Kalita, A. *et al. X-ray laser diffraction and optical image data from freezing supercooled water drops*. CXIDB ID 217 (CXIDB, 2023). https://dx.doi.org/10.11577/1973475

38 Stan, C. A., Marte, S., Kalita, A. & Mrozek-McCourt, M. *Separation of sharp and diffuse diffraction patterns from X-ray laser scattering of freezing water drops*. Version 1.0 (Zenodo, 2023). https://doi.org/10.5281/zenodo.7908740

39 Yefanov, O. *et al.* Accurate determination of segmented X-ray detector geometry. *Opt. Express* **23**, 28459-28470 (2015).

40 Treacy, M., Newsam, J. & Deem, M. A general recursion method for calculating diffracted intensities from crystals containing planar faults. *Proc. R. Soc. Lond. A* **433**, 499-520 (1991).

41 Hudait, A., Qiu, S. W., Lupi, L. & Molinero, V. Free energy contributions and structural characterization of stacking disordered ices. *Phys. Chem. Chem. Phys.* **18**, 9544-9553 (2016).

42 Amaya, A. J. *et al.* How Cubic Can Ice Be? *J. Phys. Chem. Lett.* **8**, 3216-3222 (2017).

43 Stan, C. A., Kalita, A. & Mrozek-McCourt, M. *Modeling of supercooling, solidification, and freezing stages of water drops*. Version 1.0 (Zenodo, 2023). https://doi.org/10.5281/zenodo.7908648

44 Smith, J. D., Cappa, C. D., Drisdell, W. S., Cohen, R. C. & Saykally, R. J. Raman Thermometry Measurements of Free Evaporation from Liquid Water Droplets. *J. Am. Chem. Soc.* **128**, 12892-12898 (2006).

45 Crank, J. & Nicolson, P. A practical method for numerical evaluation of solutions of partial differential equations of the heat-conduction type. *Proc. Camb. Philos. Soc.* **43**, 50-67 (1947).

46 Goy, C. *et al.* Shrinking of Rapidly Evaporating Water Microdroplets Reveals their Extreme Supercooling. *Phys. Rev. Lett.* **120**, 015501 (2018).

47 Ando, K., Arakawa, M. & Terasaki, A. Freezing of micrometer-sized liquid droplets of pure water evaporatively cooled in a vacuum. *Phys. Chem. Chem. Phys.* **20**, 28435-28444 (2018).

48 Rosenfeld, D. & Woodley, W. L. Deep convective clouds with sustained supercooled liquid water down to −37.5 °C. *Nature* **405**, 440-442 (2000).

49 Amaya, A. J. & Wyslouzil, B. E. Ice nucleation rates near ~225 K. *J. Chem. Phys.* **148**, 084501 (2018).

50 Zobrist, B., Koop, T., Luo, B., Marcolli, C. & Peter, T. Heterogeneous ice nucleation rate coefficient of water droplets coated by a nonadecanol monolayer. *J. Phys. Chem. C* **111**, 2149-2155 (2007).

51 Ickes, L., Welti, A., Hoose, C. & Lohmann, U. Classical nucleation theory of homogeneous freezing of water: thermodynamic and kinetic parameters. *Phys. Chem. Chem. Phys.* **17**, 5514-5537 (2015).

52 Koop, T. & Murray, B. J. A physically constrained classical description of the homogeneous nucleation of ice in water. *J. Chem. Phys.* **145**, 211915 (2016).

53 Pruppacher, H. R. Interpretation of Experimentally Determined Growth Rates of Ice Crystals in Supercooled Water. *J. Chem. Phys.* **47**, 1807-1813 (1967).

54 Hooke, R. & Jeeves, T. A. "Direct Search" Solution of Numerical and Statistical Problems. *J. ACM* **8**, 212 (1961).

Acknowledgments Use of the Linac Coherent Light Source (LCLS), SLAC National Accelerator Laboratory, was supported by the US Department of Energy, Office of Science, Office of Basic Energy Sciences under Contract no. DE-AC02-76SF00515. The experiments were supported by the US Department of Energy, Office of Science, Chemical Sciences, Geosciences, and Biosciences Division. A.K. and M.M.M. acknowledge support from the National Science Foundation under Grant No. 2123634 for developing the optimization algorithm used to determine the freezing parameters. Supplement funding for this project was provided by the Rutgers University–Newark Chancellor’s Research Office. We thank Eugene Han Dao and Sangsoo Kim for experimental assistance, Matias D. de Almeida and Ahmed Abdalla for an evaluation of the optical data, Gabriel Blaj for information on the X-ray detector, and Howard A. Stone for a critical reading of the manuscript.

Author contributions C.A.S. conceived and designed the study. C.A.S., S.B., P.R.W., J.E.K., M.J.H., R.P., and S.A.H.G. prepared the experiment. C.A.S., P.R.W., N.D.L., R.G.S., H.L., A.L.A., M.L. and S.B. conducted the experiment. T.F.K., M.M.M., A.K., S.M., and C.A.S. analysed the optical image data. C.A.S., S.M., M.M.M., A.K. and N.D.L. analysed the X-ray scattering data. A.K., M.M.M., and C.A.S. developed the models and determined the freezing parameters. C.A.S. wrote the manuscript.

Competing interests

The authors declare no competing interests.

Additional information

Supplementary information The online version contains supplementary material available at [].

Correspondence and requests for materials should be addressed to Claudiu A. Stan.

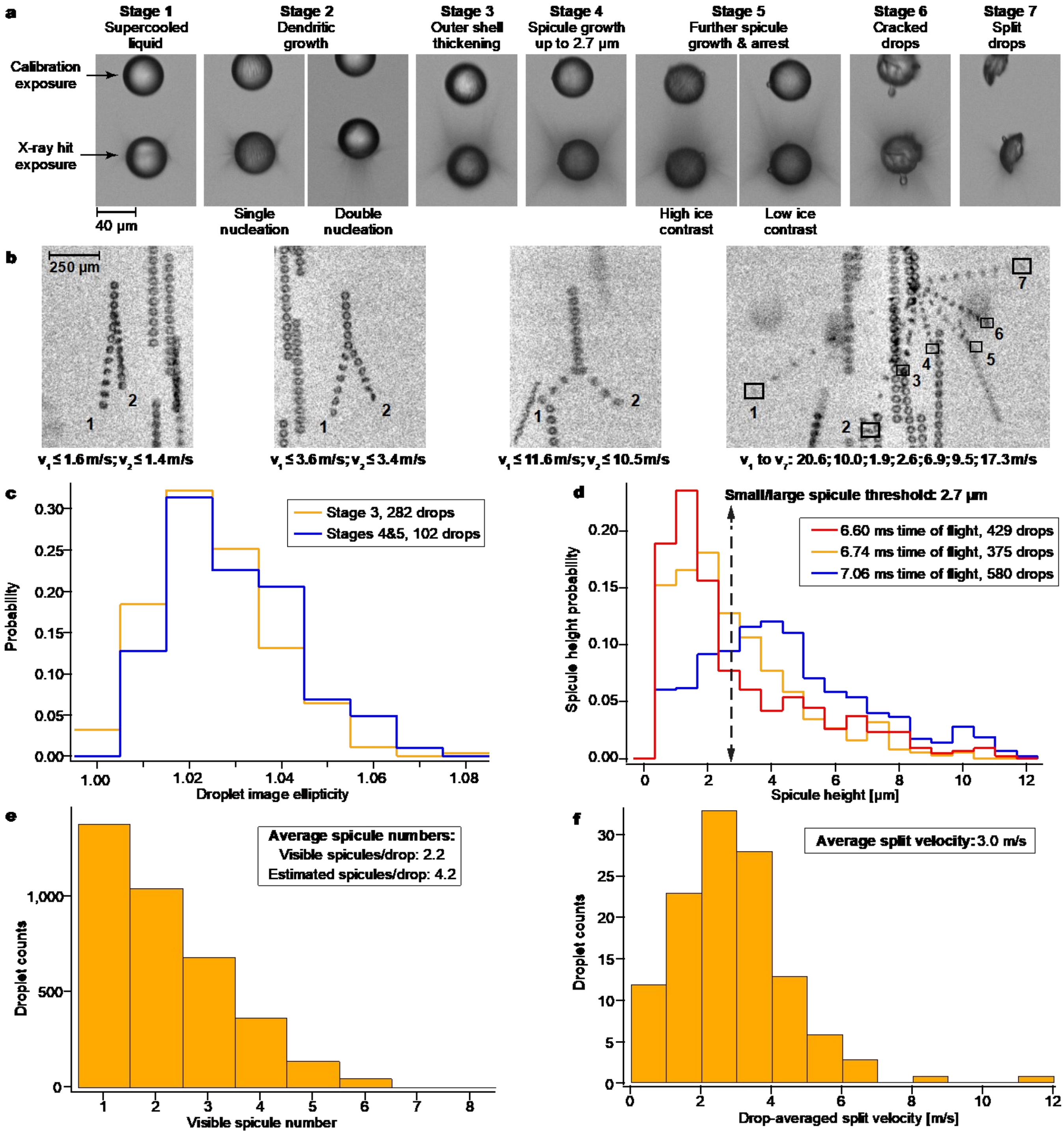

Extended Data Figure 1. Optical imaging and characterization of freezing processes. (a) Drops in different stages of freezing. The images show two exposures of the same drop, with the second (lower) exposure capturing the blowup due to the XFEL pulse. The droplets traveled from top to bottom in the images. (b) Drop splitting events captured using 12 exposures for each drop. The images illustrate the range of fragment velocities in binary fractures, and a 7-fragment fracture. The velocities measured from images may be smaller than the true velocity due to translations perpendicular to the image plane. (c) The ellipticity of droplet images indicates that the freezing-induced deformation is mostly complete before stage 3 of freezing. (d) Evolution of the distribution of spicule heights with the time of flight. The distributions evolved discontinuously, justifying the distinction between small and large spicules. (e) Distribution of visible spicule numbers. (f) Distribution of fragment velocities after binary fractures. The histogram displays the geometric mean of the fragment velocities.

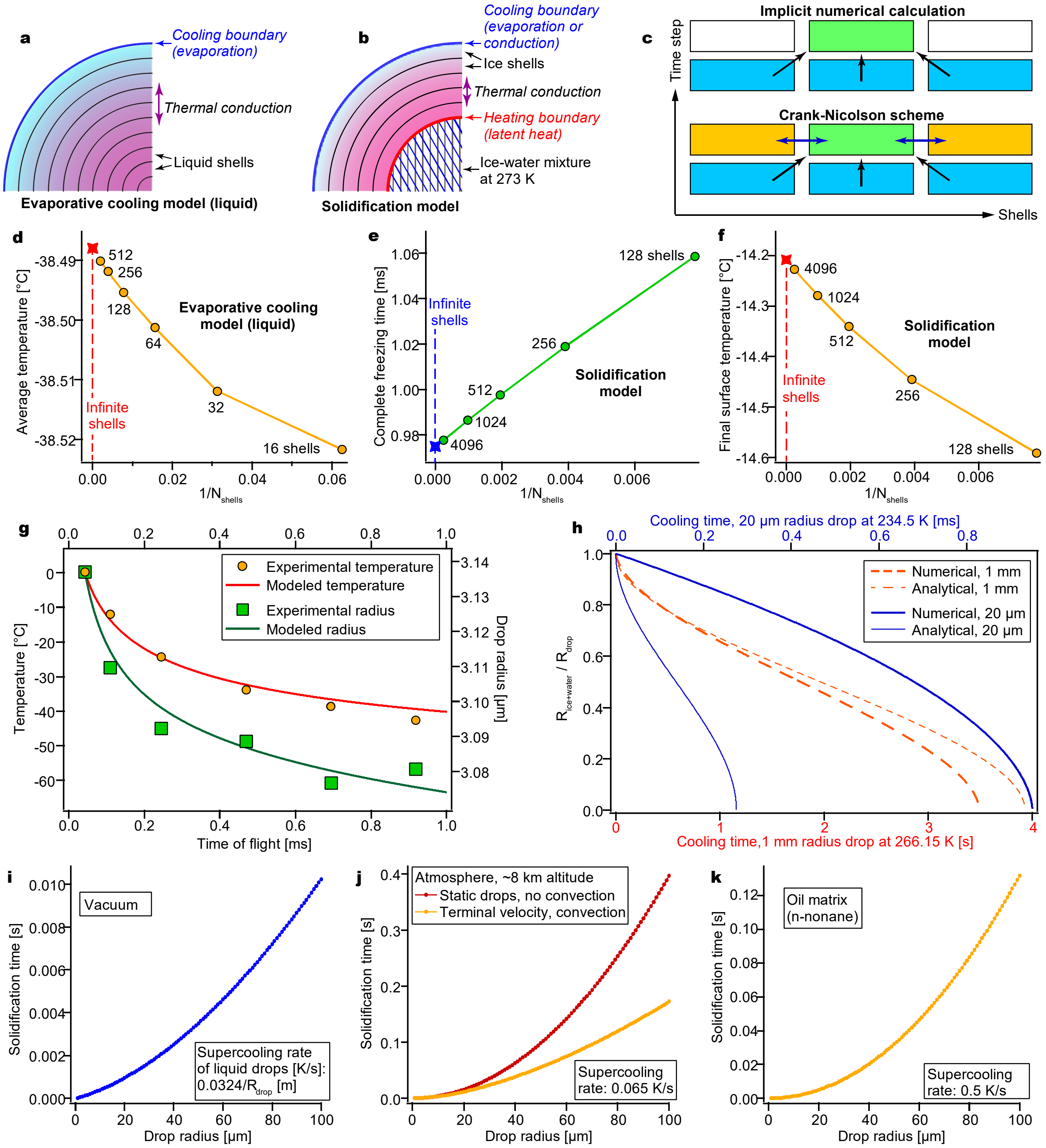

Extended Data Figure 2. Evaporative cooling and coarse solidification models. (a,b) Model geometries. (c) Implicit and Crank-Nicolson schemes. (d-f) The numerical convergence of the models. (g) Comparison of the cooling model with the measurements of Goy *et al.*[46] (h) Comparison of the solidification model vs. the analytical model of Wildeman *et al.*[6] (i-k) Modeled solidification times of an isolated 40.2-µm diameter drop, after the completion of dendritic ice growth, in three scenarios: evaporative cooling in vacuum, atmospheric cooling of stationary and free-falling drops in a standard atmosphere at ~8 km altitude (236 K, 34 kPa), and cooling in an oil matrix.

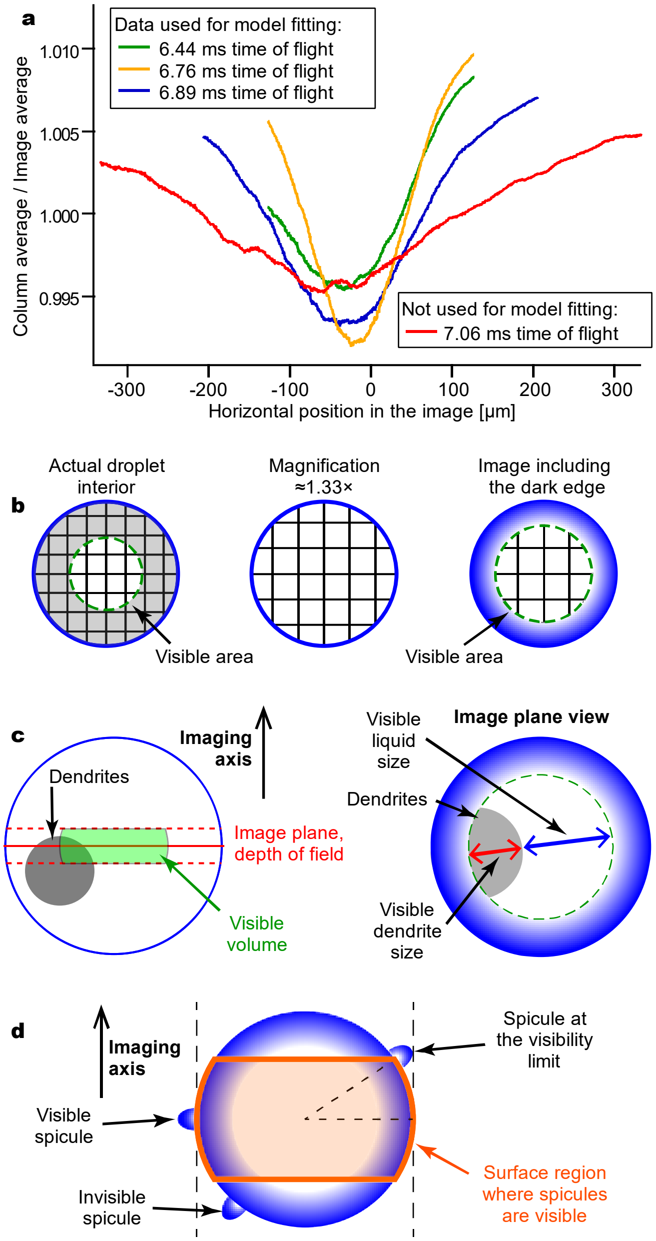

Extended Data Figure 3. Statistical and observational biases in the image data. (a) Vertically integrated image intensities for experiments with two optical exposures, recorded at different times of flight. The image intensity decreases as the number of drops observed at a given horizontal position increases. Freezing leads to an increase in the lateral spread of the drops[36], which can affect the stage statistics. To mitigate this statistical bias, only data up to 6.89 ms were used to determine the freezing parameters. (b) Illustration of the magnification of the image of the interior of the drop. (c) Stage 2 of freezing can be observed only if the ice region overlaps with the imaged volume and its size in the image exceeds a minimum size. The liquid region must also exceed this minimum size to identify the stage 2 in a freezing drop. (d) Spicules are visible only if they extend outside the drop image. This is equivalent to the spicules being visible only if they grew on a specific region of the drop surface.

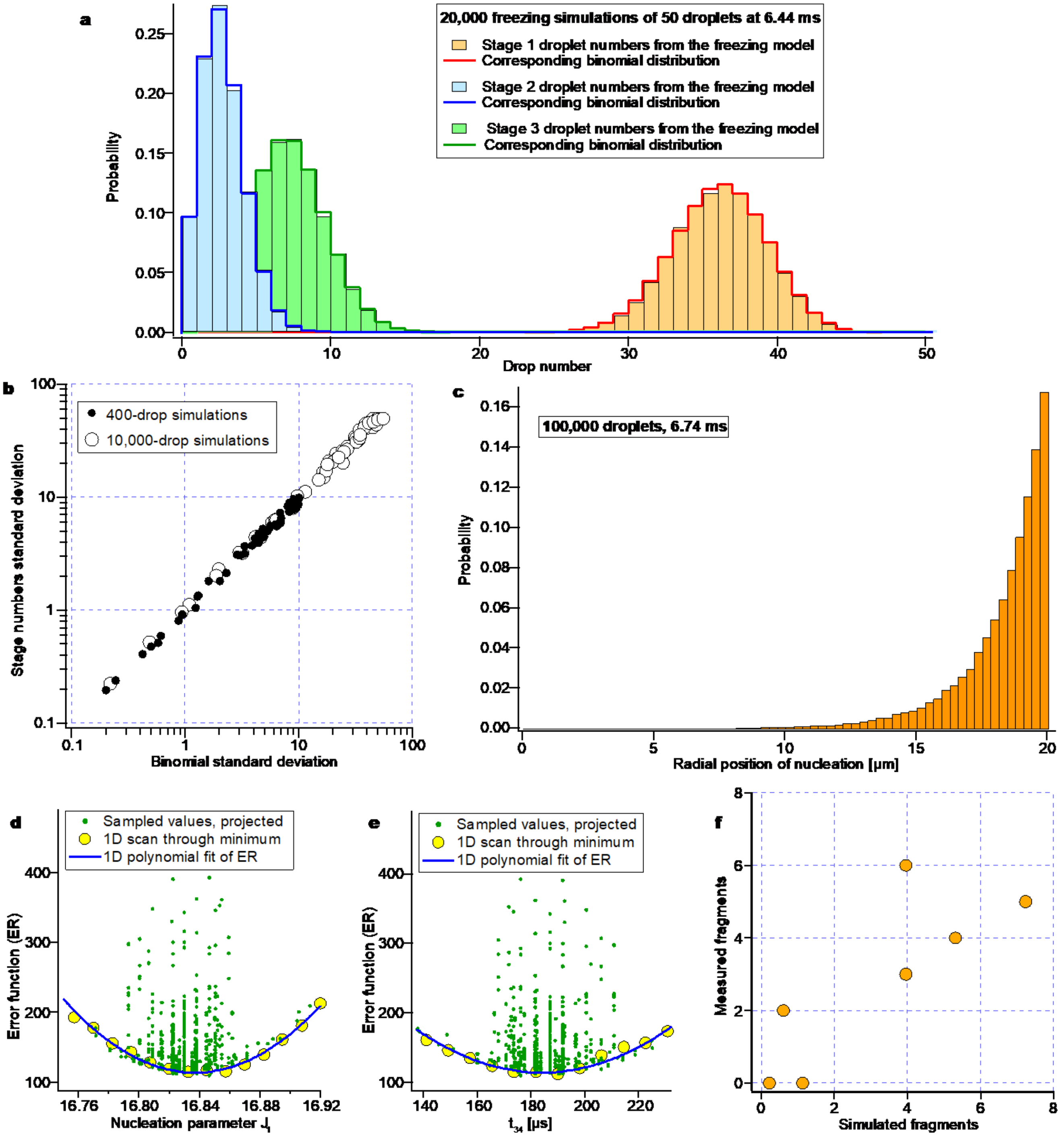

Extended Data Figure 4. Simulations of freezing drop ensembles and the determination of the freezing parameters. (a,b) Verification of the statistics of the ensemble simulations. The numbers of droplets observed in each stage have binomial distributions, and the standard deviations of stage numbers are equal to the binomial standard deviations. (c) The radial distribution of ice nucleation events. (d,e) Two-stage fitting of the parameters of the freezing model. Error function values were sampled near the minimum using a pattern search algorithm, then the error function dependencies on the parameters were fitted with parabolic functions to find the minimum of the error function. (f) Comparison of the numbers of drop fragments from experiments and simulations. The fragment numbers provide an independent test of the model because they were not used for the determination of the freezing parameters.

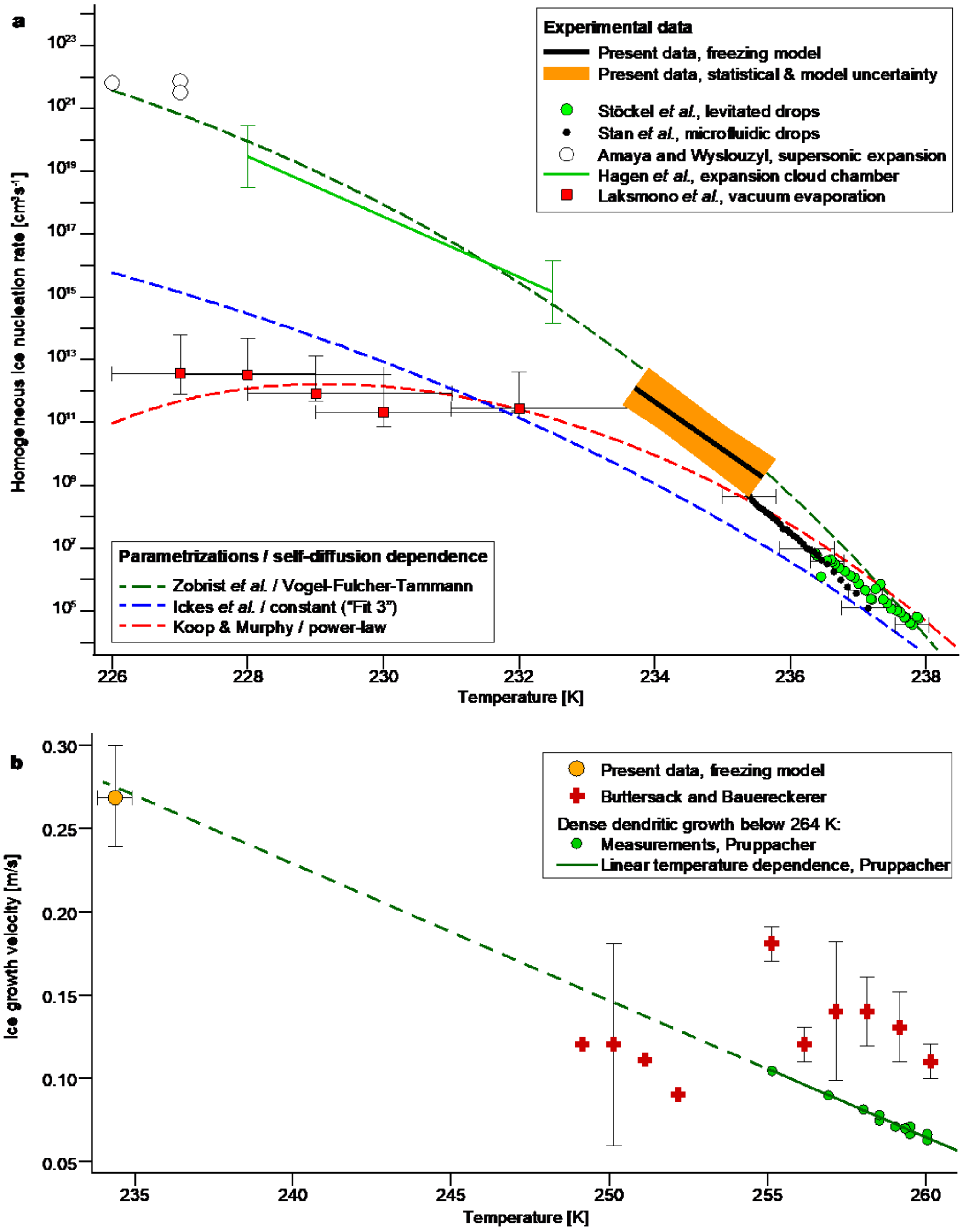

Extended Data Figure 5. Freezing model results. (a) The modeled ice nucleation rate is a parametrization valid between 233.7 and 235.6 K. It is consistent with several other measurements at both lower and higher temperatures, and with a parametrization based on a Vogel-Fulcher-Tammann temperature dependence of self-diffusion[50]. It is not consistent with another similar study conducted at an X-ray laser[21] or with parametrizations with constant[51] or power-law[52] dependencies of the self-diffusion. (b) The modeled dendritic ice growth velocity lies close to the extrapolation of Pruppacher's data[53] for the bulk growth of dense dendrites below 264 K, which scales linearly with the temperature. The error bars and bands represent the uncertainty of the freezing parameters (Extended Data Table 1) and of the temperature. For the literature data, the error bars are reproduced from the original work.

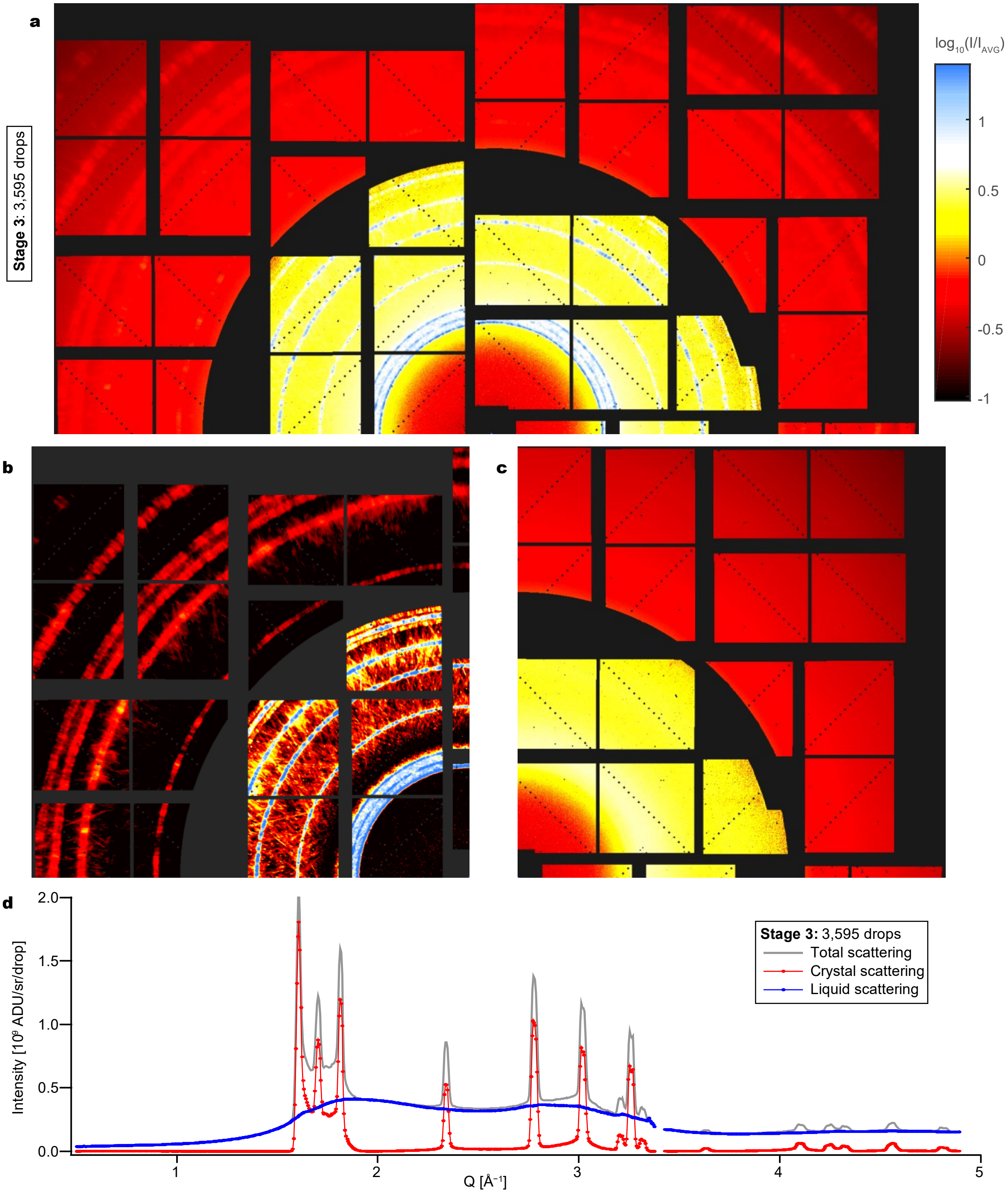

Extended Data Figure 6. Separation of X-ray scattering into crystal and liquid components. (a) Accumulated X-ray detector image from stage 3 drops (top half of the detector) (b) Corresponding separated image containing only the crystal diffraction. The intensity scale is shifted by −0.5 compared to panel (a). (c) Corresponding separated image containing only the liquid scattering component. The intensity scale is the same as in panel (a). (d) Total and separated scattering profiles.

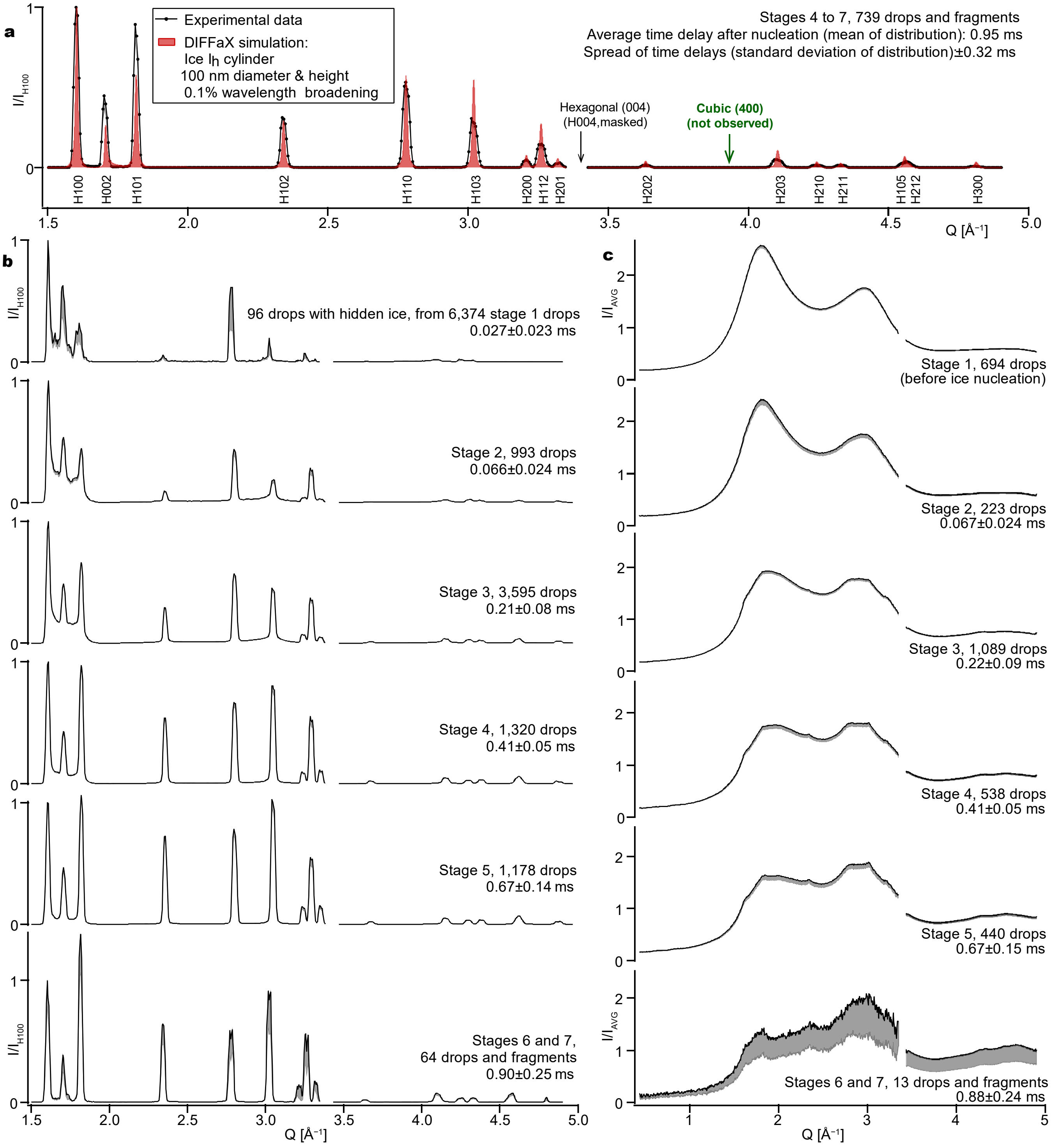

Extended Data Figure 7. X-ray crystal diffraction and liquid scattering during freezing. (a) X-ray diffraction from drops in the last four stages of freezing, recorded with 0.01 mJ XFEL pulses. This data was not affected by detector saturation. The panel also shows simulated diffraction pattern from a nanocylinder of hexagonal ice; the relative heights of the first three peaks are different from those simulated for bulk hexagonal ice[9]. (b) Evolution of X-ray diffraction from ice crystals, 0.13 mJ XFEL pulses. The height of some peaks was affected by saturation. (c) Evolution of diffuse X-ray scattering from the liquid, 0.42 mJ XFEL pulses. The liquid scattering data was not affected by saturation. In all panels, the standard deviations of experimental data, evaluated via bootstrapping over bands with $\Delta Q = 0.0025$ Å^{-1}, are shown as lower confidence bands at one standard deviation (Methods).

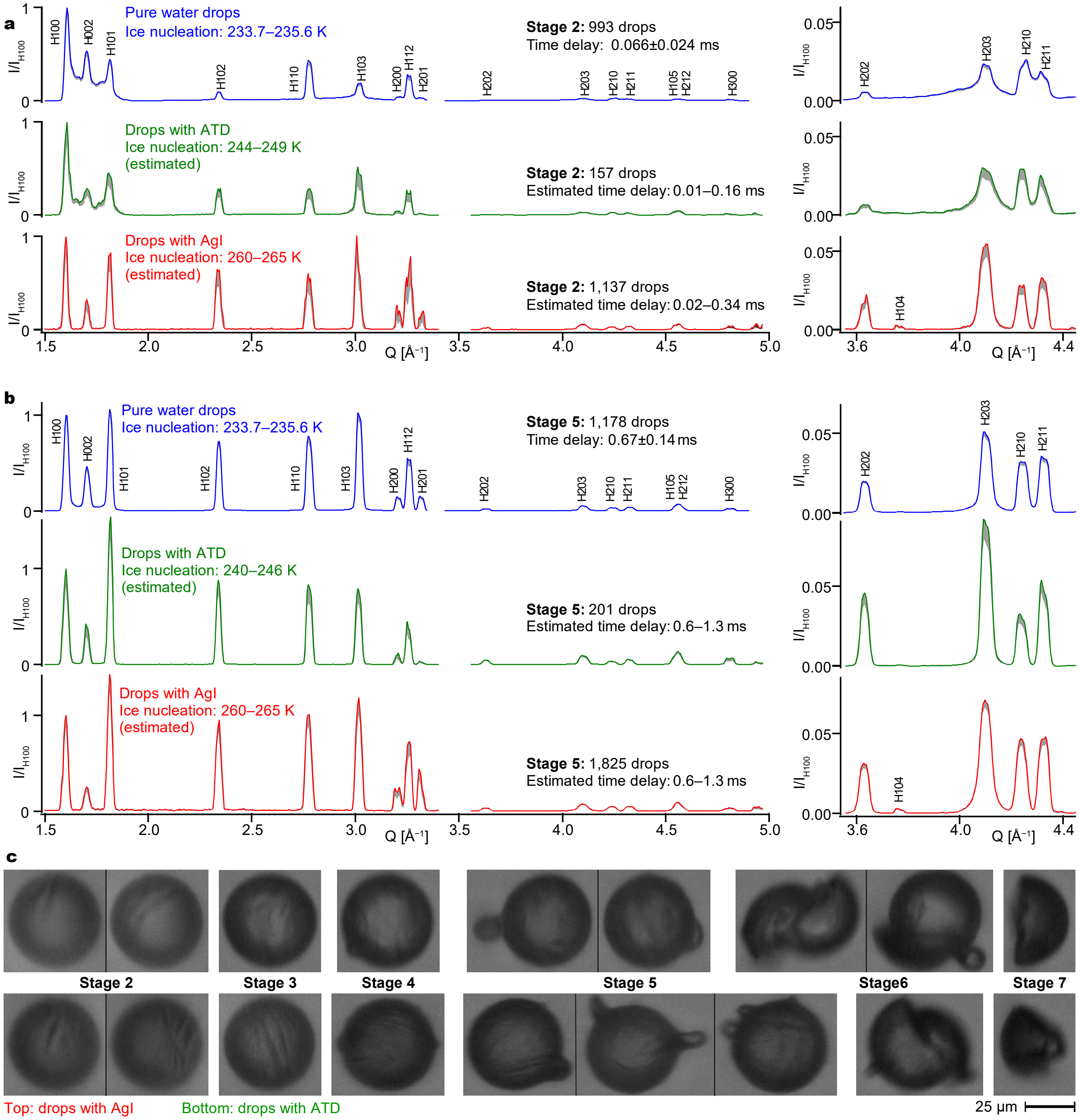

Extended Data Figure 8. Freezing after heterogeneous nucleation. (a) Diffraction from stage 2 drops of pure water (0.13 mJ XFEL pulses), doped with ATD (0.14 mJ) and doped with AgI (0.12 mJ). (b) Diffraction from stage 5 drops of pure water (0.13 mJ), doped with ATD (0.03 mJ) and doped with AgI (0.04 mJ). The left-side graphs in (a-b) display the entire *Q* range and the right-side graphs zoom on the lower height peaks at large *Q*. In panels (a-b) the standard deviations, evaluated via bootstrapping over bands with $\Delta Q = 0.0025$ Å^{-1}, are shown as lower confidence bands at one standard deviation (Methods). (c) Stages of freezing for drops doped with ATD and AgI. See the Supplementary Information for a description of how they differ from the freezing stages of pure water drops.

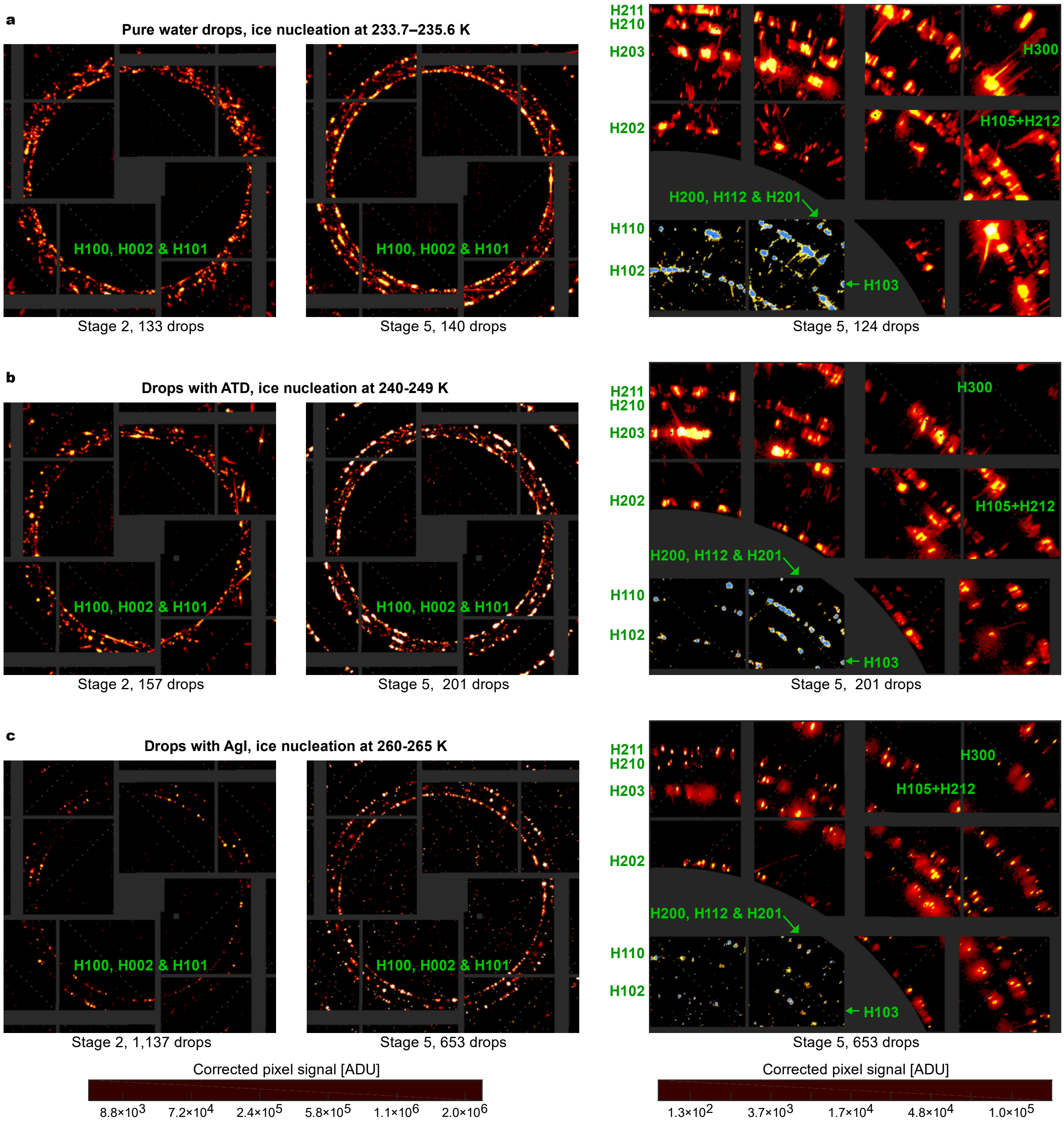

Extended Data Figure 9. Distribution and shapes of diffraction spots at different freezing temperatures and time delays. From left to right, the figure displays accumulated diffraction images of the first three diffraction rings during stages 2 and 5, and of the rings at medium and high diffraction angles during stage 5. (a) Pure water drops. During stage 2 the rings are not well defined due to spots from strongly strained crystals that appear between the rings. The spots at large diffraction angles display a large radial elongation due to inhomogeneous strain within single crystals. (b) Drops with ATD. The spots are similar to the ones from pure water. (c) Drops with AgI. There are substantially fewer diffraction spots per drop, and the first three rings are already well-defined during stage 2, indicating a higher degree of long-range order. The brightest spots at large angles are less elongated radially, indicating less inhomogeneous strain over the ~1 μm diameter regions probed by the XFEL beam.

Extended Data Table 1. Freezing model parameters for 40-μm drops freezing in vacuum after homogeneous ice nucleation, determined by fitting experimental data with the drop freezing model.

Parameter	Value	Statistical uncertainty	Description
		Freezing model parameters	
J_1	16.83	±0.03	Parametrized homogeneous ice nucleation rate J_N J_N [m^{-3}s^{-1}] = $10^{J_1+J_2(T-234.55\ \mathrm{K})}$
J_2	−1.5	±0.1	
V_{grow}	0.27 m/s	±0.03 m/s	Ice dendrite growth velocity
t_{34}	0.18 ms	±0.02 ms	Fixed duration of stage 3 (before spicules appear)
t_{45}	0.18 ms	±0.03 ms	Fixed duration of stage 4 (spicule growth up to a height threshold of 2.7 μm)
P_{56}	0.05	−0.04; +0.06	Probability of droplets cracking without separation
P_{57}	0.60	±0.04	Probability of droplets splitting into fragments
t_{56mean}	0.39 ms	±0.15 ms	Mean of normally-distributed elapsed time between threshold spicules and cracking
t_{56std}	0.17 ms	−0.17 ms; +0.31 ms	Standard deviation of normally-distributed elapsed time between threshold spicules and cracking
t_{57mean}	0.54 ms	±0.02 ms	Mean of normally-distributed elapsed time between threshold spicules and splitting
t_{57std}	0.30 ms	±0.04 ms	Standard deviation of normally-distributed elapsed time between threshold spicules and splitting
		Auxiliary experimental parameters characterizing the observability of freezing stages	
R_{vis}	13 μm	±2 μm	Actual radius of the visible region inside the drop
d_{Xmin}	2 μm	±2 μm	Minimum size of detectable ice or liquid regions
Y_{DOF}	12 μm	−5 μm; +4 μm	Effective depth of field for observing dendrites
P_{4H}	0.10	−0.10; +0.11	Probability of a stage 4 drop not displaying spicules
P_{5H}	0.015	−0.015; +0.09	Probability of a stage 5 drop not displaying spicules

SUPPLEMENTARY INFORMATION FOR:

Microstructure and crystal order during freezing of supercooled water drops

Armin Kalita,[1] Maximillian Mrozek-McCourt,[1,5] Thomas F. Kaldawi,[1,6] Philip R.Willmott,[2,3]
N. Duane Loh,[4,7,8] Sebastian Marte,[1] Raymond G. Sierra,[4,9] Hartawan Laksmono,[4,10] Jason E. Koglin,[2,11] Matt J. Hayes,[2] Robert H. Paul,[2] Serge A. H. Guillet,[2] Andrew L. Aquila,[2] Mengning Liang,[2]
Sébastien Boutet[2] and Claudiu A. Stan[1,4,*]

[1]Department of Physics, Rutgers University-Newark, Newark, NJ, USA
[2]Linac Coherent Light Source, SLAC National Accelerator Laboratory, Menlo Park, CA, USA
[3]Paul Scherrer Institute, Villigen, Switzerland
[4]Stanford PULSE Institute, SLAC National Accelerator Laboratory, Menlo Park, CA, USA

[5]Present address: Department of Physics, Lehigh University, Bethlehem, PA, USA
[6]Present address: Department of Physics, University of Rochester, Rochester, NY, USA
[7]Present address: Department of Biological Sciences, National University of Singapore, Singapore, Singapore
[8]Present address: Department of Physics, National University of Singapore, Singapore, Singapore
[9]Present address: Linac Coherent Light Source, SLAC National Accelerator Laboratory, Menlo Park, CA, USA
[10]Present address: KLA-Tencor, Three Technology Drive, Milpitas, CA, USA
[11]Present address: Los Alamos National Laboratory, Los Alamos, NM, USA

[*]email: claudiu.stan@rutgers.edu

CONTENTS

A. Optical imaging of freezing drops and freezing properties deduced from the optical data

Extended Data Fig. 1(a) shows doubly-exposed droplet images from the primary data set, where droplets were also probed by XFEL pulses. Extended Data Fig. 1(b) shows several splitting events from the auxiliary 12-exposure data. Since the multiple exposures reduced the intensity range of the image data, the intensity of images displayed in this study was adjusted from the original intensity by background subtraction and by linear rescaling for a higher contrast[36,37]. These image intensity adjustments used only linear operations to preserve the linearity of the drop images. The linearity of intensity was important for localizing the 50% intensity level at the edge of the drops, which defined the edge of the drops for measurements of their diameter and velocities. The 50% intensity level was determined with subpixel precision by fitting integrated image slices[55].

The two light pulses that illuminated the doubly-exposed droplet images were timed such that the second exposure was simultaneous with the XFEL pulse. For XFEL pulses with sufficient energy, the second exposure displayed the drop blowup due to X-ray laser ablation[34], which confirmed the proper alignment of the drops. The first exposure was taken 5 μs earlier and displayed the drop before it interacted with the XFEL pulse. The first image of the drop was used to measure the drop diameter, and both images were used to determine the drop velocity and its stage of freezing. Images of stage 2 droplets contained cases where two ice nucleation events occurred and the growing dendrites from both events were distinct. The visibility of ice patterns varied substantially, which is consistent with the solidification of a dense fan of dendrites with a platelet morphology, with the platelets perpendicular to a common plane. This type of ice dendrites was also observed in frozen drops that were previously supercooled to initial temperatures between 255 K and 268 K (see ref[53]).

The 12-exposure images enabled both the detection of splitting events and the determination of the fragment velocities in the image plane. The images shown in Extended Data Fig. 1(b) display three binary splitting events along with the fragment velocities in the droplet's center-of-mass reference frame, and a splitting event that produced seven fragments. The center-of-mass velocities were determined by dividing the fragment displacements between exposures by the 5 μs time interval between exposures, after subtracting the velocity of the parent drop. This procedure generates the fragment velocities in the plane of the image, but since the drops can have a velocity component perpendicular to the plane of the image, velocities displayed in the figure could be smaller than the actual velocities.

Extended Data Fig. 1(c) displays histograms of the ellipticity of well-focused images of drops in stages 3 to 5. These ellipticities show that the drops deformed slightly during freezing. The distribution of ellipticities had a very small variation between stage 3 and stages 4 and 5, indicating that the drop deformation primarily developed during the dendritic growth phase (stage 2). Since the development of the deformation occurred mostly during stage 2, the process of deformation was not included in the freezing model.

Extended Data Fig. 1(d) displays histograms of spicule heights in data sets collected at different times of flight. The histograms do not have a smooth variation with the time of flight and appear to switch between two differently shaped distributions between 6.74 and 7.06 ms. This suggests that the rate of growth of spicules was not continuous and justified the distinction between stage 4 (small spicules) and stage 5 (large spicules). The threshold between small and large spicules was chosen at a height that separated the peaks in the histograms at the earliest times of flight from the one at the largest time of flight.

Extended Data Fig. 1(e) displays the distribution of spicule numbers observed on stage 4 and stage 5 drops. The average number of spicules in this distribution was 2.2, but the actual number of spicules was larger because some of the spicules were hidden from view (see Extended Data Fig. 3(d)). Based on the average height of the spicules and on geometrical considerations, we estimated that the average number of spicules on the entire surface of the drop was 4.2.

Extended Data Fig. 1(f) displays the distribution of center-of-mass fragment velocities after binary splitting events. The data plotted in the figure are the geometric mean of the fragment velocities, which is equal to square root of twice the kinetic energy of the drop divided by its mass. We observed binary splitting events with mean fragment velocities ranging from below 1 m/s to approximately 11 m/s. In splitting events that produced more than two fragments, we observed velocities larger than 20 m/s; such a high-velocity fragment is shown in Extended Data Fig. 1(b).

B. Modeling of the evaporative cooling in liquid drops

Principle. The evaporative cooling of the water droplets was modeled numerically as illustrated in Extended Data Fig. 2(a), by dividing the drop into concentric shells with equal thicknesses, and by solving the heat equations for all shells at discrete time points. The inner shell temperatures were determined by heat conduction, while the outer shell was also cooled by evaporation. While this approach was used in several previous studies[2,44,46,47], our present implementation[43] uses a more stable and efficient numerical algorithm, has additional refinements, and may differ in its choices for the properties of supercooled water.

Numerical algorithm. The temperatures of the shells during evaporative cooling were calculated using the Crank-Nicolson scheme[45,56]. The difference between Crank-Nicolson scheme and the "default", or "implicit" method used in previous studies resides in the finite difference implementation of the heat equation (Eq. SE1). The implicit method evaluates the spatial differentials using the temperatures at the previous time step (Eq. SE2), while the Crank-Nicolson scheme uses the average at the previous and the current time step (Eq. SE3). In the Crank-Nicolson scheme the heat equation for a given subshell contains three unknown temperatures, but by considering the equations for all subshells a solvable linear system of equations is obtained.

$$\frac{\partial T}{\partial t} = \nabla(\alpha \nabla T) \qquad \text{(SE1)}$$

$$\frac{T_k^i - T_k^{i-1}}{\Delta t} = \frac{\alpha_k^{i-1}}{(\Delta r)^2}\left(T_{k-1}^{i-1} - 2T_k^{i-1} + T_{k+1}^{i-1}\right) + \frac{\alpha_k^{i-1}}{r_k \Delta r}\left(-T_{k-1}^{i-1} + T_{k+1}^{i-1}\right) + \frac{4}{(\Delta r)^2}\left(-\alpha_{k-1}^{i-1} + \alpha_{k+1}^{i-1}\right)\left(-T_{k-1}^{i-1} + T_{k+1}^{i-1}\right) \qquad \text{(SE2)}$$

$$\begin{aligned}\frac{T_k^i - T_k^{i-1}}{\Delta t} &= \frac{1}{2}\frac{\alpha_k^{i-1/2}}{(\Delta x)^2}\left[\left(T_{k-1}^{i-1} - 2T_k^{i-1} + T_{k+1}^{i-1}\right) + \left(T_{k-1}^{i} - 2T_k^{i} + T_{k+1}^{i}\right)\right] + \\ &+ \frac{1}{2}\left[\frac{\alpha_k^{i-1/2}}{r_k \Delta r} + \frac{4}{(\Delta r)^2}\left(-\alpha_{k-1}^{i-1/2} + \alpha_{k+1}^{i-1/2}\right)\right]\left[\left(-T_{k-1}^{i-1} + T_{k+1}^{i-1}\right) + \left(-T_{k-1}^{i} + T_{k+1}^{i}\right)\right] \qquad \text{(SE3)}\end{aligned}$$

In Eqs. SE1 to SE3, T is the temperature, r is the shell radius, α is the temperature-dependent and position-dependent thermal diffusivity of the material, Δt and Δr are the time step and the shell thickness. X_k^i is the value of the physical variable X for the cell at position index k and time index i. The state of the system is known at the previous time index, $i-1$, and must be calculated at the time index i; the time index $i-1/2$ represents a forward-extrapolated time for the calculation of the thermal diffusivity. We adapted Albert's implementation of the Crank-Nicolson scheme for a radiatively cooled sphere[56] by changing the radiative cooling term at the drop's surface with an evaporative cooling term, and by including the second-order terms in the heat equation that are proportional to the radial gradient of the temperature, dT/dr.

The difference between the two numerical schemes is further illustrated in Extended Data Fig. 2(c). The implicit method calculates the next temperature iteration of a shell based on the previous iteration temperature of the shell and of its neighbors, while the Crank-Nicolson scheme couples the temperature of a shell at the next iteration with the next-iteration temperature of its neighbors.

We found that the implicit method led to large numerical oscillations in the radial temperature profile. These oscillations can be suppressed by smoothing the temperature data after each time step, but the smoothing may affect the numerical accuracy. In contrast, the Crank-Nicolson method is stable and converges rapidly with the number of shells. We found that the most rapid numerical convergence was achieved when the shell thickness, δr, and the simulation time step, δt, are coupled by the diffusion time scale, i.e. $\delta t = \delta r^2/(2\alpha)$, where α is the thermal diffusivity of water at 234 K, near the ice nucleation temperature. Extended Data Fig. 2(d) shows the convergence of the average temperature for a drop from one of our data sets, with an initial diameter of 41.3 μm and an initial temperature of 292 K, after 6.56 ms time of flight in vacuum. The temperature for the limit of an infinite number of shells can be extrapolated with a precision better than 0.01 K. Even a coarse simulation with only 16 shells produces temperatures within 0.1 K of the infinite-shells limit, which represents a numerical precision better than the best temperature accuracy reported experimentally for measurements of ice nucleation in water microdrops[3], ±0.25 K.

General model refinements. The physical properties of water in each shell were calculated at forward-extrapolated temperatures corresponding to a time point halfway between the current time and the time of the next iteration ($i-1/2$ in Eq. SE3). The extrapolation was linear and used the slope of the current and the previous iteration. To initiate the extrapolation procedure, the water properties at the second time step were calculated using the properties at the initial time step; then the remaining time steps were calculated using properties at forward-extrapolated temperatures.

The rate of evaporation had two corrections. (i) The water vapor in the vacuum chamber condensed on the droplets and reduced the effective evaporation rate. To model this effect, the effective vapor pressure for evaporation was considered to be the difference between the vapor pressure at the droplet's surface temperature and the vapor pressure in the chamber. (ii) Collisions between evaporating molecules can cause some of the evaporated molecules to return to the drop, lowering the effective flux of evaporated molecules. This effect, which becomes more pronounced as the pressure increases and the Knudsen number decreases, was included in the code as a reduction of the evaporative flux according to the calculations reported by Sone *et al.*[57]

The mass loss due to evaporation and the corresponding change of the droplet radius were also calculated at each iteration. While the mass loss is proportional to the total evaporation rate, the droplet radius changed due to both mass loss and thermal expansion (supercooled water expands on cooling). After considering both processes, the new drop radius was calculated and the shell thickness was updated for the new radius.

Specific model refinements. In our experiments the drops were generated as a train of drops with a drop-to-drop separation comparable to the drop diameter, and a small amount of the vapor generated by neighboring droplets will condense on the drop. In vacuum, the drops carried an electrical charge that destabilized the lateral positions of the drops, initially in a zigzag pattern. We estimated that the lateral displacement of the drops due to the electrostatic repulsion scales with the fourth power of the time of flight for small lateral displacements, and we calibrated the lateral displacement during flight using an experimentally determined lateral displacement of 125 μm after 6.4 ms time of flight. This lateral displacement increases the drop-to-drop distance and changes the amount of vapor condensation from neighboring drops. The evaporative cooling model subtracts this time-varying condensation flux from the evaporation flux to correct for the presence of neighboring drops.

Another source of water vapor specific to our experiment was a catcher for the drops. The catcher had a 28-mm diameter circular aperture located 20 mm below the XFEL beam path. The catcher was connected to a dedicated vacuum pump, but due to its geometry it leaked back into the chamber a fraction of the vapor sublimated from frozen droplets in the catcher. Based on the vacuum conductance of the catcher, the chamber pressure and pumping speed, and the flux of water from the nozzle, we estimated that the pressure of the backflowing vapor at the catcher aperture was 37.5 Pa. While this pressure was much larger than the 0.4 Pa water vapor pressure in the main vacuum chamber, its total impact on the evaporative cooling was equivalent to an increase in the chamber pressure by only 0.1 Pa. The impact was small because the catcher vapor dispersed and because it acted as single-sided source of vapor that provides only about one quarter of the condensation rate from isotropic vapor. The evaporative cooling model calculated the condensation rate due to catcher vapor and subtracted it from the evaporation rate.

Experimental parameters. We developed two versions of the evaporative cooling code. One included all the refinements and was used in the droplet freezing model. The other included only the general refinements and was used to validate the evaporative model against experimental data from other studies.

The general evaporation code's input variables are the drop initial diameter and temperature, an evaporative coefficient γ, the vapor pressure in the chamber, the final time of flight, and the number of shells. The experiment-specific code adds the vapor pressure generated by the sample catcher, and instead of the final time of flight, it uses the droplet velocity and the total distance traveled. The distance traveled and the droplet velocity were needed to calculate the condensation rate due to the backflow of vapor from the catcher.

The evaporative coefficient γ represents the ratio of actual evaporative flux to the molecular flux calculated at the vapor pressure. While one study on evaporatively cooled drops[44] suggested that γ is less than 1, later studies[2,46,47] obtained results consistent with $\gamma = 1$, and we used $\gamma = 1$. In our model, a value of γ smaller than 1 can be used as an ad hoc correction for the condensation from neighboring drops, for experiments in which the droplet trains do not spread laterally.

The droplet radius and velocity were measured from optical images of well-focused, doubly exposed drops. The magnification of these doubly exposed images was measured at 497±1 nm/pixel using a resolution target, and represents the average of two calibrations done before and after the beamtime. The drop image measurements used a subpixel edge-detection algorithm[55] to determine (i) the drop radius in the horizontal direction and (ii) the vertical separation between the two drop images, from which the velocity was calculated by dividing the separation by the time interval between exposures (5 μs). The standard deviation of measured droplet diameters from the same experimental run was approximately 100 nm. The distance traveled by the drops from injector to the XFEL beam was measured by translating vertically the nozzle, from the position where it appeared in the image, to the data acquisition position. The distance traveled was equal to the distance between these two positions, which were reported by a linear translation stage encoded with a resolution of 0.1 μm.

The chamber pressure was measured using one of the chamber's pressure gauges and was 0.4 Pa during the measurements; since the chamber pressure dropped by a few orders of magnitude when the nozzle flow was turned off, the pressure measured during data acquisition represents water vapor pressure. The catcher backflow pressure was estimated at 37.5 Pa (see previous subsection *Specific model refinements*). The droplet initial temperature was assumed to be equal to the temperature of the last fluidic fitting connected to the nozzle, which was measured to be 292 K using an embedded thermistor.

Water properties used for modeling. The results of the evaporative cooling model, and of the complete solidification model (described in the next section), depend on the thermal properties of supercooled water and of ice: densities, thermal conductivities, specific heats, heats of evaporation and sublimation, and vapor pressures. For most of these variables direct measurements in supercooled water were not available at the temperatures at which ice nucleation occurs in our system (233.7–235.6 K), and the values used were determined from extrapolation of data available at higher temperatures.

The temperature-dependent density, thermal conductivity, and specific heat of ice were taken from Fukusako[58]. The heat of sublimation of ice was taken from Yen[59], who states a temperature-independent value of 2.838 MJ/kg.

The temperature-dependent vapor pressures of supercooled water and ice were calculated using the formulas given by Murphy and Koop[60].

The density of supercooled water was calculated using Amaya *et al.*'s parametrization[42] as given in their supplementary information.

The thermal conductivity of supercooled water is based on measurements by Bertolini and Tani[61], and by Saito *et al.*[62]. These measurements cover a temperature range from 244 K to 301 K. This data was fitted with a third-order polynomial and extrapolated to lower temperatures.

The specific heat of supercooled water. The least accurately known property used in our models is the specific heat of supercooled water, which increases rapidly with decreasing temperature near the ice nucleation temperature[1]. The value of the specific heat impacts the value of thermal diffusivity and the heat of vaporization. There are several different measurements of specific heat in the literature[60] that lead to significant differences in the modeled droplet temperature at the moment of ice nucleation.

We investigated three options for the value of the specific heat of supercooled water: a "lower" specific heat based on the measurements of Archer and Carter[63], a "median" specific heat based on the measurements of Angell *et al.*[1], and a "higher" specific heat based on the measurements of Tombari *et al.*[64]. These experimental measurements were fitted with 4th order polynomials and extrapolated to the ice nucleation temperatures characteristic to our experiment. Using an average droplet temperature of 234.15 K (an ice nucleation temperature typical for our experiment) and the "lower" specific heat as the reference parametrization, our evaporative cooling model predicts average droplet temperatures higher by 0.22 °C for the "median" parametrization and higher by 0.45 °C for the "higher" parametrization.

We chose to use the "lower" specific heat parametrization based on the analysis reported by Ando *et al.*[47], who found that this choice leads to the best consistency between their ice nucleation measurements on droplets cooled in vacuum, and the high-precision ice nucleation rates measured by Stöckel *et al.*[3] on single levitated droplets in air. For our experiment, the "lower" choice also leads to the best consistency between our derived ice nucleation rates and Stöckel *et al.*'s measurements.

We have also investigated if any of the specific heat parametrizations leads to a better overall consistency of the experimental data with the freezing model, defined as obtaining a smaller minimum value of the error function for the freezing model. We found that, within the numerical precision of our model, the degree of consistency was the same for all three specific heat parametrizations when applied to both our data and for Ando *et al.*'s data. This insensitivity of the overall consistency on the specific heat parametrization may indicate that the spread of specific heat data in the literature primarily reflects errors in the measurement of the temperature, which are very difficult to conduct accurately in deeply supercooled water. Systematic temperature errors, which are the primary cause of the spread of ice nucleation rate data in the literature[65], shift the temperature scale but otherwise have a negligible impact on the nucleation and freezing dynamics.

Verification of the evaporative cooling model against similar experiments and models. To verify our evaporative cooling model, we applied it to data from independent studies of freezing in evaporatively cooled water droplets in vacuum. We found that our evaporative cooling model was consistent with every previous experimental study that we tested against. Some of these studies disagree in their conclusions about the coldest achievable liquid droplet temperature or the evaporative cooling factor, but since our model is consistent with all, it is likely that the disagreements are due to systematic errors of the experimental parameters, especially the droplet diameters and the duration of evaporative cooling.

Verification case 1. Goy *et al.*[46] studied the evaporative cooling of water droplets with an initial diameter of 6372 ± 12 nm in vacuum, measuring the droplet diameter from Raman resonances and the droplet temperature using Raman spectroscopy. The evaporative cooling times were measured from the distance of flight in vacuum and the droplet velocity. The comparison between the data of Goy *et al.* and our model, for times of flight at which droplets were liquid, is shown in Extended Data Fig. 2(g). Our model is consistent with Goy *et al.*'s data for the droplet diameters. At the coldest data point for liquid droplets, Goy *et al.* measured spectroscopically a temperature of 230 ± 0.6 K while their optimized evaporative cooling model predicted a temperature of 234 K; our model predicts 233.8 K.

Verification case 2. Ando *et al.*[47] investigated the freezing of evaporatively cooled water droplets in vacuum with diameters between 49.2 μm and 71 μm, reporting the fraction of frozen droplets as a function of the time of flight in vacuum. The experimental measurements of droplet diameters from Ando *et al.* had a large uncertainty, and the authors reported both the measured droplet diameters and droplet diameters that were adjusted to achieve the best consistency of data from different drop diameters.

Our freezing model is more complex than the ice nucleation model used by Ando *et al*. While both models randomly assign ice nucleation events within the concentric drop shells used in the evaporative cooling model, our version also considers the time delay between the nucleation of ice and the time when it is observed experimentally. In Ando *et al.*'s experiment ice nucleation is detected through an increase of light scattering from the freezing droplets, but such scattering is expected to be negligible at nucleation. Therefore, we assumed that nucleation became detectable via light scattering when the rapidly growing ice-liquid mixture reached the center of the drop. We also modeled double ice nucleation events, while Ando *et al.*'s model considered only single ice nucleation events. Despite these differences between models, the fractions of frozen drops predicted by the freezing model were consistent with Ando *et al.*'s measurements.

Verification case 3. Sellberg *et al.*[2] studied supercooled water droplets using X-ray laser scattering and an experimental setup similar to ours but without in-situ optical imaging. Sellberg *et al.* considered limiting scenarios for the experimental parameters (droplet diameters and velocities, and vapor pressures in the vacuum chamber). They concluded that after 5.38 ms time of flight, droplets with a 34–37 μm diameter cooled to an average temperature of 233 ± 1 K. Our simulation for these two scenarios led to an average droplet temperature of 233.8 ± 0.7 K, where the limits of the uncertainty interval are given by the simulated temperatures for the two scenarios.

Verification case 4. Smith *et al.*[44] measured using Raman spectroscopy the temperatures of drops with radii between 6.5 and 20.3 μm evaporatively cooled in vacuum. We found that our model matches their data only if the evaporative cooling factor γ is around 0.7–0.75, somewhat larger than the value reported by Smith *et al.*, $\gamma = 0.62$. Since the hypothesis of an evaporative cooling factor different from 1 is inconsistent with later studies, the fact that our model also predicts $\gamma < 1$ for this data set suggests that our numerical model is valid, but Smith *et al.*'s drop diameters or times of flight data may have systematic errors.

Accuracy estimate. The evaporative cooling model depends on multiple experimental parameters, on thermal properties of water that have not been measured with high accuracy, and on the numerical implementation of the heat equation including refinements specific to the experiment. Due to the large number of dependencies, it is difficult to provide the uncertainty of the modeled temperatures with high accuracy.

We have tested multiple scenarios that would lead to different temperatures, such as uncertainties of droplet properties and of water properties, and ignoring some refinements in the model. The largest source of uncertainty is caused by the specific heat of supercooled water, where different choices lead to average temperatures different by 0.45 K, and surface temperatures different by 0.48 K. Other significant changes in temperature, around 0.3 K, can be caused by ignoring the water vapor pressure in the chamber or by doubling it, by an initial droplet temperature colder by 10 K, or by neglecting the $\nabla\alpha\nabla T$ term in the heat equation. Due to the high resolution of the optical images, the uncertainty due to drop diameters and velocities is smaller than 0.1 K in our experiment. Overall, we estimate that the temperature uncertainty in the evaporative cooling model (*i.e.*, the model uncertainty) is comparable to the largest sources of uncertainty, and equal to ±0.5 K. This temperature uncertainty was considered for the overall uncertainty of the nucleation rate measurements shown in Extended Data Fig. 5(a).

C. Modeling of a spherically symmetric post-dendritic solidification of a water drop

The time elapsed from the end of the dendritic growth phase to the complete solidification of the droplet was determined using a simplified numerical model[43] illustrated in Extended Data Fig. 2(b). During solidification the droplet is assumed to remain spherical while a concentric shell of fully solidified ice grows towards the inside of the drop until it reaches the center. The initial state is assumed to be a homogenous sphere of an ice-water mixture at 273.15 K. We calculated ice fraction, after the completion of the dendritic growth, considering the variation of the latent heat of melting with the temperature[22], which leads to Eq. SE4:

$$x_{ice} = \frac{1}{H^0_{melt}} \int_{T_{nuc}}^{T_{melt}} c_{p,scw}\, dT \qquad \text{(SE4)}$$

where x_{ice} is the mass fraction of ice in the mixture, H^0_{melt} is the latent heat of melting of ice at 0 °C, $c_{p,scw}$ is the specific heat of supercooled water, T_{melt} is the equilibrium melting temperature of 0 °C, and T_{nuc} is the ice nucleation temperature.

The droplet was divided into multiple concentric subshells with equal thicknesses. During solidification, thermal conduction in the fully solidified subshells transports the heat generated by the freezing of remaining liquid in the core to the surface of the drop, where the heat is lost via evaporation in vacuum. At each numerical step, a new mixed-phase subshell at the boundary of the fully solidified region was converted into fully solidified ice at the melting temperature. The time intervals of the numerical steps are not constant for two reasons: (i) the cooling power decreases during solidification because the surface of the droplet cools and the vapor pressure decreases, and (ii) the droplet has a spherical geometry, which causes a radial dependence of the thermal conduction rate and of the heating power due to freezing.

The growth dynamics of the solid shell is defined by the time intervals spent at each numerical step. The time intervals were determined through an iterative procedure. An initial time step, Δt_0 , is defined as the duration in which the outermost shell freezes due to the initial cooling power provided by the sublimation of ice at 0 °C:

$$\Delta t_0 = \rho H^0_{melt}(1 - x_{ice})\Delta r / j^0_{cool} \qquad \text{(SE5)}$$

where ρ is the water density, Δr is the subshell thickness, and j^0_{cool} is the heat flux due to evaporative cooling through the sublimation of ice. All physical parameters were taken at the equilibrium melting temperature.

Using the initial time step, the temperature distribution in the solidified subshells was calculated at each iteration using the Crank-Nicolson algorithm (see equation SE3). The implementation of the algorithm was the same as the one for the evaporative cooling of the liquid, except for: (i) introducing a new frozen subshell at each time step, (ii) using the thermal properties of ice instead of supercooled water, and (iii) in the equation for the innermost solid subshell, adding a heating term for the latent heat released during freezing. The temperature-dependent properties of ice used in the model were listed in the previous section.

The temperature distributions were then used to determine the thermal gradients near the freezing front, and the values of the time steps were adjusted to make the thermal conduction rate consistent with the heat released due to freezing. The adjustment was done by scaling the time steps by the thermal gradient near the freezing front, since the gradient is proportional to the heat flux and thus to the solidification velocity:

$$\Delta t_k = \Delta t_0 \left(T_3^4 - T_2^4\right) / \left(T_{k-1}^k - T_{k-2}^k\right) \quad \text{(SE6)}$$

where Δt_k is the freezing time of the k^{th} subshell (starting the count at the surface), and T^i_j is the temperature of the j^{th} subshell at the time step i. Since the model adds a new frozen shell at each time step, the k^{th} subshell freezes at the time step k. The initial state had four frozen subshells with the innermost subshell at the melting temperature just after freezing, and the thermal gradient was calculated using the temperatures of the two subshells that were closest to the just-frozen subshell (T^k_2 and T^k_3).

The temperature distributions and the adjustment of the time steps were calculated iteratively, starting with an initial set of constant time steps equal to Δt_0 and calculating the corresponding temperature distribution. The next iteration used this temperature distribution to refine the time steps according to Eq. SE6. For the physical conditions of our experiment, using two or three iterations leads to relative differences smaller than 10% in the total freezing duration. Our calculation used three iterations (an initial one using Δt_0 for all subshells, and two refinements).

The solidification model is less numerically stable than the evaporative cooling model. It requires subshells thinner than approximately 500 nm to avoid situations where the linear system of equations from the Crank-Nicolson scheme does not have a real solution, and the shell temperatures must be smoothed after each time step to prevent numerical oscillations. Small numerical oscillations of the temperature still occurred for approximately the first 20 time steps but damped afterwards. Since the very rapid rate of freezing near the droplet center made the calculations less accurate, we ended the simulation when the innermost four shells were still liquid. We addressed limitations of numerical stability and accuracy by using more subshells (up to 4096) than in the evaporative cooling model.

Calculation of solidification times for cooling in vacuum, air, and a hydrocarbon liquid. We developed two additional variations of the simplified solidification model for the freezing of drops in air and in a hydrocarbon liquid. For cooling in air, both thermal conduction and evaporation contribute to cooling, but evaporation has a smaller rate than in vacuum because it is limited by the diffusion of water vapor in the air. For a drop embedded in a liquid hydrocarbon, the only cooling mechanism is thermal conduction. We calculated the rates of cooling due to conduction and due to evaporation using Langmuir's models for small-sphere, diffusion-limited cooling and evaporation[66]. For cooling in air, we used thermal conductivity of air given by Stephan and Laesecke[67] and the diffusivity of water in air given by Marrero and Mason[68], taking into account both the temperature and the pressure dependence. For cooling in a hydrocarbon liquid, we used n-nonane as a model liquid for the oils used in emulsion freezing experiments, because the thermal properties of n-nonane are well defined and are available from a NIST database[69].

The solidification model for air included refinements beyond the small-sphere cooling model[66], which accounted for the effect of the finite size of the boundary layer and of convection[70]. These refinements were added to enable a precise comparison with the experimental solidification times given by Kleinheins *et al.*[16]. The finite size of the boundary layer (~4 mm at a plane surface[71]) leads to a ~5% increase in the cooling rates for drops of 345 µm diameter, and less than that for smaller drops; this effect was implemented in the model by scaling up the cooling power. We estimated the effect of full free convection by comparing the solidification times with and without convection given by Kleinheins *et al.*[16]. Full free convection reduces the solidification times by a factor of 0.89, consistent with the increase of heat loss rates due to free convection near hot wires[71]. Therefore, the effect of full free convection was estimated by multiplying the solidification times without convection by a factor of 0.89. To calculate the effect of forced convection we sampled the solidification time curves calculated by Kleinheins *et al.*[16] for a range of air velocities, and we empirically fitted the ratio of convective to diffusive cooling power as $P_{conv}/P_{diff} = 1.45*V^{0.49}$, where V is the air velocity in m/s. Both the finite size of the boundary layer and the forced convection increase the cooling power by numerical factors, which were used to multiply the cooling terms in the Crank-Nicolson numerical model. Convection also impacts the evaporation rate and cooling power. We modeled its impact on the evaporative cooling in air by multiplying the evaporative cooling terms by the same numerical factors as for conduction, because the Péclet numbers for water vapor diffusion in air and for thermal conduction in air differ by less than 10%. The terminal free-fall velocity of water drops in air was calculated as a function of drop radius and air pressure and temperature using the parameterization given by Beard and Pruppacher[72].

Extended Data Fig. 2 shows the simulated durations of post-dendritic solidification of droplet with radii from 1 to 100 µm in 1-µm steps, for three different scenarios. The scenarios were based on three freezing conditions: (i) Cooling in vacuum with 0.5 Pa water vapor pressure. The cooling rate was scaled inversely proportional to the radius of the drop using the conditions of our experiment, where 40.2-µm diameter drops cool at ~1500 K/s near the ice nucleation temperature. (ii) Cooling in a standard atmosphere[73] at an altitude of ~8 km, at an air temperature near 236 K and an air pressure of 34 kPa, assuming an air updraft of 10 m/s which leads to a cooling rate of 0.0065 K/s. (iii) Cooling in a n-nonane liquid environment at a cooling rate of 0.5 K/s, which was chosen to mimic emulsion cooling experiments that produced metastable ice with stacking defects[18]. This simulation is however different from freezing in a concentrated water-oil emulsion, where the large water fraction changes the thermal properties of the droplet's environment, and the freezing of other drops can heat up the emulsion.

The temperature of the liquid drop before freezing and the corresponding fraction of ice generated by dendritic freezing were calculated as the temperature where half of the drops would freeze due to homogeneous ice nucleation, using an exponential nucleation rate parametrization that extrapolates the measurements of Stöckel *et al*. All solidification simulations used 1024 subshells. The freezing times of drops in oil are approximately three times faster than the freezing times in stationary air, and similar to the freezing times of drops falling in air at the terminal velocity; the scaling of solidification times with the drop size is similar in oil and air because all cooling mechanisms have either diffusion-limited cooling rates, or rates proportional to them (for convection cooling). The duration of solidification in vacuum has a different scaling with the drop radius; it is comparable to the duration in oil for the smallest drops but approximately 10 times more rapid for the largest drops.

Numerical convergence. The convergence of the solidification time and of the surface temperature at the end of solidification are shown in Extended Data Fig. 2(e,f), for a 41.5-µm diameter drop with an initial ice fraction of 0.528, which corresponds to ice nucleation at 234.15 K, and an ambient pressure vapor of 0.5 Pa. The results, shown for numbers of shells between 128 and 4096, can be extrapolated to tightly defined values in the limit of an infinite number of shells. A simulation with 1024 shells is sufficient to obtain a freezing time within 1%, and a drop surface temperature within 0.1 K, of the values extrapolated to an infinite number of shells.

Physical accuracy. For our primary experimental data set, the predicted time elapsed between the end of the dendritic ice growth and completed solidification was 0.94 ms. This duration of post-dendritic solidification is consistent with the experimental observation of freezing dynamics, including splitting, over a range of time of flights of approximately 1 ms. These dynamic freezing phenomena should occur on the same timescale as the solidification, because they should either stop (spicule growth) or become improbable (cracking and shattering) after the solidification is complete and the internal pressure no longer increases.

Kleinheins *et al.*[16] measured the freezing times of 345-μm diameter water drops in stationary air between −26 °C and −5 °C. We modeled their experiment considering the finite size of the boundary layer. For the case of full free convection, our model predicts solidification times within ±2% of the experimental data, except for the coldest data point at −26 °C, where our model predicts a solidification time 4% shorter.

A different model of the solidification dynamics in supercooled water drops in (partial) vacuum was proposed by Wildeman *et al.*[6], who deduced an analytical formula for the position of the freezing front as a function of solidification time. This analytical model is compared with our model in Extended Data Fig. 2(h), for two different situations: (1) Wildeman *et al.*'s typical experimental conditions of a 2-mm diameter drop previously supercooled to 266.15 K in an equilibrium water vapor pressure of 340 Pa, which after dendritic freezing forms a phase mixture with an ice fraction of 0.089, and (2) a 40-μm diameter drop supercooled to 234.5 K in a pressure vapor of 0.5 Pa, which after dendritic freezing forms a phase mixture with an ice fraction of 0.523. Simulation (1) used 4096 subshells, and simulation (2) used 1024 subshells.

For both scenarios, our numerical model predicts different solidification times than the analytical model. There are two main reasons for this discrepancy. (i) The analytical model does not consider that part of the liquid in the core is already frozen, thus overestimating the heat that is generated during solidification; this omission increases the solidification time. (ii) The analytical model assumes that the ice at the droplet surface is in thermodynamic equilibrium with the surrounding water vapor and is therefore at a stationary temperature. This assumption overestimates the heat conduction rate through the solid shell and thus underestimates the solidification time. For 2-mm diameter droplets the analytical solidification time is slightly longer than our model because case (i) dominates. For 40-μm diameter droplets the analytical solidification time is approximately three times shorter because case (ii) dominates. Thus, the analytical model is appropriate for the millimeter-sized drops in Wildeman *et al.*'s study, but it fails when applied to our experimental conditions. The predicted analytical solidification time of approximately 300 μs is inconsistent with our experiment, when on average the droplets are about to start to grow large spicules, and thus have a significant liquid fraction.

D. Modeling of multistage freezing in supercooled water drops

D.1 Modeling of freezing in a single supercooled droplet

The freezing of a single droplet is a sequence of distinct processes associated with each of the freezing stages observed via optical imaging, as illustrated in the main text Fig. 2(a) and Extended Data Fig. 1(a): supercooled liquid and nucleation, dendritic growth, complete solidification of the outer shell, formation of small spicules, growth of small spicules into large spicules, and the fracture of the drops with or without separation of fragments.

Each of these processes was modeled separately using simulation subroutines implemented as MATLAB functions, and the entire freezing was modeled with a master simulation code that called the subroutines sequentially[43]. The simulation subroutines modeled the evolution of a droplet during a stage of freezing, until either the transformation to the next stage occurred or the droplet reached the end time of the entire simulation. This end time is equal to the time of flight of the drops, from their generation at the nozzle until they are probed experimentally. The primary outputs of the subroutines are the stage of the droplet and the simulation end time of the subroutine. If the transformation to the next stage occurs, the subroutine output is the next freezing stage and the time of the transition; if a transformation is not observed, the output is the current stage and the end time of the entire simulation. The master code compares the time output of the subroutine with the end time of the entire simulation, and calls the next subroutine if the time output is smaller than the end time. When the end time is reached, the master code reports the freezing stage of the simulated drop.

Since freezing starts with ice nucleation, which is a stochastic process, the output of the master code is also stochastic. The master code must be run for many drops to determine the probabilities of the freezing stages at a given time of flight.

During the simulation, the subroutines used as input and output a data structure that contains all the needed parameters, such as the droplet radius and time of flight. The subroutines added to the data structure the primary simulation outputs (the current freezing stage and the simulation time) and auxiliary parameters needed for the simulation of the next freezing stages. For example, a random location for the nucleation of ice was calculated in the first subroutine, and then passed to the dendritic growth stage subroutine to predict when the dendritic stage ends.

The modeling of freezing started with the calculation of temperatures in all the concentric shells at all discrete simulation times up to the final time of flight. The temperature and time data were written into specific fields of the data structure, and then passed to the subroutines.

A critical feature of the freezing model is the distinction between the physical stage of freezing and the optically observed stage of freezing. The physical and observed stages can be different if, for example, features such as ice crystals or spicules are not visible in the images.

D.1.1 Ice nucleation

The model assumed that ice nucleation is homogeneous, with a rate that depends exponentially on temperature according to the relation:

$$J_N = 10^{J_1 + J_2 (T - 234.55\text{K})} \qquad \text{(SE7)}$$

where J_N is the nucleation rate in $\text{m}^{-3}\text{s}^{-1}$, T is the temperature in degrees Kelvin, and J_1 and J_2 are nucleation parameters determined by fitting the experimental data. The reference temperature of 234.55 K is between the most probable nucleation temperature and the middle of the range of nucleation temperatures, and was chosen empirically to improve the numerical accuracy when using exponential functions. This type of parametrization is appropriate[65] when the range of ice nucleation temperatures is narrow (233.7–235.6 K in our experiment).

The subroutine calculates at each time step the probabilities of nucleation in all shells and compares these probabilities with random numbers uniformly distributed from 0 to 1. If one of the random numbers is smaller than the corresponding nucleation probability, an ice nucleation event is assumed to occur in that shell. The shell index, the radial location of nucleation (the shell radius), and the time step were recorded, and a random three-dimensional direction was also assigned to the nucleation event. All these results were written in the output data structure. Due to the fine discretization of the time steps (3 μs for a 32-shell simulation), the calculated probabilities in each shell were very small, and it was highly unlikely that the simulated nucleation occurred in more than one shell, but if that happened, one of the shells was randomly chosen as the nucleation location.

Simulation of double ice nucleation events. The search for ice nucleation events was continued after the first nucleation event, until either a second ice nucleation event occurred, or until the ice grew dendritically from the first nucleation position to the diametrically opposed point on the surface of the drop. The second ice nucleation event was simulated in the same way as the first event, detecting the radial position and the time of nucleation and assigning a random three-dimensional direction for the second nucleation. The subroutine then calculated whether the second nucleation point was within a spherically-grown region of ice-water mixture due to the first nucleation. If the second nucleation was observed in the mixed phase, this second event was ignored and the search for the second nucleation continued; if it was observed outside the mixed phase region, the second nucleation event parameters were recorded and the subroutine stopped. For the typical conditions of our experiment, approximately one quarter of the modeled ice nucleation events were double, and the rest were single.

If nucleation was not observed, the subroutine reported the current simulation time as being equal to the time of flight, and the physical and observed state of the drop as being liquid (stage 1). If nucleation occurred, the output of the subroutine contained the parameters (radial position, time, direction of nucleation) of the first nucleation event, and those of the second nucleation event in case it occurred. The subroutine marked the *physical* state of the droplet as being the dendritic ice growth stage, and passed the simulation to the next subroutine at the time of the first nucleation event. The *observed* state of the drop was marked as a liquid droplet, because right after nucleation the ice nucleus is smaller than the optical resolution and would not be visible.

D.1.2 Dendritic ice growth

The dendritic growth of ice was modeled as a spherical growth of an ice-water mixture. The assumption of spherical dendritic growth is consistent with the drop images, and with the movie from Stan *et al.*[4] for a drop with comparable sizes and temperatures. The region filled with dendrites was modeled to grow at a radial expansion velocity equal to an ice growth rate v_{grow}, which was determined by fitting the experimental data. While the actual dendrite growth rate is known to depend on the temperature, its variation over the range of drop temperatures in our data is expected to be small[53], and the model used a fixed growth rate. The corresponding subroutine calculated the duration of the dendritic ice growth. For single nucleation, the duration of dendritic growth is:

$$\Delta t_2 = (R_{N1} + R_D)/v_{grow} \qquad \text{(SE8)}$$

where Δt_2 is the duration of dendritic growth (stage 2), R_{N1} is the radial position of the first nucleation event from the nucleation subroutine, and R_D is the drop radius. For double nucleation, Δt_2 was calculated as the time when the entire droplet became filled with the phase mixture, which was the union of two spherical phase mixtures grown from the two nucleation points.

If the sum of the first nucleation time with the dendritic growth time was smaller than the time of flight, the subroutine advanced the simulation time by Δt_2, reported the physical and observed stages of the drop as having a solidified outer shell without spicules (stage 3), and exited. If the sum of times was larger than the time of flight, the subroutine reported the current time as being the time of flight and the physical stage of dendritic growth (stage 2). The subroutine also calculated the observed stage of the drop, which could be any of the stages 1 through 3.

Calculation of the optically observed state of the drop. The identification of the dendritic growth stage in our optical images requires that regions of both the ice-water phase mixture and of the supercooled liquid are visible. Also, since we imaged a part of the drop volume rather than its entire volume, these regions must be within the imaged volume.

The limitations of the optical system for imaging the inside of the drop are illustrated in Extended Data Fig. 3. In the images, the interior of the drop is magnified by a factor approximately equal to the refractive index of water[74].The imaged volume is restricted along the optical axis by the depth of field, and in the imaging plane by a combination of the dark obscured region near the edge of the drop and of the optical magnification. We quantified the experimental observability of the dendritic growth using three auxiliary parameters in the model: an effective depth of field, Y_{DOF}, the real-space radius of the region visible in the image, R_{vis}, and the minimum size of a mixed phase or liquid region that can be identified in the images, d_{Xmin}.

The criteria used to determine if the dendritic stage is observed are illustrated in Extended Data Fig. 3(c) for the case of single nucleation. A sphere of phase mixture was constructed, centered on the location of the nucleation point, and with a radius equal to the product of the ice growth rate with the time elapsed from nucleation. The criterion for observation is that both the phase mixture and the supercooled liquid must be present in the imaged volume and be larger than d_{Xmin}. The intersection between an image plane and the phase mixture is a circle, and in this plane the criterion for observation is that both the circle and the remaining liquid region must be larger than d_{Xmin}. Mathematically, this is equivalent to the requirement that the most advanced growth point of the phase mixture, in the radial direction, must have a radial position smaller than $R_{vis} - d_{Xmin}$. If this condition was satisfied, the droplet's observed stage was the dendritic growth (stage 2); if the phase mixture did not advance to this limit yet, the droplet's observed stage was liquid (stage 1); if the phase mix advanced past this limit droplet's observed stage was the one of having a solid outer shell around the phase mixture (stage 3). We note that our imaging system could not distinguish the solid outer shell from the phase mixture; we assigned the stage 3 classification (observed) when the ice was visible everywhere inside the drop and no spicules could be seen.

The criteria for determining the observed stage were evaluated both in the imaged plane (the equatorial plane of the drop) and at the planes that limit the effective depth of field. If they lead to different conclusions about the observed stage, additional criteria were applied to determine the stage. For example, the phase mixture could have grown sufficiently to be observed in one of the planes that limit the depth of field but not yet in the equatorial plane; in this case an observed stage 2 was assigned because the phase mixture advanced sufficiently somewhere in the imaged volume.

The criteria of observing in the image both a phase mixture region and a liquid region larger than d_{Xmin} were also applied to the case of double nucleation. The criteria were implemented using more complicated mathematical conditions than for single nucleation, since the growth of both phase mixture spheres had to be considered.

The values of the three imaging parameters relevant to the observability of stages 1 to 3 (Y_{DOF}, R_{vis}, and d_{Xmin}) were determined by fitting the freezing model against the experimental data. This resulted in the values R_{vis} = 13 µm, d_{Xmin} = 2 µm, and Y_{DOF} = 12 µm. These values are consistent with the optical properties of the system and the selection of data. R_{vis} was approximately the same as the radius of the visible region inside the drop images divided by an expected optical magnification of 1.33× (equal to the refractive index of water). d_{Xmin} and Y_{DOF} were larger, respectively, than the nominal optical resolution (0.7 µm) and the nominal depth of field (1.6 µm) of the microscope objective, but this is expected because the phase mixture is a translucent object with low optical contrast, and because we included in analysis out-of-focus drops whose center was up to ±10 µm away from the focal plane.

D.1.3 Outer shell solidification prior to the generation of spicules

After the completion of the dendritic growth, the drops formed a fully solidified outer shell that grew from the outside to the inside, until the first spicule appeared. This is the stage 3 of freezing, and the model for this stage assumes that its duration is given by a fixed time t_{34}.

The sum, t_4, of the current simulation time (t_3, the time at which the dendritic growth is complete) and t_{34} represents the elapsed flight time until the generation of spicules. If t_4 was larger than the total time of flight the spicules did not form; the subroutine updated the current simulation time to the total time of flight (thus ending the overall simulation) and reported a physical stage 3 and an observed stage 3. If t_4 was smaller than the time of flight, spicules were generated; the subroutine updated the current simulation time to t_4 and reported a physical stage 4 and an observed stage 3, since when the spicules form, they are too small to be resolved optically.

D.1.4 Spicule growth up to the small-spicule threshold

The growth of ice spicules on freezing drops was previously observed to be discontinuous, with the spicules growing to a certain size, followed by an arrest, and possibly by further cycles of growth and arrest[6]. Such a discontinuous spicule growth is consistent with the statistics of our data. Extended Data Fig. 1(d) shows histograms of spicule heights observed in data sets recorded at different times of flight. The peaks of the histograms shifted discontinuously to larger heights, with a spicule height of 2.7 µm separating the peaks at shorter times of flight from the one at the longest time of flight. We therefore defined the stage 4 of freezing as the one in which the drops have observable spicules with a height less than a threshold of 2.7 µm.

The subroutine for stage 4 modeled the evolution of the droplet from the apparition of small spicules until they grew to the threshold height of 2.7 µm. The model assumed that the duration of stage 4 is given by a fixed time t_{45}. The sum, t_5, of the current simulation time (given by the time at which the spicules appeared, t_4) and t_{45} represents the elapsed flight time until the appearance of large spicules with heights above 2.7 µm. If t_5 was larger than the total time of flight, large spicules did not form; the subroutine reported the current time as being the total time of flight (thus ending the overall simulation) and reported the physical stage 4. If t_5 was smaller than the time of flight, large spicules were generated; the subroutine updated the current simulation time to t_5, and reported the physical stage 5. The subroutine then calculated the observed stage of the drop, which can be either 3, 4 or 5 depending on whether the spicules were visible or hidden in the image.

Calculation of the optically observed state of the drop. Extended Data Fig. 3(d) illustrates how a droplet with spicules (physical stage 4 or 5) can appear as a droplet without spicules (observed stage 3). A single spicule will not be visible if it does not extend outside the projection of the droplet onto the imaging plane. For a given drop radius and spicule height, the spicule will be visible if the angle between the optical axis and the radial direction of the spicule is larger than a threshold angle. This threshold angle defines two regions on the surface of the drop: an equatorial band where a spicule will be visible, and two spherical caps where the spicule will be hidden. For a single spicule, the probability of being hidden is given by the fractional area of the spherical caps. The probability of multiple spicules being hidden, P_H, is given the probability of a single spicule being hidden raised to a power equal to the number of spicules.

Using an average number of spicules of 4.2 and the average spicule height of 3.54 µm (see Extended Data Fig. 1(d,e) for spicule height and number distributions), we estimated that the probability of a drop with spicules not displaying any of them was 0.043. This estimate has a low accuracy because it is based on the average spicule height. Therefore, the probabilities of all spicules being hidden for stage 4 drops, P_{4H}, and for stage 5 drops, P_{5H}, were determined by optimizing the match between experimental and simulated data, similarly to the procedure used for the optical parameters R_{vis}, d_{Xmin}, and Y_{DOF}. This procedure led to the values $P_{4H} = 0.10$, and $P_{5H} = 0.015$. As expected, the small spicules are more likely to be hidden than the estimate based on the average spicule height, and the large spicules are less likely to be hidden than the estimate.

To determine the observed stage, a random number with a uniform distribution between 0 and 1 was generated. If this number was smaller than the probability of being hidden (P_{4H} or P_{5H}, depending on the physical stage), the observed stage was 3; if it was larger, the observed stage was the same as the physical stage.

D.1.5 Cracking and splitting

Assigning an evolution branch. After the droplets reached stage 5 (large spicules), the model assumed that three possibilities for further evolution exist: (1) droplets remained in stage 5 indefinitely, (2) the droplets cracked but did not separate (stage 6), or (3) the droplets split into multiple fragments (stage 7). For all three cases, this was the last modeled transformation of the droplet. The model used two branching probability parameters: P_{56} for evolution into stage 6, and P_{57} for evolution into stage 7. The probability that a drop remains into stage 5 indefinitely is $1 - P_{56} - P_{57}$.

The subroutine for modeling droplet cracking and splitting treated all these cases. The evolution branch was chosen by generating a random number uniformly distributed between 0 and 1. If the random number was smaller than $1 - P_{56} - P_{57}$, the droplet remained in the physical stage 5 and the observed stage was either 3 or 5 depending on whether the spicules were visible, as described in the previous section. If the random number was larger than $1 - P_{56} - P_{57}$ and smaller than $1 - P_{57}$, the subroutine calculated the evolution of the droplet towards stage 6 (cracking without splitting). For the remaining cases, the subroutine calculated the evolution of the droplet towards stage 7 (splitting into fragments).

Modeling of cracking without splitting. Cracking was modeled to occur at a normally distributed time delay after the droplet formed large spicules, with a mean value t_{56mean} and a standard deviation t_{56std}. A random time delay Δt_{56} was generated using t_{56mean} and t_{56std}, and added to the current time delay (t_5) to obtain the predicted time of cracking, t_6. If t_6 was larger than the total time of flight, the drop did not crack; the subroutine updated the current time to the time of flight, reported a physical stage 5, and an observed stage of either 3 or 5 depending on whether the spicules were visible. If t_6 was smaller than the total time of flight, the drop cracked; the subroutine updated the current time to the final time of flight, reported a physical stage 6, and an observed stage 6. Unlike earlier subroutines, the updated current time was always the final time of flight since this is the last freezing process that is modeled.

Modeling of drop splitting. The subroutine for splitting is similar to the one for cracking but has additional features to model the departure of the split fragments from the imaged value, and to measure the splitting event probabilities from the auxiliary 12-exposure data set.

Splitting was modeled to occur at a normally distributed time delay after the droplet formed large spicules, with a mean value t_{57mean} and a standard deviation t_{57std}. A random time delay Δt_{57} was generated using t_{57mean} and t_{57std}, and added to the current time delay (t_5) to obtain the predicted time of cracking, t_7. If t_7 was larger than the total time of flight, the drop did not split; the subroutine updated the current time to the time of flight, reported a physical stage 5 and an observed stage of either 3 or 5 depending on whether the spicules were visible. If t_7 was smaller than the total time of flight, the drop split; the subroutine updated the current time to the final time of flight, reported a physical stage 7, and an observed stage 7. When splitting occurred, the splitting time t_7 was recorded by the subroutine, since this variable was necessary for simulating the experiments with 12 light exposures; if splitting did not occur t_7 had a preset value of zero. Same as for cracking, the updated current time was the total time of flight since this was the last freezing process modeled.

Modeling the number of split fragments visible in images. Split fragments present a challenge to the interpretation of experimental data because they can leave the imaged volume due to the lateral velocity imparted by splitting. This can induce significant errors in measuring the probability of not only stage 7 droplets, but also of the other stages, by lowering the number of observed drops in the ensemble. To mitigate the impact of splitting on data analysis, only part of the data was used for the optimization of freezing parameters, as described below in section E.1.

A precise modeling of the departure of split fragments from the imaged volume is difficult due to the wide range of fragment velocities (from 1 to 20 m/s), due to the variable number of fragments, and due to different fragment masses. To verify the accuracy of the entire freezing model, we developed a simplified splitting model which is expected to be less accurate than the rest of the model. Given the lower accuracy, this part of the model was not included in the freezing parameter determination procedure.

The model for the departure of split fragments defined an additional freezing parameter equal to the number of observed split fragments, which was set to zero initially. Two types of fragments are expected to be observed in the images: fragments that were also in the imaged volume before splitting, and fragments originating from the drops that were outside the imaged volume. Drops are present outside the imaged volume because the drops spread in flight, and we estimated that at the times of flight we investigated, the supercooled droplets had a peaked radial distribution in a cylindrical region with a radius of approximately 125 μm. This radius is larger than the ±10 μm image depth over which data was collected, and we estimate that approximately half of the injected droplets traveled outside the imaged volume. These droplets did not contribute to the counts of droplets in stages 1 to 6, but could send fragments into the imaged volume.

The drop splitting was modeled as a binary disintegration with equal and opposed fragment velocities equal to 3.4 m/s, which is the arithmetic mean of fragment velocities in binary splitting events from the 12-exposure data set. Events in which more than two fragments were generated were accounted for empirically, by setting the number of observed fragments to either (i) the experimental average number of fragments, 2.26, if both modeled fragments remained in the imaged volume, or (ii) half of the average number if only one of the modeled fragments remained in the imaged volume. To facilitate the comparison with the two-exposure image data, which detects individual split fragments, the model calculated the number of visible fragments rather than the number of drops that split.

If splitting occurred in the model, a random direction was set for the binary split, and the displacement of fragments was calculated along the horizontal direction of the image and along the imaging axis. The displacement was calculated using the split direction, the velocity of fragments, and the difference between the total time of flight and the time of split, t_7. If the horizontal displacement was less than half of the image width (127 μm) and the optical axis displacement was less than the image depth (10 μm), both fragments were assumed to be visible and the fragment number was set to 2.26. If the horizontal displacement was less than half the image width, and the optical axis displacement was more than the image depth but less than the estimated mean depth of out-of-focus drops (35 μm), only one fragment was assumed to be visible and the fragment number was set to 2.26/2.

D.2 Modeling of freezing in an ensemble of drops

Since the freezing of a single drop is a stochastic process, most of the properties of the freezing processes were calculated as average values after running the single-drop freezing simulation multiple times. We typically simulated ten times more drops than in the experimental data sets; this ratio represents a balance between being able to perform simulations in a practical amount of time, and having a smaller statistical noise in the simulations than in the experiment. To speed up the simulation, the code used a parallel loop to distribute single drop simulations to multiple computer cores. Although the single drop simulation outputs a data structure that contains all the parameters and variables of freezing, most of them are not required for the optimization of freezing parameters. The multiple-drop simulations generated a simpler output that contained only the single-drop freezing information needed for optimization, depending on the intended application of the model.

For the simulation of the primary data set with double optical exposures, the goal was to obtain the probabilities of observed stages at a given time of flight, and the output included a list of the physical and observed stages of each drop simulated; the number of split fragments from one drop was also included to compare the simulation with the experiments, since the two-exposure data contains observations of split fragments rather than splitting events. For the simulation of the auxiliary data set with 12 light exposures, the experimental data allowed only the determination of the splitting events, and the goal of the simulation was to detect the splitting events and their probability within a range of time of flights. The multiple-drop simulation for the auxiliary data reported a splitting variable that was zero if the drop did not split, or the splitting time otherwise. Other variants of the multiple-drop simulation were used to test the simulation or to characterize other features of freezing. For example, Extended Data Fig. 4(c) shows the radial distribution of ice nucleation events in an ensemble of 100000 drops with a diameter of 40.35 μm at 6.74 ms time of flight. The nucleation events occur predominantly at radii above 0.75 of the drop radius, due the outer parts of the drop having a larger relative volume and being ~1 K colder than the center of the drop. The average radial location of nucleation is at 0.91 of the drop radius, closer to the surface than in the case of equally probable nucleation, which has an average location at 0.75 of the drop radius[36].

Randomization and statistical tests. Due to the stochastic nature of ice nucleation, cracking, and splitting, each simulated droplet has a unique freezing process. To ensure this statistical character in simulations, the calculation loop for a single drop performed an extra randomization of the (pseudo)random numbers used by the simulation, by imposing a new seed for the random number generator. The random number generator used a Mersenne twister algorithm, and the algorithm's seed was updated for each drop as a function of both the current time and the loop iteration number.

For droplet-ensemble simulations at a given time of flight, the number of drops observed in each stage should follow binomial distributions. To test the proper statistical behavior of the freezing simulation, we ran the same droplet ensemble simulation multiple times. Extended Data Fig. 4(a) shows that the distribution of the number of drops in different stages was almost identical to the binomial distribution. A perfect match is not expected, as it can occur only for an infinite ensemble of drops.

Another test of the simulation statistics can be made by comparing the standard deviation of the number of simulated drops in one freezing stage with the standard deviation for a binomial distribution. Extended Data Fig. 4(b) shows the comparison of the binomial and the simulated standard deviations of drop numbers in all stages. The data in the figure was obtained from ensemble simulations with 400 drops and with 10000 drops, each running 100 times. The data points represent all the freezing stage numbers, simulated for all the experimental conditions in the primary data set. The binomial standard deviation was calculated using for the binomial probability the average probability of a stage from all the runs. The ratios of binomial and simulated standard deviations were close to one, which confirms that the freezing simulation produces data with the correct statistics.

E. Determination of the freezing parameters

E.1 Experimental data sets and corresponding fitting goals

The primary data set. The main data set consists of 17260 pairs of doubly exposed optical images and X-ray scattering images of distinct pure water drops. Out of this data set, 15631 optical images were selected for fitting the freezing model parameters. The selection of data for fitting was done in two steps to ensure that the experimental ensembles of droplets were statistically equivalent. First, we considered only doubly exposed droplets estimated to be within ±10 μm, along the imaging axis, of the focal plane. In this range, it is possible to identify all the freezing stages in the images despite some images being slightly out of focus, and the accuracy of identifying a freezing stage is improved by the presence of two images of the same drop. Outside this range of field depths, drops at the dendritic growth stage cannot be identified reliably, which would introduce systematic errors in the probabilities of freezing stages.

The second data selection criterion was to only use data if the droplet stream did not display a large lateral spread caused by splitting or by droplet self-propulsion during freezing[36]. The lateral spreading of drops is illustrated in Extended Data Fig. 3(a), which displays the average light intensity in vertical pixel columns from all images in an experimental run. Lower intensity values are caused by the presence of droplets, which appear darker in the images. The stream of drops was already spread before the first drops froze. The spreading rate increased when the drops started to freeze, particularly after the drops started to split with large lateral velocities. Since the spreading of drops was isotropic while the depth of detection was fixed at ±10 μm, spreading lowered the fraction of drops to whom a freezing stage be assigned. Also, the spreading biases the stage probabilities towards earlier stages of freezing because those drops are more likely to remain within the detection volume. Based on the data shown in Extended Data Fig. 3(a), we selected for fitting only data sets with times of flight up to 6.89 ms.

For the primary data set, the goal of the fitting was to determine which values of the freezing parameters lead to simulated stage probabilities that are as close as possible to the experimental data. This was difficult to implement for cracked drops and for split fragments due to spreading and due to the small probabilities (<0.01) and numbers (<10) of such drops in measurements up to 6.89 ms time of flight. Therefore, the practical purpose of the fitting for the primary data was to realize the closest match in the probabilities of stages 1 to 6; the freezing parameters relevant to stage 7 were instead determined by fitting the auxiliary 12-exposure data set.

The auxiliary 12-exposure data set. The auxiliary data set consists of 10855 images recorded with 12 light exposures at 5 μs intervals, at a magnification of 5.1 μm/pixel (approximately 10 times smaller than the in the main two-exposure data set). Six distinct experimental runs captured droplets with times of flight between 6.37 ms and 7.67 ms. Up to 12 images of a droplet were visible in one image frame if they stayed in the field of view, recording the droplet motion over up to (12−1)×5 μs = 55 μs, which was sufficient to observe and characterize splitting events. The data used for fitting were the times of flight at which the splitting occurred.

While more splitting events could be detected in the 12-exposure data than in the two-exposure data, the freezing stages of individual drops could no longer be identified due to the lower optical magnification. The imaged volume was much larger than in the main data set, with a lateral field of view of 2.8 mm, a vertical field of view of 4.9 mm, and an effective depth of field of approximately ±500 μm. On average, 34 droplets were visible in each image, because the 143-μm vertical spacing of consecutive injected drops was smaller than the vertical field of view. Given that the drops that split traveled laterally at most 500 μm laterally from the stream, and that the splitting is expected to be isotropic, all the splitting events were in principle observable. Nevertheless, some of the splitting events that occurred near the center of the droplet stream could not be detected because they were obscured by overlapping images from other drops. This effect manifested in a distribution of the lateral splitting positions that had a central dip, instead of a flat-top or a peaked distribution. We corrected the splitting event numbers by adding missed events such that the distribution had a flat top.

To compare the experimental data with the simulations, a probability of splitting must be calculated, which requires the total number of droplets investigated. We calculated this number by assuming that an experimental run is statistically equivalent to tracking the droplet stream continuously over a total time equal to the product of the number of images with the 55 µs drop tracking time. During the total time, the equivalent number of droplets tracked is given by the product of the total time with the droplet generation frequency of 69 kHz. This statistical approach is justified by the large number of images in the experimental runs (between 1040 and 4732 images), and translates into each image being statistically equivalent to tracking an average of 3.795 droplets across the whole vertical field of view. The number of droplets used to normalize the splitting probability was determined by multiplying the number of images in a run by 3.795. Therefore, the entire data set of 10855 12-exposure images was equivalent to tracking 41195 droplets across the entire field of view.

For the auxiliary 12-exposure data set, the goal of fitting was to determine the freezing parameters specific to splitting (P_{57}, t_{57mean}, and t_{57std}) that led to the best match between the measured and the simulated probabilities of splitting. These parameters could not be determined accurately by fitting the primary data set due to the loss of split drops from the statistical ensembles. For each of the six experimental runs, the vertical field was divided into five slices with equal heights, and in each slice the probability of splitting was calculated by dividing the number of observed splitting events by the equivalent number of drops in the respective run. The vertical limits of each slice were converted into time of flights using the measured drop velocity. This procedure led to 30 discrete probabilities of splitting, each within specific ranges of time of flights. The total number of drops for probability calculations was determined by multiplying the number of images in the experimental run by 3.795.

E.2 Determination of the freezing parameters from the primary and auxiliary data

Since the freezing parameters were constrained to different extents by the two experimental data sets, they were determined using the data that constrained them best. The primary two-exposure data had the best information on drops in stages 1 through 5 due to the large counts in these stages, and poor information on stages 6 and 7. The first step used the probability of drops in stages 1 to 5 to determine the freezing parameters that had the largest impact on these stages: J_1, J_2, v_{grow}, t_{34}, and t_{45}. The auxiliary model parameters (R_{vis}, d_{Xmin}, Y_{DOF}, P_{4H}, and P_{5H}) were also determined in this step.

The second step was to determine the parameters relevant to split drops (P_{57}, t_{57mean}, and t_{57std}) using the auxiliary 12-exposure data. The simulation of the 12-exposure data fixed the parameters determined in the first step and optimized only the parameters relevant to the splitting events.

The third step was the determination of parameters relevant to cracked drops (P_{56}, t_{56mean}, and t_{56std}), which can only be determined from the main data set. The simulations optimized these parameters while fixing all other at the values determined in the first two steps. The parameters relevant to cracked drops were the least constrained by fitting, due to the small number of cracked drops.

For a final verification of the determination of the freezing parameters, we compared the number of split fragments from simulations and experiments, in the primary two-exposure data. Splitting is the last freezing transformation in the model, and the numbers of split fragments in the primary data were not used for the determination of the freezing parameters, therefore this comparison tested the validity of the entire model. Extended Data Fig. 4(f) shows a plot of experimental counts of split fragments from different runs against the simulated number of split fragments. The simulated fragment numbers in the graph are fractional because they were scaled by the average number of split fragments per drop (see section D.1.5). The experimental numbers of split fragments are comparable to the simulated numbers, which we consider a good match given the complexity of the entire freezing simulation and the approximations made in the subroutine for modeling split fragments (section D.1.5).

E.3 The error function minimized during fitting

The criterion used for the calculation of the freezing model parameters is that the best set of these parameters will maximize the statistical probability of the experimental result. When this criterion is applied to measurements that are normally distributed, it leads to the well-known method of least squares minimization. Our raw measurements consist of the number of drops investigated, and of either the number of drops observed at a given stage of freezing (primary data set) or the number of drops that split in a range of time delays (auxiliary data set). Since these measurements are statistically described by binomial distributions and not by gaussian distributions, the sum of squared differences cannot be used. Instead, we defined an error function based on binomial probabilities.

Error function definition. The error function, ER, is based on the assumption that if an experiment or a simulation results in a number of drops k_{stg} from a number of recorded drops N_{stg}, the probability $Pr_{measurement}$ of this particular result is given by the binomial distribution P_{Bn} :

$$Pr_{measurement} = P_{Bn}\left(k_{stg}; N_{stg}, p^*_{stg}\right) = \binom{N_{stg}}{k_{stg}} {p^*_{stg}}^{k_{stg}} \left(1 - p^*_{stg}\right)^{(N_{stg}-k_{stg})} \quad \text{(SE9)}$$

where p^*_{stg} is either the probability of observing that stage (primary data set), or the probability of splitting (auxiliary data set). The binomial distribution of the simulated data was verified directly, as described in Section D.2. The probability of obtaining all the measurements from one experiment, $Pr_{experiment}$, is the product of the measurement probabilities:

$$Pr_{experiment} = \prod\nolimits_{all\ measurements} Pr_{measurement} = \prod\nolimits_{all\ meas.} P_{Bn}\left(k_{stg}, N_{stg}, p^*_{stg}\right) \quad \text{(SE10)}$$

The exact probabilities p^*_{stg} are not known. We approximated them with the numerically simulated probabilities, p_{stg}, which are a function of all freezing parameters, α_i :

$$p^*_{stg} \approx p_{stg} = p_{stg,simulated} = p_{stg}(\alpha_i) \quad \text{(SE11)}$$

We defined an optimization function, $OF(\alpha_i)$, calculated as the binomial probability of the experiment at the simulated stage probabilities. $OF(\alpha_i)$ will be maximized when the parameters have their true physical values:

$$OF(\alpha_i) = \prod\nolimits_{all\ meas.} P_{Bn}\left(k_{stg}; N_{stg}, p_{stg}(\alpha_i)\right) \quad \text{(SE12)}$$

Finally, we defined the error function $ER(\alpha_i)$ such that $ER(\alpha_i)$ will be minimized when the parameters α_i are equal to their true physical values, and $ER(\alpha_i)$ is convenient to handle numerically. $ER(\alpha_i)$ is the negative of the base-10 logarithm of the optimization function $OF(\alpha_i)$:

$$ER(\alpha_i) = -\log_{10} OF(\alpha_i) = -\sum\nolimits_{all\ meas.} \log_{10} P_{Bn}\left(k_{stg}; N_{stg}, p_{stg}(\alpha_i)\right) \quad \text{(SE13)}$$

Implementation for our data. For our experiment, the measurements to be included in the summation are either all the stage number measurements, or all the number of splitting events, from all the measurements relevant to fitting:

$$ER(\alpha_i) = -\sum\nolimits_{ms} \left(\sum\nolimits_{stg} \log_{10} P^*_{Bn}\left(k^{ms}_{stg}; N^{ms}_{total}, p^{ms}_{stg}(\alpha_i)\right)\right) \quad \text{(SE14)}$$

where *ms* is the measurement index, *stg* the stage index, P^*_{Bn} is a modified binomial probability described below, k^{ms}_{stg} is the experimental number of stage *stg* drops in the data set *ds*, N^{ms}_{total} is the number of drops in the experimental data set *ds*, p^{ms}_{stg} is the simulated probability of drops in stage *stg* within measurement *ms*, and α_i are the relevant freezing parameters for fitting.

In Eq. (SE14), a modified binomial probability, P^*_{Bn}, was used to prevent infinite negative values of *ER* when one or more of the simulated probabilities p^{ms}_{stg} are equal to zero, which can occur either due to using a finite number of simulated drops, or due to p^{ms}_{stg} being less than the smallest real number that can be represented numerically. To prevent infinite negative values while also retaining the ability of the error function to report very small stage probabilities, for $p^{ms}_{stg} = 0$ the modified binomial probability P^*_{Bn} was set to the smallest real number that can be represented in MATLAB, 2.225×10^{-308}:

$$P^*_{Bn}\left(k^{ms}_{stg}; N^{ms}_{total}, p^{ms}_{stg}(\alpha_i)\right) = \begin{cases} P_{Bn}\left(k^{ms}_{stg}; N^{ms}_{total}, p^{ms}_{stg}(\alpha_i)\right), \text{if } p^{ms}_{stg}(\alpha_i) > 0 \\ 2.225\times10^{-308}, \text{if } p^{ms}_{stg}(\alpha_i) = 0 \end{cases} \tag{SE15}$$

E.4 The fitting algorithm for the determination of freezing model parameters

Mathematically, the freezing simulation is a multidimensional function of the freezing parameters with a stochastic output (*i.e.*, for a given set of freezing parameters, the stage and splitting probabilities will be different for each simulation run). The variance of these probabilities decreased with the number of drops that were simulated but remained significant for the number of drops that could be practically simulated. Thus, the noisy experimental data were fitted with a numerical function that was also noisy.

Due to the stochastic noise of the simulations, multidimensional fitting algorithms based on gradient searches were inefficient. Instead, the data was fit to the model using a hybrid procedure, in which a "pattern search" algorithm[54] was first used to locate and sample the multidimensional minimum of the error function, followed by the determination of the freezing parameters by analytical fits of the sampled values.

Locating and sampling the error function minimum. To locate the minimum of the error function, we used a customized pattern search algorithm. The pattern search is a type of direct search algorithms[54], and operates by "polling" function values near an initial point in the multidimensional space defined by all the function parameters. The polling points are obtained by increasing or decreasing one of the function parameters by a fixed differential, and the complete polling set is obtained by performing this procedure on all parameters. If the error function at one of the polling points has a lower value than the value at the initial point, this polling point becomes the starting point for a new polling iteration, and the parameter differential is doubled. If the initial point has the smallest error function, the starting point remains the same, and the parameter differential is halved.

The pattern search is particularly effective when the fit function is stochastic, because the repeated polling of the function enables the algorithm to escape from false local minima. Such minima are caused by the error function returning, with low probability, values at the low end of its statistical range. This escape ability decreases as the true minimum is approached, and the search will practically end at a point that is near the true minimum. To achieve a closer approach of the true minimum, the noise of the fit function must be reduced, which can be achieved in the freezing model by increasing the number of simulated drops.

In principle, it is possible to determine the error function minimum with a high numerical precision by using the pattern search algorithm with simulations of very large numbers of drops. We did not follow this approach because the noise of the model decreased too slowly with the number of drops, requiring simulations with impractically large numbers of drops.

Instead, our approach was to use the pattern search algorithm to generate a noisy set of error function values, starting near an approximate minimum that was found through a preliminary search. The set consisted of all *ER* values returned during the polling process. These values were then fit to determine the minimum by fitting them with a multidimensional parabolic function.

To implement this approach, we customized the MATLAB implementation of the pattern search algorithm. The customized pattern search had three critical modifications. First, the parameter differentials were set to distinct values for each parameter, such that the change in the error function near its minimum, when one parameter was varied by its differential, was approximately the same for all parameters. This ensured that all parameters were optimized at similar rates. Second, if after a small number of consecutive iterations (typically three) the center point did not change, the *ER* value for the center point was recalculated. This ensured that the algorithm did not remain pinned in a false minimum. Third, the algorithm did not update the center location and the parameter differentials unless the maximum absolute difference between the center and the polled points was larger than a preset threshold proportional to the standard deviation of the error function. This feature can be used to restrict the pattern search to a small region near the minimum.

The sampling of the error function near the minimum is illustrated in Extended Data Fig. 4(d,e) for two freezing variables: the nucleation rate parameter J_1 and the duration of the stage 3, t_{34}. The data was generated via a pattern search in which the probabilities of the first five freezing stages were fit against simulations in which the first five freezing parameters and the first three auxiliary experimental parameters (see Extended Data Table 1) were varied. The graphs display the sampled error function values from the multiparameter pattern search as a function of one parameter, but since multiple parameters were varied in the pattern search, the graphs represent the hyperdimensional projection of *ER* values along the J_1 variable and along the t_{34} variable. A noisy minimum of *ER* values is visible in both cases.

Determining the precise location of the minimum. The error function values sampled near the minimum were first fit with a multidimensional parabolic function:

$$ER^{fit}(\alpha_i) = ER^{min} + \sum_i C_i\left(\alpha_i - \alpha_i^{min}\right)^2 \qquad \text{(SE16)}$$

where $ER^{fit}(\alpha_i)$ is the fitting function that depends on the freezing parameters α_i, ER^{min} is the minimum value of the fitting function and C_i are numeric coefficients. α_i^{min} are the best freezing parameter values, which lead to the lowest value of $ER^{fit}(\alpha_i)$. A parabolic function was chosen because near a minimum, all functions have a quadratic form in the leading approximation of the Taylor expansion. The Taylor expansion also includes cross terms that depend on the product of two different parameters, but we did not include them because the squared terms were sufficient for a good quality of the fit.

The best values of the freezing parameters were typically refined further, by performing single-parameter (or one-dimensional, 1D) scans from the minimum of the multidimensional parabola, followed by fitting the scan data with 1D parabolic functions.

Unlike the simulated probabilities, $ER^{fit}(\alpha_i)$ and the parabolic fit functions are analytic, and the fitting were performed using gradient-based optimization algorithms. The results of fitting are illustrated in Extended Data Fig. 4(d,e). The 1D scans and two corresponding parabolic fits are located at the lower outline of the plotted points, which is to be expected for a good fit because the points sampled with the pattern search are projected from an approximately parabolic hypersurface.

We found that good multidimensional parabolic fits require of the order of one thousand sampled points that are relatively close to the minimum and are distributed symmetrically around it. These sets of sampled points were acquired by starting the pattern search close to the minimum of *ER*.

The determination of the freezing parameters required of the order of one billion single-droplet simulations. The three fitting steps (see section E.2) used experimental data from approximately 70000 drops because the two-exposure image data were used twice. Each *ER* calculation used ten times the number of experimental drops, and of the order of 1000 *ER* calculations were needed, which leads to 7×10^8 single-drop simulations. The total number of single-drop simulations needed is somewhat larger due to the 1D scans, and because finding an initial starting point for the pattern search required additional simulations.

E.5 Estimates of the statistical uncertainty of the freezing parameters

Due to the stochasticity of the freezing process, the measured probabilities of freezing stages and of splitting have their own statistical noise. This noise leads to a statistical uncertainty of the freezing parameters, which is larger than the precision with which the parameters can be determined from fitting.

We evaluated the statistical uncertainty of the freezing parameters from the statistical uncertainty of the error function value *ER* that is caused by the experimental noise. We evaluated the statistical uncertainty of *ER* as the standard deviation of *ER* from multiple-drop simulations conducted with the same number of drops as in the experiment. (In contrast, the parameter determination procedure used simulations with ten times the number of drops in the experiment, to ensure that the simulation noise was smaller than the experimental noise.)

We evaluated the standard deviation of *ER* by running approximately 100 multiple-drop simulations. This procedure was performed for each of the three fitting steps (see section E.2) since the calculation of *ER* used different experimental measurements in each case. The standard deviations of *ER* for steps one to three were 8.8, 5.2, and 2.0, respectively.

The range of uncertainty for a given freezing parameter was calculated as the negative and positive changes in the parameter values, relative to the value at the minimum, that led to an increase in the *ER* by one standard deviation of *ER*, based on the final fitting functions used to determine the minimum of *ER* (see section E.4). The uncertainty ranges for all freezing parameters are displayed in Extended Data Table 1.

F. Heterogeneous ice nucleation experiments

F.1 Dynamics of freezing at the droplet scale

Images of droplets freezing after heterogeneous nucleation are shown in Extended Data Fig. 8(c). While the stages of freezing are the same as after homogeneous nucleation, their properties were different because of the different nucleation temperatures (see Section F.2), and because of different temperature gradients. For pure water drops the temperature difference between surface and center was ~1.5 K at nucleation, which has a small impact on thermal properties inside the drop except for the nucleation rate. In contrast, according to the evaporative cooling model, the temperature difference is ~4 K for drops with ATD and ~20 K for drops with AgI. In the latter case, when the regions near the surface first became cold enough to nucleate ice, the center of the drop was ~10 K above the melting temperature.

For drops doped with AgI, the freezing stage properties were most different from the ones after homogeneous nucleation. (i) During dendritic growth the ice features were often observed near the periphery of the drop, as expected since the center of the drop was too warm to freeze. The surface of the drop likely solidified while the center of the drop was still liquid, in part because ice grew faster in the colder liquid near the surface, and in part because multiple ice nucleation events likely occurred due to the high concentration and high ice nucleation efficiency of AgI particles. (ii) The spicules were larger, and most frequently only one spicule was observed. This can be explained by the smaller fraction of ice after dendritic freezing, which leads to a higher liquid fraction and a better connectivity of the liquid regions[14], allowing the pressure buildup to be relieved through the growth of a single large spicule. The larger size, and thus volume, of the spicules is explained by the larger liquid fraction trapped by the ice shell. (iii) The fraction of drops whose fragments remained joined after cracking (stage 6) was substantially larger than after homogeneous nucleation. For pure water drops our model predicts that drops with joined fragments are one order of magnitude less likely than split drops, while for drops with AgI joined fragments were observed approximately as frequently as separated fragments. Such joined drops were also reported in other experiments that investigated drop shattering at small and moderate supercooling[6,7,16,23]. The fragments remain joined because the liquid still present inside the drop holds the fragments together via surface tension[6].

The images of drops containing ATD particles showed stage properties that ranged from the ones observed with AgI to the ones observed for pure water. The ATD particles were less efficient nucleators than AgI particles, and nucleated ice over a wide temperature range between the nucleation temperatures of drops with AgI and with pure water.

We could not develop detailed freezing models for drops with ice ice-nucleating particles because we did not have low-magnification image data to measure the splitting probability. The development of freezing models after heterogeneous nucleation should be feasible because the stages could be detected, and their probabilities evolved with the time of flight. However, some stages must be modeled differently. For example, in drops with AgI, dendritic freezing should lead to an inhomogeneous ice fraction and the growth of spicules might be better modeled as a continuous process rather than a two-step process.

The drops with ice-nucleating particles had large thermal gradients in the liquid phase (up to 1.4 K/μm for drops with AgI with the surface at 262.5 K), but they were only a fraction of the gradient at the dendritic freezing front, and should not have a substantial effect on the formation of the crystal. The thermal gradient at the freezing front can be estimated from a heat flux balance as $(\mathrm{d}T/\mathrm{d}x)_{\mathrm{dendritic}} = f_{FZ}\, v_G\, \mathrm{L}\, \rho$, where f_{FZ} is the frozen fraction, v_G the ice growth speed, L the latent heat of melting, and ρ is the density of the liquid. This formula is consistent with experimental data[10] and predicts a gradient of 2.9 K/μm for drops with AgI, two times larger than the cooling gradient. This ratio increases with supercooling is of the order of hundreds for pure water drops.

F.2 Estimation of nucleation temperatures and time delays

The estimated nucleation temperatures and time elapsed from nucleation are given in Extended Data Fig. 8(a-b) for the heterogeneous nucleation experiments. We used different methods to estimate the nucleation temperatures and time delays for drops with AgI and ATD particles, because they had very different ice nucleation efficiencies. The drops with AgI nucleated ice very efficiently and had the largest temperature differentials inside the drop, and we approximated that the nucleation occurred in the shell at the surface. In contrast, nucleation in drops with ATD was observed over a wide range of temperatures (wider than the temperature differentials), and we approximated that the nucleation could occur anywhere inside the drop.

Stage 2 of freezing. Due to the continuous rapid cooling, the nucleation temperatures must be calculated as the relevant temperature in a liquid drop at the time of nucleation. The time delay between nucleation and probing by the XFEL must be evaluated first. For the dendritic phase of freezing (stage 2), we deduced the delays based on the size of the dendritic crystals and their growth speed. We defined the shortest possible time delay for both AgI and ATD as the time needed for a crystal to grow to the minimum observable crystal size from the freezing model, d_{Xmin}. In drops with ATD, we defined the longest possible time delay as the time in which a crystal grew from the drop surface to the limiting location where stage 2 can be identified (see Extended Data Fig. 3(c)), $R_{drop} + R_{vis} - d_{Xmin}$. In drops with AgI the drop center was too warm to freeze, and we defined the longest possible time delay as the time in which the crystals size became equal to the drop radius, since this was approximately the size of the longest straight dendritic crystal segments observed in images.

The time in which crystals grew to a specific size was estimated using the temperature-dependent ice growth velocity, $v_{grow}(T)$, given by Amaya *et al.*[42], at the relevant drop temperature. For drops with AgI we used the temperature of the outer shell (approximately equal to the surface temperature), and for drops with ATD we used the average temperature of the drop.

The range of nucleation temperatures for drops with AgI was calculated as the surface temperatures at the times of flight corresponding to the limits of the time delay range. For drops with ATD the lower nucleation temperature was given as the surface temperature corresponding to the shortest delay, and the higher nucleation temperature as the center temperature corresponding to the longest time delay.

Stage 5 of freezing. For drops with AgI, the heterogeneous nucleation rate per drop was sufficiently high that most drops observed at a given time of flight were in the same stage of freezing, which indicates that most of the drops nucleated ice in the same temperature range as the one found for stage 2. Therefore, we estimated the time delay for stage 5 by adding the additional time of flight to the delay for stage 2. Since the diffraction data for stage 5 was collected at two different times of flight, the lower limit of time delays was calculated as the lower limit of time delays for stage 2 plus the shorter additional time of flight, and the higher limit by adding the higher limit for stage 2 to the longer additional time of flight.

For drops with ATD, the time delays after nucleation were calculated using the time delays over which stage 5 occurred, according to an adjusted freezing model. The lower limit of the time delays was estimated as $\Delta t^*_2 + t^*_{34} + t^*_{45}$ and the upper limit as $\Delta t^*_2 + t^*_{34} + t^*_{45} + 0.5(t^*_{56mean} + t^*_{57mean})$, where the star superscript indicates that these variables apply to the drops with ATD, rather than the pure water drops in the freezing model. The duration of dendritic freezing was calculated as $\Delta t^*_2 = 1.75R_{drop}/v_{grow}(T)$ because nucleation was assumed to occur equally probably inside the drop volume, which leads to an average nucleation radius[36] $R_N = 0.75R_{drop}$. The durations of the latter stages were estimated by scaling them linearly to the values in the model, by a factor equal to the ratio of solidification times. The delay limits were first evaluated over a range of temperatures near the expected nucleation temperature. Then, the correct value of a given delay limit was chosen such that the delay and its associated temperature were consistent with the cooling curve of the liquid drop. The lower limit of nucleation temperatures was estimated as the surface temperature corresponding to the shortest delay, and the higher limit as the center temperature corresponding to the longest time delay.

G. Processing of X-ray scattering data

G.1 Data sets and data selection

For the determination of X-ray scattering from freezing drops, we used only single-drop diffraction patterns which had a simultaneous doubly exposed optical image with an identifiable freezing stage. For the X-ray scattering data, drops with optically identifiable stages were included even if they were outside the ±10 μm depth of field used for the measurement of stage probabilities, because for X-ray scattering the physically relevant condition is the time elapsed after ice nucleation, which is estimated based on the freezing stage. This enabled the collection of additional X-ray scattering data from drops with spicules and split fragments, which could be identified outside the ±10 μm depth of field. The data used for X-ray scattering from pure water drops also included additional times of flight from 7.06 ms to 7.85 ms, and contained diffraction data from 17260 drops and drop fragments. At the longest times of flight, the best hit rate was obtained by probing the droplet stream off-center, which also improved the collection of data from split fragments, which spread rapidly from the center of the droplet stream.

The X-ray scattering data from pure water drops was collected using three different settings of the pre-sample attenuator: 0.9% transmission (739 drops and drop fragments, approximately 0.01 mJ average pulse energy at the sample), 11% transmission (13524 drops and fragments, approximately 0.13 mJ at the sample) and 33% transmission (2997 drops and fragments, approximately 0.42 mJ at the sample). These transmission values were set on a trial-and-error basis to provide the largest raw X-ray scattering signals on the detector while avoiding the degradation of the detector pixels due to very intense Bragg peaks. At the largest times of flight (7.34–7.95 ms) the drops were almost completely frozen (stages 4 to 7) and diffracted strongly, thus a 0.9% transmission was used. The crystal diffraction data recorded at 0.9% transmission was not affected by X-ray detector saturation. The 11% transmission data included the shortest times of flight (6.44–7.06 ms), where all freezing stages were observed but most drops were in the early stages of freezing (stages 1 to 3). The crystal diffraction data was affected by detector saturation, but the 11% transmission data was most useful for determining the properties of the ice crystals due to a large number of shots. The data 33% transmission was recorded for only a few runs (6.74–6.91 ms) until it was observed that the high intensity of the diffraction peaks led to a high risk of pixel degradation due to very intense Bragg peaks, and included drops in all stages. Due to the larger pulse energy, the 33% data had the best X-ray scattering data from the liquid phase. The liquid scattering pattern from stage 1 drops had the same shape for the 11% and the 33% transmission data, showing that the liquid scattering data recorded 33% transmission was not affected by detector saturation.

The X-ray scattering data from drops with ice-nucleating particles was collected at 10% transmission for stage 2 drops, and at 2% (ATD) or 3% (AgI) transmission for stage 5 drops. The number of data points and the average pulse energies at the drops for these data sets are given in Extended Data Fig. 8 and its caption.

The XFEL pulses occasionally intercepted droplets that were outside the lateral field of view of the optical images. Such drops were at different distances from the detector than the main data, and due to the geometry of diffraction they led to the apparition of Bragg peaks away from the expected diffraction angles for ice, or the scattering image from the liquid had a different size of the attenuator shadow. These events were detected based on their anomalous crystal diffraction or liquid scattering profiles, and were removed from the data.

G.2 Detector geometry refinement

The 2D X-ray detector used in this study was a 32-tile, 4-quadrant Cornell-SLAC Pixel Array Detector[33] (CSPAD). The four quadrants are arranged to make an opening for the XFEL beam and are movable to prevent exposure to spurious small-angle scattering from upstream beamline components. The modular construction of the detector introduced an uncertainty in the location of individual pixels relative to the sample. To determine the location of the detector pixels with high accuracy, it was necessary to refine the pixel coordinates, through translations of the individual detector tiles, by requiring that the diffraction peaks from a reference sample are observed as close as possible to the expected diffraction angles[39]. The reference data we used were the virtual powder ice diffraction rings collected from droplets in stages 3 to 5 at short times of flight (6.44–6.76 ms), because this choice provided relatively narrow rings as they were least broadened by the spreading of the droplet stream.

Reference diffraction angles and photon momentum transfers. The diffraction angles and the corresponding photon momentum transfer for hexagonal and cubic ice were calculated using an X-ray wavelength of 1.3051 Å and the lattice constants of hexagonal and cubic ice at 273 K. For hexagonal ice we used the lattice constants a = 4.5226 Å and c = 7.3651 Å at 273 K, which were calculated using the temperature-dependent parametrization given by Röttger *et al.*[75]. For cubic ice we used a lattice constant a = 6.3955 Å at 273 K, which we derived by scaling Dowell and Rinfret's 88 K data[76] by the cube root of the volumetric thermal expansion ratio predicted by Röttger *et al.*'s parametrization for hexagonal ice.

The refinement of the pixel coordinates. The pixel positions were refined by adjustments to the position of individual CSPAD tiles relative to the interaction point. The adjustments consisted of translations in three dimensions and were derived in two steps. The first step involved minimizing an alignment function that quantified the overlap of experimental Bragg peaks with their expected locations, and provided translation corrections in the plane of the detector, for each of the detector quadrants. The second step involved manual adjustments for each of the individual tiles to ensure the overlap of the experimental virtual powder diffraction pattern rings with the expected locations of the diffraction rings of hexagonal ice.

The alignment function was built by multiplying the square of the pixel intensity with the corrected radial distance of a pixel to the expected diffraction ring (in the plane of the detector). This alignment function is minimized when the experimental peaks align with their expected locations. Translations of the tiles along the XFEL beam were treated by scaling the radius of the expected diffraction ring. The function was calculated only over a set of pixels located near the expected diffraction ring, to avoid an erroneous alignment of the tile with a different ring. The value of the function was then minimized using the fmincon function in MATLAB.

In principle, the translation corrections for each detector tile can be determined by minimizing the alignment function, but in our case, this led to poorly constrained shifts due to the substantial broadening of the Bragg peaks. Instead, we minimized the alignment function for a whole quadrant (containing 8 tiles), and we repeated this procedure for sample-detector distances ranging from 69.5 to 72.1 mm in 0.2 mm steps, obtaining for each quadrant two orthogonal position corrections in the plane of the detector. The multiple minimizations were necessary because the location of the direct beam derived from minimization changed with the sample-detector distance.

For each trial sample-detector distance, a composite image of the diffraction image was assembled using the corrected pixel positions, and the expected rings from hexagonal ice at 273 K were overlaid on it. Then, for each of the tiles, the sample-detector distance and the corresponding corrections in the plane of the detector were determined based on the best overlap of the experimental and predicted rings. For a few of the tiles, it was also necessary to add a second-order translation correction in the plane of the detector.

The geometry optimization was performed using data from pure water drops. We verified that the refinement of pixel coordinates remained valid for the measurements on drops with ice nucleating particles.

We note that our detector geometry optimization procedure leads to diffraction peaks that are perfectly aligned with the diffraction peaks of hexagonal ice at 273 K, and this may obscure a difference between the density of rapidly solidified ice in our experiment and that of perfect hexagonal ice. Despite this limitation, the geometry optimization was necessary for performing the Williamson-Hall strain analysis, because the default detector geometry led to diffraction profiles with peak widths significantly larger than the width that is visible in accumulated diffraction images such as the one shown in Fig. 4(a) in the main text.

G.3 Pixel signal corrections

Pedestal subtraction and common mode noise correction. The detector data was processed[38] starting with the raw intensity readout from the detector, which includes a background signal ("pedestal"). The pedestal is the raw detector output in the absence of any incoming photons, and was measured in a dedicated "dark" run recorded with XFEL shutter closed, halfway through the data acquisition. The first step in the data processing was the subtraction of the pedestal from the raw detector data.

The CSPAD detector exhibits a "common mode" noise[77], where the signal from a given pixel also depends on the X-ray intensity arriving at nearby pixels. The CSPAD tiles contain unbonded pixels that do not produce signal in response to X-rays, but produce an electronic signal that is an approximation of the common noise level. To correct for common noise for measurements with pure water drops, we calculated the average signal from the unbonded pixels (after pedestal subtraction) and subtracted it from each active pixel. This procedure was performed independently over each half of the detector tiles, to account for the variation of the common mode noise across the detector. We note that the common-mode correction we used is different from the default correction used by the LCLS data analysis environment. The common mode noise was very large in the detector tiles containing the edge of the attenuator's shadow, and the unbonded pixels algorithm was superior to the default one.

The measurements for drops with AgI and ATD required a different treatment of the common mode noise. This data was collected two days later than the data for pure water drops, and the noise of the X-ray detector was different. (This could indicate a degradation of the CSPAD detector during the beamtime, due to exposing it to high-intensity diffraction from ice.) Applying the common mode correction to our data led to a discontinuous liquid scattering profile at the edge of the attenuator, and to unphysically high crystal peaks at 2.7–3.4 Å. Therefore, for drops with AgI and ATD we did not apply a correction for the common mode noise; without this correction, the liquid scattering patterns had the best continuity at the edge of the attenuator.

Attenuator correction and detector masking. The attenuation of the X-ray passing through the post-sample attenuator varied substantially with the diffraction angle, due to the increase of X-ray path at larger angles combined with the exponential dependence of the attenuation with the X-ray path length. To measure the attenuation factor, a liquid jet was established at the interaction region by lowering the nozzle and switching off the drop generation. Two runs were recorded with the attenuator in place and with the attenuator removed. The attenuation factor was obtained by dividing the average intensities from the two runs after background subtraction and common mode correction. To reduce the impact of shot noise, the average intensity images were smoothed before division, using a 3-by-3 pixel averaging kernel.

Regions of the detector tiles that were partially shadowed by the attenuator had anomalous attenuation factors, caused by the common mode noise. These regions affected by large common noise errors were masked from further data processing. The mask can be seen in Extended Data Fig. 6(a-c), where parts of the tiles are missing from the displayed images. Besides masking pixels affected by the common mode noise, the mask also omitted: (i) unbonded and tile-boundary pixels along with their neighbors; (ii) pixels that displayed anomalously high or low signal levels, or large standard deviations, in the dark run; (iii) damaged pixels, which displayed anomalous signal levels when exposed to X rays; (iv) regions near the edge of the attenuator, where the attenuation factor is prone to errors due to variations in the distance of individual drops from the detector; and (v) regions masked by other objects, such as the holder of the attenuator.

Polarization correction. The X-ray laser pulses used in the experiment were linearly polarized in the horizontal direction, leading to an angular dependence of the intensity of the detector, with the maximum scattered intensity along the vertical axis. We used the procedure given by Sellberg *et al.*[2] to correct this effect by dividing the data by a polarization correction factor, $P_{corr}(\theta_p, \varphi_p)$, where $P_{corr} \leq 1$. This amplified the signal from pixels away from the vertical direction and made the scattering signal azimuthally symmetric.

G.4 Separation of X-ray crystal diffraction and X-ray liquid scattering

G.4.1 Calculation of total scattering profiles

Using the optimized pixel locations and the 109.92-μm pixel size, the following values were calculated for each pixel: the diffraction angle $2\theta_p$, the azimuthal angle φ_p, the photon momentum transfer $Q_p = 4\pi \sin(\theta_p)/\lambda$ where λ is the X-ray wavelength, the solid angle covered by the pixel Ω_p, and the polarization correction factor[2] (which is a function of θ_p and φ_p).

The radial scattering points were calculated for 1000 equally sized momentum transfer bins covering the range from 0 to 5 $Å^{-1}$. All the pixels with valid data (*i.e.* pixels that were not masked) were grouped in sets to their corresponding *Q*-bins. Some of the *Q*-bin pixel sets, for example those at the lowest *Q* values, which map to the central opening of the detector, did not include any pixels. To avoid noisy results and to improve the separation of scattering from crystals and liquid, the radial scattering patterns were calculated only if the *Q*-bin set contained at least 15 valid pixels.

The *Q*-bin scattering intensity for a single diffraction image was calculated in analog-to-digital detector units (ADU) per solid angle, or ADU/sr. At the 9.5 keV photon energy used in the experiment, the CSPAD outputs approximately 45 ADUs at normal photon incidence[78]. The average scattering in a *Q*-bin, in ADU/sr units, was calculated according to the formula:

$$I(Q_b) = \sum_{bin\,pixels} I_p / \sum_{bin\,pixels} \Omega_p \qquad \text{(SE17)}$$

where $I(Q_b)$ is the scattering intensity measured in the *Q*-bin, Q_b is the center of the bin, and I_p is the scattered photon signal in detector units. If a *Q*-bin contains less than 15 pixels, $I(Q_b)$ was assigned either a zero value or a special numerical value (not-a-number) depending on how $I(Q_b)$ was used in the next steps of the data analysis.

G.4.2 Separation of crystal and liquid scattering profiles

The scattering signal from a freezing drop contained both a diffuse signal from the liquid, and localized high-intensity signals from the crystals, which can be either Bragg peaks or crystal truncation rods. Separation of these components was useful for understanding the structural evolution of both the crystal and the liquid. XFEL diffraction images were well suited for separation because crystal diffraction could be identified not only based on pixel intensity but also based on the grouping of pixels.

Separation of scattering components from single detector images. The separation of the X-ray scattering into crystal and liquid components was performed by assigning individual pixel data to either crystal diffraction or liquid scattering. The assignment of pixel data was based on the pixel intensities and their spatial grouping in the detector images. The criteria for identifying crystal diffraction in a single pixel were that (i) the pixel intensity was significantly larger than the liquid scattering intensity in the image being analyzed, and that (ii) the pixel had at least one adjacent pixel that also had a significantly larger intensity than the liquid.

The intensity criterion for the crystal diffraction pixels varies both with the diffraction angle $2\theta_p$ (due to the varying intensity of the liquid scattering) and with the azimuthal angle φ_p (due to the polarization of the X rays). Other analysis challenges were the photon statistics, the spread of the signal from a photon across multiple pixels, and the variation of the detector signal per photon as the diffraction angle and the X-ray path inside the detector increases. These challenges were addressed using an intensity criterion that considers the statistics of X-ray photon detection.

To determine the intensity threshold for crystal diffraction in a specific pixel, the average liquid scattering intensity at the pixel's diffraction angle was estimated first. This value was calculated by averaging intensities from pixels in the same Q-bin as the specific pixel, and having intensities in the 15%–98% percentile among all pixels in the bin. These intensities were polarization-corrected but not attenuation-corrected. The high percentile cutoff was imposed to exclude the relatively rare pixels exposed to high-intensity crystal diffraction, which can lead to an incorrectly high average for the liquid. The low percentile cutoff was imposed empirically after finding that, after the pedestal and the common mode corrections were applied, the lowest intensity pixels in a Q-bin could have negative intensity values that affected later processing steps.

Using the liquid X-ray scattering intensity at the pixel's diffraction angle, the average number of photons scattered by the liquid at the pixel's specific location was calculated using:

$$N_L = \frac{I_L(\theta_p) P_{corr}(\theta_p, \varphi_p)}{\mathrm{ADU_{phot}}\, D_{corr}(\theta_p, \varphi_p)} \qquad \text{(SE18)}$$

where $I_L(\theta_p)$ is the average liquid scattering intensity at the diffraction angle $2\theta_p$, $P_{corr}(\theta_p, \varphi_p)$ is the polarization correction factor at the diffraction angle $2\theta_p$ and the azimuthal angle φ_p, $\mathrm{ADU_{phot}} = 45$ is the detector signal for a 9.5 keV photon at normal incidence, and $D_{corr}(\theta_p, \varphi_p)$ is an approximate geometrical correction of $\mathrm{ADU_{phot}}$. $D_{corr}(\theta_p, \varphi_p)$ is equal to the ratio of X-ray attenuation in the pixel along the mean photon path length in the volume of the pixel, to the same attenuation for a photon at normal incidence. The multiplication of the liquid intensity with the polarization correction factor ensured that the reduction of scattered intensity due to polarization was accounted for.

The intensity threshold for crystal diffraction was defined as the average liquid intensity plus a multiple of the standard deviation of the liquid intensity. The standard deviation of N_L is equal to $(N_L)^{1/2}$ since the detected photons have Poisson statistics, and the standard deviation of the intensity is equal to the standard deviation of the photon number multiplied by the corrected detector signal per photon, $\mathrm{ADU_{phot}} D_{corr}(\theta_p, \varphi_p)$. The intensity threshold for crystal diffraction, $I_{XT,p}$, was therefore defined as:

$$I_{XT,p} = \mathrm{ADU_{phot}}\, D_{corr}(\theta_p, \varphi_p) \max\{(N_L + n_\sigma \sqrt{N_L}), N_{min}\} \qquad \text{(SE19)}$$

where n_σ is the number of standard deviations and N_{min} the minimum photon number. A setting of $n_\sigma = 4.5$ was sufficient for a good separation of the crystal scattering. The quantity maximized in Eq. (SE19) is the threshold number of photons arriving at a pixel, which physically cannot be smaller than 1, and for pure water drops we used $N_{min} = 1$. For drops with AgI and ATD we found empirically that the best separation occurred when N_{min} was set to 1.5 instead of 1, which may be due to the larger detector noise. The pixels were initially separated based on the intensity threshold and stored in two X-ray detector images that contained the separated data for the pixels that recorded crystal scattering, and for the pixels that recorded liquid scattering. The separated images contained pixels that did not contain intensity information (for example, in the crystal image, the pixels exposed only to liquid scattering did not contain data); such pixels were assigned a special numerical value (not-a-number).

The second criterion for separating the scattering components is that pixels with crystal scattering must have at least one adjacent pixel with crystal scattering. This was applied next. For each pixel in the crystal scattering image, the number of adjacent pixels with crystal data was calculated. If no adjacent pixels were found, that pixel was copied to the liquid image and then erased from the crystal image.

Calculation of total, crystal, and liquid scattering profiles from one detector image. From one corrected diffraction image, the pixel separation procedure generated two partial images for crystal diffraction and liquid scattering. The Q-bin scattering intensity calculation described in Section F.4.1 was modified to calculate the separated scattering intensities. The liquid scattering intensity per solid angle, $I_L(Q_b)$, was normalized by the total solid angle of the liquid pixels in the bin. This procedure leads to the same intensity as the one in a liquid diffraction image without crystal scattering:

$$I_L(Q_b) = \sum_{bin\ pixels,liquid} I_p / \sum_{bin\ pixels,liquid} \Omega_p \qquad \text{(SE20)}$$

The crystal scattering intensity per solid angle, $I_X(Q_b)$, was calculated by correcting first the pixel signal by subtracting the Q-bin-averaged liquid scattering from the signal in the crystal pixels, followed by the normalization of the corrected crystal signal by the solid angle of all pixels with crystal diffraction in the Q-bin. This procedure leads to the same intensity as in a crystal powder diffraction ring without liquid scattering:

$$I_X(Q_b) = \left(\sum_{bin\ pixels,crystal} I_p - I_L(Q_b) \sum_{bin\ pixels,crystal} \Omega_p\right) / \sum_{bin\ pixels} \Omega_p \qquad \text{(SE21)}$$

Calculation of scattering profiles from image sets. The crystal and liquid scattering intensities from a set of diffraction images were calculated by averaging in each Q-bin the respective intensities derived from single images. These scattering profiles thus represent the average liquid and crystal scattering from single drop. An example of scattering profiles with absolute scattering intensities is shown in Extended Data Fig. 6(d).

Performance and limitations of the separation procedure. Extended Data Fig. 6(a-c) shows the total, crystal, and liquid scattering images and scattering profiles accumulated from 3595 stage 3 drops from the data with 11% X-ray transmission. The crystal image shows only Bragg peaks and crystal truncation rods, while the liquid image has a smooth intensity variation. The scattering profile of the liquid has only small distortions at the location of Bragg peaks. The crystal profile displays a significant signal between the Bragg peaks, but this signal is due to the crystal truncation rods and not due to liquid scattering. The crystal truncation rods are visible in the crystal diffraction image shown in Extended Data Fig. 6(b).

For the data at 11% and 33% transmission, the separation procedure left residual crystal peaks in the liquid profile with a height of 0.008 of the height of the peaks in the crystal profile, as well as broader distortions caused by the incomplete separation of the signal from the wings of the Bragg peaks and from crystal truncation rods. The residual peaks in the 11% transmission liquid profile are barely visible in Extended Data Fig. 6(d). In the 0.9% transmission data, the heights of the residual peaks in the liquid profiles were approximately 0.05 of the height of the peaks in the crystal. We empirically corrected for this incomplete separation by subtracting 0.008 (11% and 33% transmission) or 0.05 (0.9% transmission) of the crystal profile from the liquid profile, and by multiplying the crystal profile by 1.008 (11% and 33% transmission) or 1.05 (0.9% transmission). The scattering profiles displayed in the main text Fig. 3 and Extended Data Fig. 7, as well as the crystal data used for the Williamson-Hall strain analysis (main text Fig. 4) were empirically corrected for the incomplete separation.

The reduced performance of the separation procedure for the 0.9% transmission data is due to a physical limitation of the separation procedure when the scattered intensity is very small. In this case, the average scattering was below one photon per pixel, and a significant portion of the pixels recording photons are surrounded by pixels not recording any photons. In our separation procedure such pixels are assigned to liquid scattering, but as the overall intensity on the detector decreases there is an increasing probability that the pixels recorded weak crystal diffraction. Although significant, the imperfect separation of 0.9% transmission data had a small impact on the subsequent data analysis. Without the empirical correction of the separation, it would lead to an approximately 5% reduction of the peak heights, which in the Williamson-Hall analysis would have decreased the grain size and increased the inhomogeneous strain by 5%, less than the uncertainty of the fit shown in main text Fig. 4(b).

G.4.3 Generation of accumulated crystal and liquid scattering images

We generated accumulated X-ray detector images of liquid scattering and crystal diffraction by assembling X-ray scattering data characterized by the same XFEL transmission and the same stage of freezing. Since single scattering images typically display only a few Bragg peaks, the combined images, which have numerous Bragg peaks, were used to illustrate their typical shapes and location as shown in the main text Fig. 4(a). The combined images were also used as an additional test of the separation of scattering into crystal and liquid components (Extended Data Fig. 6(a-c)).

The liquid scattering images (see Extended Data Fig. 6(c)) were assembled as a weighted sum of scattering images from single drops. The weight of a single drop image was calculated as average of the intensity in all available pixels (i.e., the pixels found to be exposed to liquid scattering only). This weight was then written in a normalization matrix with the same dimension as the diffraction image. The weight value was written only at the location of available pixels; not-a-number values were written at the location of pixels missing from the liquid image because they had been exposed to crystal diffraction. The weighting reduced intensity variations in accumulated image, in regions where single liquid images had missing information due to the presence of Bragg peaks.

In the crystal diffraction images from single drops, the intensity of the pixels not exposed to crystal diffraction was first set to zero. The accumulated crystal diffraction image (see Extended Data Fig. 6(b)) was then obtained by summing diffraction images from single drops. The total diffraction image was assembled by summing diffraction images from single drops. To bring the intensity to comparable values for all images (total, crystal, and liquid), the total and the crystal scattering images were further divided by the sum of the weights of the liquid images.

To help visualize diffraction peaks with very different intensities, the intensity display scale of the images in the main text Fig. 4(a), Extended Data Fig. 6(a-c), and Extended Data Fig. 9 is nonlinear. The detector images in Extended Data Fig. 6(a-c) are displayed on a logarithmic scale, and the images in Extended Data Fig. 9 are displayed on a power-law scale with an exponent of 0.33. The scattering intensity data for the main text Fig. 4(a) was (i) divided by molecular form factor of water, (ii) multiplied by the photon momentum transfer Q, (iii) multiplied by the radial position of the detector pixels, (iv) divided by the cosine of the diffraction angle 2θ, and (v) the part of the image behind the post-shadow attenuator was multiplied by a factor proportional to the angle-dependent attenuation factor.

G.5 Williamson-Hall analysis

The Williamson-Hall analysis is shown in the main text Fig. 4(b). The line breadth was calculated as the integral breadth of the peak[26], *i.e.*, as the peak area divided by the peak height. The peak area was calculated by numeric integration of the points from that peak that had a height of at least of ~0.1 of the maximum intensity.

The integral line breadth does not depend on X-ray intensity errors that are proportional to the signal and have a negligible dependence on Q across the peak. Therefore, although the peaks between 2.7–3.4 $Å^{-1}$ were affected by the detector noise, this has a small impact on the line breadth since the noise level had a weak dependence on Q across a single peak. The incomplete separation of crystal diffraction from liquid scattering led to residual peaks in the liquid profiles that had approximately the same width as the one from the crystal profiles. Due to the similar width of the residual peaks, the incomplete separation reduced both the peak height and the peak area, and the relative error of the integral breadth was smaller than the relative error of the peak height.

The integral line breadths can be affected by detector saturation. Saturation reduces selectively the highest intensities across the peak, flattening the top of the peak and causing an increase of the measured breadth. To avoid this problem, the Williamson-Hall analysis was reported only for the 0.9% transmission data set, which had the lowest diffraction intensities at the pixel level. Another source of error is the partial sampling of the diffraction reflections in the reciprocal space, which leads to statistical fluctuations of the peak shape and height. In our data, the shapes or heights of the hexagonal (200), (201) and (300) peaks had the largest fluctuations, as seen in Extended Data Figs. 7 and 8. The number of pixels where these peaks could be recorded were relatively small, with regions that overlapped with the (200) and (201) rings being masked to mitigate the common mode noise, and the (300) ring being located near the corner of the detector. These three peaks were not included in the Williamson-Hall analysis.

The uncertainties of the crystal size and of the inhomogeneous strain (see Fig. 4(b)) were calculated from the standard deviation of the linear fit coefficients. We evaluated the impact of sampling by calculating the crystal size and strain for a subset of the data (303 drops and fragments, instead of 739). For this subset, $d_{undersampled} = 91\pm25$ nm and $\varepsilon_{undersampled} = 0.0071\pm0.0006$ µm, which is consistent with the analysis of the full data set.

H. References

(References 1–54 are from the main text; supplementary references start at #55.)

1 Angell, C. A., Oguni, M. & Sichina, W. J. Heat Capacity of Water at Extremes of Supercooling and Superheating. *J. Phys. Chem.* **86**, 998-1002 (1982).

2 Sellberg, J. A. *et al.* Ultrafast X-ray probing of water structure below the homogeneous ice nucleation temperature. *Nature* **510**, 381-384 (2014).

3 Stöckel, P., Weidinger, I. M., Baumgartel, H. & Leisner, T. Rates of Homogeneous Ice Nucleation in Levitated H_2O and D_2O Droplets. *J. Phys. Chem. A* **109**, 2540-2546 (2005).

4 Stan, C. A. *et al.* A microfluidic apparatus for the study of ice nucleation in supercooled water drops. *Lab Chip* **9**, 2293-2305 (2009).

5 Hagen, D. E., Anderson, R. J. & Kassner, J. L. Homogeneous Condensation–Freezing Nucleation Rate Measurements for Small Water Droplets in an Expansion Cloud Chamber. *J. Atmos. Sci.* **38**, 1236-1243 (1981).

6 Wildeman, S., Sterl, S., Sun, C. & Lohse, D. Fast Dynamics of Water Droplets Freezing from the Outside In. *Phys. Rev. Lett.* **118**, 084101 (2017).

7 Lauber, A., Kiselev, A., Pander, T., Handmann, P. & Leisner, T. Secondary Ice Formation during Freezing of Levitated Droplets. *J. Atmos. Sci.* **75**, 2815-2826 (2018).

8 Murray, B. J., Knopf, D. A. & Bertram, A. K. The formation of cubic ice under conditions relevant to Earth's atmosphere. *Nature* **434**, 202-205 (2005).

9 Malkin, T. L., Murray, B. J., Brukhno, A. V., Anwar, J. & Salzmann, C. G. Structure of ice crystallized from supercooled water. *Proc. Natl. Acad. Sci. USA* **109**, 1041-1045 (2012).

10 Buttersack, T. & Bauerecker, S. Critical Radius of Supercooled Water Droplets: On the Transition toward Dendritic Freezing. *J. Phys. Chem. B* **120**, 504-512 (2016).

11 Esmaeildoost, N. *et al.* Heterogeneous Ice Growth in Micron-Sized Water Droplets Due to Spontaneous Freezing. *Crystals* **12**, 65 (2022).

12 Pruppacher, H. R. & Klett, J. D. *Microphysics of Clouds and Precipitation*. (Springer Dordrecht, 2010).

13 Murray, B. J., Carslaw, K. S. & Field, P. R. Opinion: Cloud-phase climate feedback and the importance of ice-nucleating particles. *Atmos. Chem. Phys.* **21**, 665-679 (2021).

14 Korolev, A. & Leisner, T. Review of experimental studies of secondary ice production. *Atmos. Chem. Phys.* **20**, 11767-11797 (2020).

15 Field, P. *et al.* Secondary ice production: Current state of the science and recommendations for the future. *Meteor. Mon.* **58**, 7.1-7.20 (2017).

16 Kleinheins, J., Kiselev, A., Keinert, A., Kind, M. & Leisner, T. Thermal Imaging of Freezing Drizzle Droplets: Pressure Release Events as a Source of Secondary Ice Particles. *J. Atmos. Sci.* **78**, 1703-1713 (2021).

17 Korolev, A. *et al.* Observation of secondary ice production in clouds at low temperatures. *Atmos. Chem. Phys.* **22**, 13103-13113 (2022).

18 Malkin, T. L. *et al.* Stacking disorder in ice I. *Phys. Chem. Chem. Phys.* **17**, 60-76 (2015).

19 Maruyama, M. *et al.* X-Ray Analysis of the Structure of Premelted Layers at Ice Interfaces. *Jpn. J. Appl. Phys.* **39**, 6696-6699 (2000).

20 Dash, J. G., Rempel, A. W. & Wettlaufer, J. S. The physics of premelted ice and its geophysical consequences. *Rev. Mod. Phys.* **78**, 695-741 (2006).

21 Laksmono, H. *et al.* Anomalous Behavior of the Homogeneous Ice Nucleation Rate in "No-Man's Land". *J. Phys. Chem. Lett.* **6**, 2826-2832 (2015).

22 Buttersack, T., Weiss, V. C. & Bauerecker, S. Hypercooling Temperature of Water is about 100 K Higher than Calculated before. *J. Phys. Chem. Lett.* **9**, 471-475 (2018).

23 Keinert, A., Spannagel, D., Leisner, T. & Kiselev, A. Secondary Ice Production upon Freezing of Freely Falling Drizzle Droplets. *J. Atmos. Sci.* **77**, 2959-2967 (2020).

24 Thomson, E. S., Hansen-Goos, H., Wettlaufer, J. S. & Wilen, L. A. Grain boundary melting in ice. *J. Chem. Phys.* **138** (2013).

25 Niozu, A. *et al.* Crystallization kinetics of atomic crystals revealed by a single-shot and single-particle X-ray diffraction experiment. *Proc. Natl. Acad. Sci. USA* **118** (2021).

26 Williamson, G. K. & Hall, W. H. X-ray line broadening from filed aluminium and wolfram. *Acta Metall.* **1**, 22-31 (1953).

27 Hondoh, T. Dislocation mechanism for transformation between cubic ice I_c and hexagonal ice I_h. *Philos. Mag.* **95**, 3590-3620 (2015).

28 Haji-Akbari, A. & Debenedetti, P. G. Direct calculation of ice homogeneous nucleation rate for a molecular model of water. *Proc. Natl. Acad. Sci. USA* **112**, 10582-10588 (2015).

29 Lupi, L. *et al.* Role of stacking disorder in ice nucleation. *Nature* **551**, 218-222 (2017).

30 Murray, B. J. & Bertram, A. K. Formation and stability of cubic ice in water droplets. *Phys. Chem. Chem. Phys.* **8**, 186-192 (2006).

31 Liang, M. N. *et al.* The Coherent X-ray Imaging instrument at the Linac Coherent Light Source. *J. Synchrotron Radiat.* **22**, 514-519 (2015).

32 Emma, P. *et al.* First lasing and operation of an ångstrom-wavelength free-electron laser. *Nat. Photonics* **4**, 641-647 (2010).

33 Hart, P. *et al.* The CSPAD megapixel x-ray camera at LCLS. *Proc. SPIE* **8504**, 85040C (2012).

34 Stan, C. A. *et al.* Liquid explosions induced by X-ray laser pulses. *Nat. Phys.* **12**, 966-971 (2016).

35 Brownscombe, J. & Thorndike, N. Freezing and shattering of water droplets in free fall. *Nature* **220**, 687-689 (1968).

36 Stan, C. A. *et al.* Rocket drops: The self-propulsion of supercooled freezing drops. *Phys. Rev. Fluids* **8**, L021601 (2023).

37 Kalita, A. *et al.* *X-ray laser diffraction and optical image data from freezing supercooled water drops*. CXIDB ID 217 (CXIDB, 2023). https://dx.doi.org/10.11577/1973475

38 Stan, C. A., Marte, S., Kalita, A. & Mrozek-McCourt, M. *Separation of sharp and diffuse diffraction patterns from X-ray laser scattering of freezing water drops*. Version 1.0 (Zenodo, 2023). https://doi.org/10.5281/zenodo.7908740

39 Yefanov, O. *et al.* Accurate determination of segmented X-ray detector geometry. *Opt. Express* **23**, 28459-28470 (2015).

40 Treacy, M., Newsam, J. & Deem, M. A general recursion method for calculating diffracted intensities from crystals containing planar faults. *Proc. R. Soc. Lond. A* **433**, 499-520 (1991).

41 Hudait, A., Qiu, S. W., Lupi, L. & Molinero, V. Free energy contributions and structural characterization of stacking disordered ices. *Phys. Chem. Chem. Phys.* **18**, 9544-9553 (2016).

42 Amaya, A. J. *et al.* How Cubic Can Ice Be? *J. Phys. Chem. Lett.* **8**, 3216-3222 (2017).

43 Stan, C. A., Kalita, A. & Mrozek-McCourt, M. *Modeling of supercooling, solidification, and freezing stages of water drops*. Version 1.0 (Zenodo, 2023). https://doi.org/10.5281/zenodo.7908648

44 Smith, J. D., Cappa, C. D., Drisdell, W. S., Cohen, R. C. & Saykally, R. J. Raman Thermometry Measurements of Free Evaporation from Liquid Water Droplets. *J. Am. Chem. Soc.* **128**, 12892-12898 (2006).

45 Crank, J. & Nicolson, P. A practical method for numerical evaluation of solutions of partial differential equations of the heat-conduction type. *Proc. Camb. Philos. Soc.* **43**, 50-67 (1947).

46 Goy, C. *et al.* Shrinking of Rapidly Evaporating Water Microdroplets Reveals their Extreme Supercooling. *Phys. Rev. Lett.* **120**, 015501 (2018).

47 Ando, K., Arakawa, M. & Terasaki, A. Freezing of micrometer-sized liquid droplets of pure water evaporatively cooled in a vacuum. *Phys. Chem. Chem. Phys.* **20**, 28435-28444 (2018).

48 Rosenfeld, D. & Woodley, W. L. Deep convective clouds with sustained supercooled liquid water down to −37.5 °C. *Nature* **405**, 440-442 (2000).

49 Amaya, A. J. & Wyslouzil, B. E. Ice nucleation rates near ~225 K. *J. Chem. Phys.* **148**, 084501 (2018).

50 Zobrist, B., Koop, T., Luo, B., Marcolli, C. & Peter, T. Heterogeneous ice nucleation rate coefficient of water droplets coated by a nonadecanol monolayer. *J. Phys. Chem. C* **111**, 2149-2155 (2007).

51 Ickes, L., Welti, A., Hoose, C. & Lohmann, U. Classical nucleation theory of homogeneous freezing of water: thermodynamic and kinetic parameters. *Phys. Chem. Chem. Phys.* **17**, 5514-5537 (2015).

52 Koop, T. & Murray, B. J. A physically constrained classical description of the homogeneous nucleation of ice in water. *J. Chem. Phys.* **145**, 211915 (2016).

53 Pruppacher, H. R. Interpretation of Experimentally Determined Growth Rates of Ice Crystals in Supercooled Water. *J. Chem. Phys.* **47**, 1807-1813 (1967).

54 Hooke, R. & Jeeves, T. A. "Direct Search" Solution of Numerical and Statistical Problems. *J. ACM* **8**, 212 (1961).

55 Stan, C. A. *et al.* Negative Pressures and Spallation in Water Drops Subjected to Nanosecond Shock Waves. *J. Phys. Chem. Lett.* **7**, 2055-2062 (2016).

56 Albert, D. J. *Numerically solving a transient heat conduction problem with convection and radiation.* M.Sc. thesis, Naval Postgraduate School, Monterey, California, (1993).

57 Sone, Y. & Sugimoto, H. Kinetic theory analysis of steady evaporating flows from a spherical condensed phase into a vacuum. *Phys. Fluids A* **5**, 1491-1511 (1993).

58 Fukusako, S. Thermophysical Properties of Ice, Snow, and Sea Ice. *Int. J. Thermophys.* **11**, 353-372 (1990).

59 Yen, Y.-C. Review of thermal properties of snow, ice, and sea ice. Report No. CRREL 81-10, (U.S. Army, Corps of Engineers, Cold Regions Research and Engineering Laboratory, 1981).

60 Murphy, D. M. & Koop, T. Review of the vapour pressures of ice and supercooled water for atmospheric applications. *Q. J. R. Meteorol. Soc.* **131**, 1539-1565 (2005).

61 Bertolini, D. & Tani, A. Thermal conductivity of water: Molecular dynamics and generalized hydrodynamics results. *Phys. Rev. E* **56**, 4135-4151 (1997).

62 Saito, A., Okawa, S. & Shimamoto, D. Research on a thermal conductivity measurement of supercooled water. *Trans. Jpn. Soc. Mech. Eng.* **62**, 770 (1996).

63 Archer, D. G. & Carter, R. W. Thermodynamic properties of the NaCl+H_2O system. 4. Heat capacities of H_2O and NaCl(aq) in cold-stable and supercooled states. *J. Phys. Chem. B* **104**, 8563-8584 (2000).

64 Tombari, E., Ferrari, C. & Salvetti, G. Heat capacity anomaly in a large sample of supercooled water. *Chem. Phys. Lett.* **300**, 749-751 (1999).

65 Riechers, B., Wittbracht, F., Hutten, A. & Koop, T. The homogeneous ice nucleation rate of water droplets produced in a microfluidic device and the role of temperature uncertainty. *Phys. Chem. Chem. Phys.* **15**, 5873-5887 (2013).

66 Langmuir, I. The evaporation of small spheres. *Phys. Rev.* **12**, 368-370 (1918).

67 Stephan, K. & Laesecke, A. The Thermal Conductivity of Fluid Air. *J. Phys. Chem. Ref. Data* **14**, 227-234 (1985).

68 Marrero, T. R. & Mason, E. A. Gaseous Diffusion Coefficients. *J. Phys. Chem. Ref. Data* **1**, 3-118 (1972).

69 *NIST Chemistry WebBook*. (NIST Standard Reference Database Number 69, 2022). https://doi.org/10.18434/T4D303

70 Langmuir, I. Convection and conduction of heat in gases. *Phys. Rev.* **34**, 401 (1912).

71 Brody, I. & Kőrösy, F. Convection and conduction of heat in gases. *J. Appl. Phys.* **10**, 584-596 (1939).

72 Beard, K. V. & Pruppacher, H. R. A determination of the terminal velocity and drag of small water drops by means of a wind tunnel. *J. Atmos. Sci.* **26**, 1066-1072 (1969).

73 *U.S. Standard Atmosphere, 1976*. Report NOAA-S/T-76-1562 (National Oceanic and Atmospheric Administration, 1976).

74 Kobel, P., Obreschkow, D., de Bosset, A., Dorsaz, N. & Farhat, M. Techniques for generating centimetric drops in microgravity and application to cavitation studies. *Exp. Fluids* **47**, 39-48 (2009).

75 Röttger, K., Endriss, A., Ihringer, J., Doyle, S. & Kuhs, W. F. Lattice constants and thermal expansion of H_2O and D_2O Ice I*h* between 10 and 265 K. Addendum. *Acta Cryst. B* **68**, 91-91 (2012).

76 Dowell, L. G. & Rinfret, A. P. Low-Temperature Forms of Ice as Studied by X-Ray Diffraction. *Nature* **188**, 1144-1148 (1960).

77 van Driel, T. B., Herrmann, S., Carini, G., Nielsen, M. M. & Lemke, H. T. Correction of complex nonlinear signal response from a pixel array detector. *J. Synchrotron Radiat.* **22**, 584-591 (2015).

78 Herrmann, S. *et al.* CSPAD upgrades at LCLS. Report No. SLAC-PUB-15843, (SLAC National Accelerator Laboratory, 2014).